11

Microporous Materials Characterized by Vibrational Spectroscopies

Can Li and Zili Wu
Chinese Academy of Sciences, Dalian, China

I. INTRODUCTION

The characterization of microporous materials, more popularly called zeolitic materials, began with the discovery and synthesis of zeolites in the 1960s. Various spectroscopic techniques, i.e., X-ray diffraction (XRD), IR, Raman, nuclear magnetic resonance (NMR), electron spin resonance (ESR), and so forth have been used to characterize zeolites and/or zeolite-adsorbate systems. Among these techniques, vibrational spectroscopies, mainly IR spectroscopy and Raman spectroscopy, are most extensively employed for the investigation of zeolites and the interaction between zeolites and adsorbates.

The properties of zeolites are mainly dependent on their structure, so that it is absolutely necessary to characterize the structure of zeolites, as well as the changes in the structure during the synthesis and use of zeolites. In principle, vibrational spectroscopies such as IR and Raman are the most powerful techniques to supply detailed information on the structure of molecules. Thus, vibrational spectroscopies have been most frequently used to characterize the microporous materials (mainly zeolites) since the beginning of zeolite discovery and synthesis. Another advantage is that several vibrational spectroscopies can be applied under in situ conditions and they can be very successfully used for studies of high-surface-area porous materials like zeolites. To date, IR and Raman spectroscopies have been successfully applied to the zeolite characterization in almost every aspect, such as (a) framework and extraframework structure, e.g., lattice vibrations related to structure type, cation vibrations related to cation nature and location; (b) sites in zeolites, usually characterized by using probe molecules; (c) adsorption and catalytic reactions on zeolites; and (d) the guest–host chemistry within zeolite channel and cavity.

Many extensive reviews have been written on zeolite characterization by vibrational spectroscopies, but most are very specific and focused on research review; few papers are general and comprehensive. This chapter is intended to give a general introduction and to include the newly published literature (mainly in the last two decades) on the vibrational spectroscopic characterization of microporous materials, starting with the theoretical description of IR and Raman spectroscopy, followed by the application of IR and Raman spectroscopy to zeolites and zeolite-adsorbate systems, and finally the recent advances of UV-Raman spectroscopy in zeolite studies. Obviously, it is impossible to cover in depth

the spectroscopic characterization of all microporous materials reported in the literature in a single chapter, but we try to be as exhaustive as possible and most published work will be listed in tabular form.

II. PRINCIPLE: VIBRATIONAL SPECTROSCOPIES

A. IR Spectroscopy

1. Theory of IR Spectroscopy

Infrared spectroscopy is the most common form of vibrational spectroscopy. It has been for more than 30 years the most important and commonly used technique to characterize zeolites and zeolite-adsorbate systems (1–6). IR radiation falls into three categories, as illustrated in Table 1. Molecules possess discrete levels of rotational and vibrational energy. Transitions between vibrational levels usually occur by absorption of photons with frequencies v in the mid-IR range (Table 1). For small deviations of the constituent atoms from their equilibrium positions, the potential energy $V(r)$ can be approximately expressed as that of a harmonic oscillator:

$$V(r) = k(r - r_{eq})^2 \tag{1}$$

in which $V(r)$ is the interatomic potential; r and r_{eq} the distance between the vibrating atoms and the equilibrium distance between the atoms, respectively; and k the force constant of the vibrating bond. Figure 1 shows the plot of $V(r)$ as a function of r (dotted line). This is a parabolic potential and such a vibrator is called a harmonic oscillator. The corresponding vibrational energy levels are equidistant and can be described as (7,8):

$$E_v = hv(v + 1/2)/2 \tag{2}$$

where h is Planck's contant, v is the vibrational quantum number, and it can have the values 0, 1, 2, 3, . . . , and v is the frequency of the vibration:

$$v = \frac{1}{2\pi}\sqrt{k(m_1 + m_2)/m_1 m_2} = \frac{1}{2\pi}\sqrt{k/\mu} \tag{3}$$

with μ as the reduced mass and m_i the mass of the vibrating atoms. The simple relationship between frequency, force constant, and mass (or reduced mass) given in Eq. (3) is often used in conjunction with isotopic substitution to assign or interpret observed frequencies.

The harmonic approximation is only valid for small deviations of the atoms from their equilibrium positions, and the separation between the two successive vibrational levels is aways the same (hv). Allowed transitions are those for which the vibrational

Table 1 Classification of Infrared Radiation

Region	Wavelength (μm)	Energy (meV)[a]	Wavenumber (cm^{-1})	Detection of
Infrared	1000–1	1.2–1240	10–10,000	—
Far	1000–50	1.2–25	10–200	Lattice vibrations
Mid	50–2.5	25–496	200–4000	Molecular vibrations
Near	2.5–1	496–1240	4000–10,000	Overtones

[a] 1 meV = 8.0655 cm^{-1}.

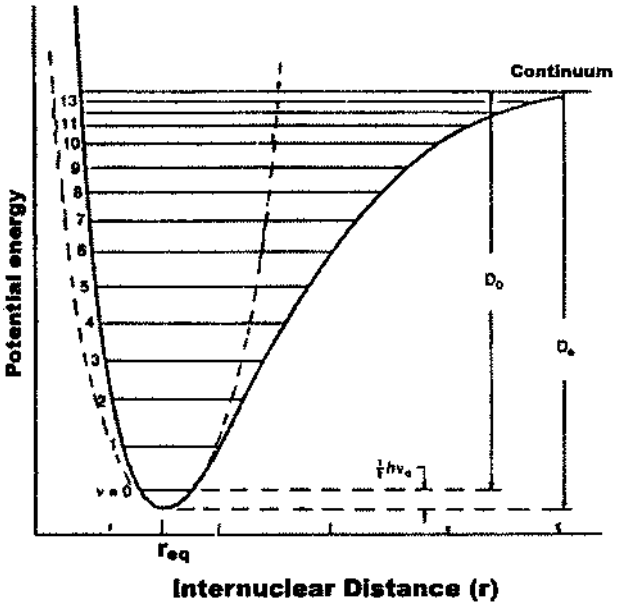

Fig. 1 Potential energy curve for a diatomic molecule. Solid line indicates a Morse potential that approximates the actual potential. Broken line is a parabolic potential for a harmonic oscillator. D_e and D_0 are the theoretical and spectroscopic dissociation energies, respectively.

quantum number changes by one unit, namely, $\Delta v = \pm 1$. Overtones, i.e., absorption of light at a whole number times the fundamental frequency, would not be allowed. This is not the case of an actual molecule whose potential is approximated by the Morse potential function shown in Fig. 1 (solid line).

$$V = D_e(1 - e^{-\beta x})^2 \tag{4}$$

where D_e is the dissociation energy and β is a measure of the curvature at the bottom of the potential well. If the Schrödinger equation is solved with this potential, then

$$Ev = h\nu(v + 1/2) - h\chi_e\nu(v + 1/2)^2 + \cdots \tag{5}$$

where χ_e is the anharmonicity constant.

Equation (5) shows that the energy levels of the anharmonic oscillator are no longer equidistant, and the separation decreases with the increase of v as shown in Fig. 1. And overtones, i.e., vibrational transitions with $\Delta v > 1$, become allowed.

For polyatomic molecules with N atoms, the number of fundamental vibrations is $3N-6$ for a nonlinear and $3N-5$ for a linear molecule. In addition, there are overtones and combinations of fundamental vibrations. Fortunately, however, not all vibrations can be observed. Absorption of an IR photon occurs only if a dipole moment changes during the vibration. It is not necessary that the molecule possess a permanent dipole; it is sufficient if a dipole moment changes during the vibration. The intensity of the IR band is proportional to the change in dipole moment. This distinguishes IR from Raman spectroscopy where the selection rule requires that the molecular polarizability change during the vibration.

In diatomic molecules, the vibration occurs only along the chemical bond connecting the two atoms. In polyatomic molecules like zeolite, the situation is complicated because all of the nuclei perform their own harmonic oscillations. This problem can sometimes be resolved by a technique known as a *normal coordinate analysis*. In this method, a functional group in a polyatomic molecule may be treated as independent oscillators, irrespective of the larger structure to which they belong. In other words, any of the complicated vibrations of a molecule can be expressed as a superposition of a number of "normal vibrations" that are completely independent of each other. For example, the vibrations of the TO_4 tetrahedra (with, e.g., T = Si or Al) in the framework of zeolite consist of many modes, i.e., the asymmetrical stretching mode ($\leftarrow$ OT $\rightarrow$ $\leftarrow$ O), symmetrical stretching mode ($\leftarrow$ OTO $\rightarrow$), and T-O bending mode of the TO_4 tetrahedra.

However, for the application of IR spectroscopy in zeolite research, the spectra are usually not interpreted by comparison with theoretically derived frequencies but mainly on the basis of empirical data, e.g., via comparison with known spectra of solids, liquids, or gases. Only in a few cases are frequencies computed and related to experimentally obtained data.

2. Experimental Techniques

a. Transmission IR Spectroscopy

Transmission IR spectroscopy has been the most widely used technique to study the structure of zeolites and the adsorbed species. In this case, the sample consists typically of 10–100 mg of zeolite, pressed into a self-supporting or KBr-mixed disk of approximately 1 cm^2 and a few tenths of a millimeter thickness. The disk is then placed perpendicular to a beam of IR radiation, and the spectrum is recorded by detecting the transmitted beam. Figure 2 illustrates the positions of the incident and transmitted beams in a typical transmission experiment. I_0 represents the incident energy of radiation, I the transmitted energy, and T the transmittance, $T = I/I_0$. The absorbance is defined as:

$$A = -\ln T = \ln I_0/I \tag{6}$$

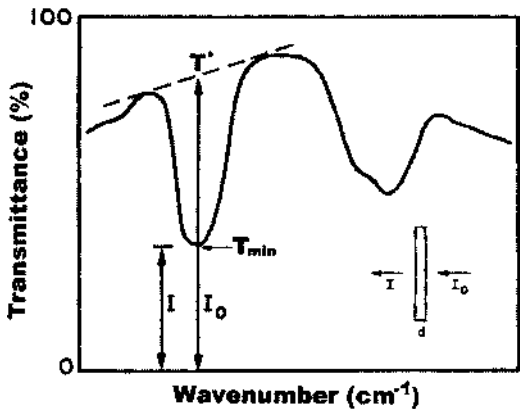

Fig. 2 Schematic illustration of a transmission experiment and the illustration of the method used to determine the incident and transmitted radiation from a transmission spectrum.

For quantitative evaluation of the concentration, c, of the species involved, one may use the Lambert-Beer law:

$$A = \varepsilon_v cd \tag{7}$$

where ε is the extinction coefficient and d the thickness of the sample. For materials in which an absorbing functional group may be present in a variety of bonding environments, it is often preferable to work in terms of the integrated absorbance (A_{int}) rather than the absorbance at the band maximum. The integrated absorbance as a quantitative measure of the IR-absorbing species can be expressed as:

$$A_{\text{int}} = cd \int_{v_1}^{v^2} \varepsilon_v \, dv = cd \int_{v_1}^{v^2} \ln(I_0(v)/I(v))dv \tag{8}$$

Equation (8) is strictly valid only for infinitely diluted systems where ε_v can be taken as a constant. For vibrations of a solid lattice or functional groups present at the surface (e.g., OH, SH, etc.), ε_v is a constant. For spectrum of species adsorbed on a catalyst, ε_v may be changed with changing the adsorbate concentration. For IR measurement of zeolites, ε_v is usually unknown. Experimental determination of ε_v is troublesome and practiced only in a few cases (8). Therefore, very often the absorbances are given in arbitrary units, and only relative concentrations or numbers of species are estimated. Mostly the band intensities are not integrated, and the maximal absorbance, $A_{\max} = \ln(T^*/T_{\min})$, is used as a measure of the relative concentration.

Scattering of the incident radiation can be significant for samples prepared from powders. The effect of scattering is to reduce the intensity of the transmitted beam, thereby making it harder to obtain a good spectrum. According to the theory of Rayleigh scattering, scattering is most severe for large particles and high wavenumbers. To avoid such artifacts, it is desirable to work with particles less than 1 μm in diameter, whenever possible (9).

b. Diffuse Reflectance IR (Fourier Transform) Spectroscopy (DRIFT)

For a long time, IR spectroscopic studies on zeolites were almost exclusively carried out in the transmission mode. More recently, Kazansky and coworkers (10,11) pioneered the work in employing diffuse reflectance spectroscopy (DRS), which used to be an important method for UV-visible spectroscopy of solid samples like zeolites. DRS is very helpful in exploring the near-IR region, where transmission techniques essentially fail due to the severe scattering of the zeolite samples. However, this region is of great interest because the overtone and combination modes of the hydroxyls appear in this region. Moreover, it brings larger differences in the frequencies in overtone of different types of OH groups than in the mid-IR region. Also, the interference of water on the observation of the vibrations of OH groups in the mid-IR region could be avoided by this technique.

To take the diffuse reflectance spectrum of a powder sample, the sample is placed in a shallow cup and exposed to a beam of IR radiation, as shown in Fig. 3. The incident radiation passes into the bulk of the sample and undergoes reflection, refraction, and absorption before reemerging at the sample surface. The diffusely reflected radiation from the sample is collected by a spherical or elliptical mirror and focused onto the detector of the IR spectrometer. Two important requirements for successful diffuse reflectance measurements must be fulfilled: (a) the sample must be sufficiently thick and large to avoid light loss by forward scattering and/or scattering at its edges; (b) scattering must be predominant compared with absorption so that illumination is essentially diffuse.

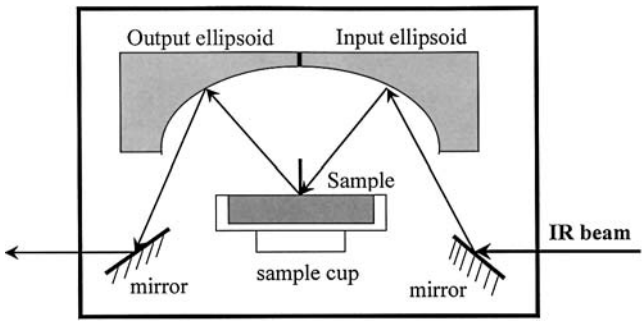

Fig. 3 Scheme of a unit for diffuse reflectance infrared spectroscopy.

The interpretation of diffuse reflectance spectra is based on the phenomenologic theory developed by Kubelka and Munk (12,13) and has been well summarized in some books (6,9,14). The IR absorption spectrum is described by the Kubelka-Munk function:

$$K/S = (1 - R_\infty)^2/2R_\infty \tag{9}$$

where K is the absorption coefficient, a function of the frequency v

S is the scattering coefficient

R_∞ is the reflectance of a very thick sample with zero backgroud reflectance, measured as a function of v.

If S does not depend on the IR frequency, the Kubelka-Munk function transforms the measured spectrum $R_\infty(v)$ into the absorption spectrum $K(v)$. Unfortunately, up to now, no quantitative measurements of the diffuse reflectance are reported, mainly due to the lack of general standards as exists in UV-visible region. In situ cells for DRIFT studies and reflectance accessories have been described (6,9,14) and are commercially available.

Other IR techniques, such as photoacoustic IR spectroscopy (PAS) (6,15,16), IR emission spectroscopy (17), attenuated total reflection (ATR) FTIR spectroscopy (18), have also been occasionally used to characterize zeolite systems.

B. Raman Spectroscopy

1. Introduction

Raman spectroscopy is concerned with vibrational and rotational transitions, and in this respect it is similar to IR spectroscopy. However, in comparison with the vast amount of IR spectroscopy work, the field of zeolite Raman spectroscopy has not attracted the same attention and is still evolving (19). The reason for this is that there is considerable difficulty in obtaining Raman spectra with acceptable signal-to-noise ratios from highly dispersed materials such as zeolites. Two main problems are responsible for this: the intrinsically low sensitivity of Raman spectroscopy because the Raman scattering is very weak, and the strong fluorescence interference often obscuring the Raman spectrum of zeolite for Raman spectroscopy which uses visible laser as the excitation sources. In order to increase the sensitivity and to avoid the fluorescence background, shifting the excitation frequency can often obtain successful Raman spectra of zeolite samples (20–26). Variation of the excitation frequency led to two recent instrumental advances: Fourier transform Raman (FT-Raman) spectroscopy and UV Raman spectroscopy. The advent of FT-Raman spectroscopy with excitation source in the near-infrared (NIR) region, and especially the

employment of UV Raman spectroscopy with excitation in the UV region, offers new perspectives in enhancing the sensitivity and avoiding fluorescence background.

2. Theory of Raman Spectroscopy

There exist extensive, detailed descriptions of Raman theory (10,11,27–30). When a molecule is irradiated by a light with frequency v, a small portion of it is scattered inelastically but most part is scattered elastically. The elastically scattered light with the same frequency υ of the incident light is called Rayleigh scattering, and the inelastically scattered light with frequencies $v \pm v_1$ is called Raman scattering. Light scattering arises from dipole moments induced in atoms or molecules by the incident field, through the polarizability of the electrons. The static polarizability leads to Rayleigh scattering, whereas modulation of the polarizability by electronic, vibrational, or rotational motion leads to Raman scattering. Thus, the vibrational frequencies are observed as Raman shifts from the incident frequency v.

The origin of Raman spectra can be explained by classical theory. Consider a light wave of frequency v with an electric field strength E. E can be expressed as

$$E = E_0 \cos 2\pi v\mathrm{t} \tag{10}$$

where E_0 is the amplitude of the incident light at $t = 0$ and t the time. When a diatomic molecule is irradiated by this light, the dipole moment P is given by

$$P = \alpha E = \alpha E_0 \cos 2\pi v\mathrm{t} \tag{11}$$

Here α is called the polarizability. If the molecule is vibrating with frequency v_1, the nuclear displacement q is written as

$$q = q_0 \cos 2\pi v_1 t \tag{12}$$

where q_0 is the vibrational amplitude. If the polarizability changes during the vibration, its value for a small vibrational amplitude will be given by

$$\alpha = \alpha_0 + \left(\frac{\partial \alpha}{\partial q}\right) q \tag{13}$$

where α_0 is the polarizability at the equilibrium position, and $(\partial\alpha/\partial q)_0$ is the rate of change of α with respect to the change in q, evaluated at the equilibrium position. Combining Eqs. (11)–(13), we have

$$\begin{aligned} P &= \alpha E_0 \cos 2\pi v t \\ &= \alpha E_0 \cos 2\pi v t + \left(\frac{\partial \alpha}{\partial q}\right)_0 q_0 E_0 \cos 2\pi v t \cos 2\pi v_1 t \\ &= \alpha E_0 \cos 2\pi v t + \left(\frac{\partial \alpha}{\partial q}\right)_0 q_0 E_0 [\cos \{2\pi(v + v_1)t\} + \cos \{2\pi(v - v_1)t\}]/2 \end{aligned} \tag{14}$$

The first term in Eq. (14) describes the Rayleigh scattering of frequency v, and the remaining term gives the Raman scattering of frequencies $v + v_1$ (anti-Stokes) and $v - v_1$ (Stokes). In addition, Eq. 14 tells that Raman scattering requires

$$\left(\frac{\partial \alpha}{\partial q}\right) \neq 0 \tag{15}$$

That is, the polarizability of the molecule must change during the vibration for a Raman active mode.

In the quantum theory of Raman scattering, the vibrational energy of a molecule is recognized to be quantized. A nonlinear molecule with N atoms has $3N - 6$ normal vibrations and a linear molecule has $3N - 5$. The energy of each of these vibrations will be quantized according to the relationship in Eq. 2. Perturbation theory is used to introduce quantization into the Raman scattering theory. Put simply, this approach applies perturbations to the ground-state molecular wavefunctions until new wavefunctions are obtained that describe the vibrational excited state. The transition from ground state can then be regarded as being achived via a perturbing wavefunction, which is the sum of the perturbations applied. This perturbing wavefunction will have a corresponding energy and gives us a useful pictorial description of Raman scattering with the vibrational transitions occurring via this virtual energy level (Fig. 4).

The Rayleigh scattering arises from transitions that start and finish at the same vibrational energy level. In the case of Stokes lines, the molecule at $v = 0$ is excited to the $v = 1$ state by scattering light of frequency $v - v_1$. Anti-Stokes lines arises when the molecule initially in the $v = 1$ state scatters radiation of frequency $v + v_1$ and reverts to the $v = 0$ state. Since the population of molecules is larger at $v = 0$ than $v = 1$ (the Maxwell-Boltzmann distribution law), the Stokes lines are always stronger than the anti- Stokes lines. For this reason, the Stokes Raman scattering is usually used in Raman spectroscopy.

Theoretically, the intensities of Raman bands can be calculated as (30):

$$I_{mn} = CI_0(v_0 - v_1)^4 \sum_{ij} \left|(\alpha_{ij})_{mn}\right|^2 \tag{16}$$

Where C is a constant, I_0 the incident intensity, and α_{ij} the components of the polarizability tensor associated with the transition from m to n states.

$$(\alpha_{ij})_{mn} = \frac{1}{h}\sum_e \left(\frac{M^i_{me} M_{en}}{v_{em} - v_0 + i\Gamma_e} + \frac{M_{me} M^i_{en}}{v_{en} + v_0 + i\Gamma_e} \right. \tag{16–17}$$

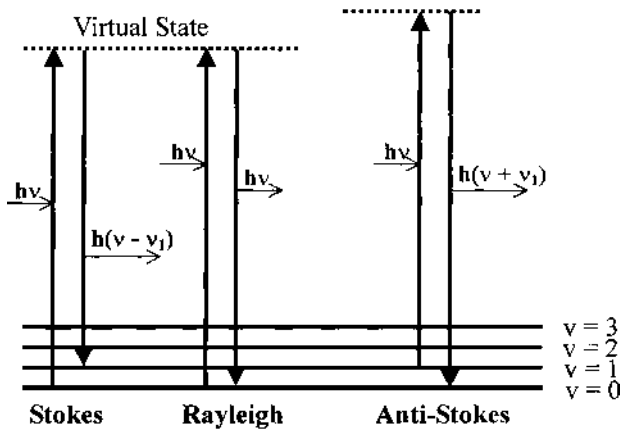

Fig. 4 Schematic mechanism for Rayleigh scattering and Raman scattering.

where v_{em} and v_{en} are the frequencies corresponding to the energy differences between the states subscribed and h is Planck's constant. M_{me}^{I}, etc., are the electric transition moments. Γ_e is the bandwidth of the eth state.

3. Experimental Techniques

a. Conventional Raman Spectroscopy

A Raman spectrometer has five major components (11):

1. *Excitation source*. This is generally a continous wave (CW) gas laser such as Ar^+ (351.1–514.5 nm), Kr^+ (337.4–676.4 nm), or He-Ne (632.8 nm).
2. *Sample illumination and scattered light collection system*. In principle, Raman scattered light can be viewed at any angle with respect to the direction of propagation of the exciting beam. The three most often used experimental arrangements use an angle of 0° (forward scattering), 90°, and 180° (back scattering) between the excitation incidence and the collection of Ramans scattering.
3. *Sample holder*. In most cases, the sample holder can be rotated or vibrated when measuring the sample in order to avoid overheating by laser. For in situ Raman studies, various Raman cells were designed (7,28,32). Most cells used in studies to date have been made of glass or quartz, with optical flats cemented in place. Standard glass vacuum line technology has been employed, and caution against the use of vacuum grease (which is highly fluorescent) in connectors or stopcocks is recommended (32).
4. *Monochromator or spectrograph*. This disperses the light scattered from the sample and then Raman spectrum can be acquired by the detector. It is also used to reject Rayleigh lines and reduce the stray light so that weak Raman scattering can be observed.
5. *Detection system*. Several sensitive detection techniques are now commonly used: photon counting using photomultiplier (PM) tube, photodiode array detection, charge-coupled device (CCD) detection.

b. FT-Raman Spectroscopy

With the idea that fluorescence may be reduced by shifting the exciting wavelength to longer wavelength, a new Raman technique, FT-Raman spectroscopy, was suggested in the 1960s (33) and became viable in the 1980s. Employing an exciting line in the near-IR region (1064 nm of Nd:YAG laser) where electronic transitions are rare, FT-Raman is very effective in reducing or eliminating fluorescence interference for many samples including biomolecules. FT-Raman spectroscopy can also achieve high resolution, which is difficult for conventional Raman spectroscopy.

Conventional Raman spectroscopy measures intensity vs. frequency or wavenumber. FT instruments, on the other hand, measure the intensity of light of many wavelengths simultaneously. The latter is often referred to as a time-domain spectroscopy. This spectrum is then converted to a conventional spectrum by means of Fourier transformation using computer programs. The distinctive feature of the FT technique, like FTIR, is that it sees all wavelengths at all times. This provides improved resolution, spectral acquisition time, and signal-to-noise ratio (S/N) over conventional dispersive Raman spectroscopy.

Although the interest in FT-Raman has increased significantly, several limits of its capability remain (34): (a) FT-Raman cannot completely eliminate the fluorescence background when samples absorb light strongly in the NIR region. For many zeolite samples,

fluorescence background in the NIR region is still too strong to obtain good FT-Raman spectra. (b) The sensitivity of FT-Raman spectroscopy is still low since the Raman scattering cross-section decreases as λ increases ($I \propto 1/\lambda)^4$ although FT technique can improve the sensitivity somewhat. (c) A serious problem of FT-Raman is the difficulty to study samples at elevated temperatures. For most cases, temperature cannot be greater than 373 K because the thermal black-body emission from the sample becomes more intense (broad background) than the Raman signal. As a result, FT-Raman measurements of catalytic samples under reaction conditions are nearly impossible.

c. Resonance Raman Spectroscopy

Resonance Raman (RR) scattering occurs when the sample is irradiated with an exciting line whose energy corresponds to that of the electronic transition of a particular chromophoric group in a molecule. Under these conditions, the intensities of Raman bands originating in this chromophore (mostly v_1 mode) are selectively enhanced by a factor of 10^3–10^5. This selectivity is important not only for identifying vibrations of this particular chromophore in a complex molecule but also for locating its electronic transitions in an absorption spectrum.

The enhancement of the Raman bands in resonance Raman scattering can be explained theoretically by Eq. (17). In normal Raman scattering, the excitation frequency v_0 is always from an electronic transition, i.e., $v_0 < v_{em}$. Namely, the energy of the incident light is smaller than that of an electronic transition. When is v_0 approaches an electronic transition, v_{em}, the denominator of the first term in the brackets of Eq. (17) becomes infinite. Hence, this term ("resonance term") becomes so large that the value of the polarizability tensor components increases dramastically. This results in increases in the intensity of the Raman band of several orders of magnitude. This phenomenon is called *resonance Raman scattering*. Two broad types of resonance effect can be identified: the preresonance Raman effect and the resonance Raman effect. Figure 5 shows the energy level diagram for these two Raman effects.

Figure 6 shows how to use resonance Raman spectroscopy to selectively study the local structure of a compound. Suppose that a compound contains two chromophoric groups that exhibit electronic absorption bands at v_A and v_B as shown in Fig. 6. Then, vibrations of chromophore A are resonance enhanced when v_0 is chosen near v_A, and those of chromophore B are resonance-enhanced when v_0 is chosen near v_B. Thus, the vibrations of the two different chromophores can be selectively enhanced by choosing exciting lines in the regions of their electronic absorption.

d. UV Raman Spectroscopy

As the fluorescence usually occurs in the visible or near-UV region, UV Raman utilizes an excitation laser line (using a frequency-doubled Ar^+ ion laser) in the UV region, which shifts the excitation wavelength to the opposite direction of FT-Raman. It has been demonstrated that there are several advantages of UV Raman spectroscopy over conventional Raman spectroscopy: (a) The fluorescence is avoided successfully in the UV region because most fluorescence appears in the visible region. This is particularly important to zeolite characterization. (b) The sensitivity will be increased significantly since the Raman scattering intensity is inversely proportional to the fourth power of wavenumber (λ^4). (c) *Resonance Raman enhancement*. As most electronic transitions occur in the UV region, there are more opportunities to make use of the resonance Raman effect in the UV Raman

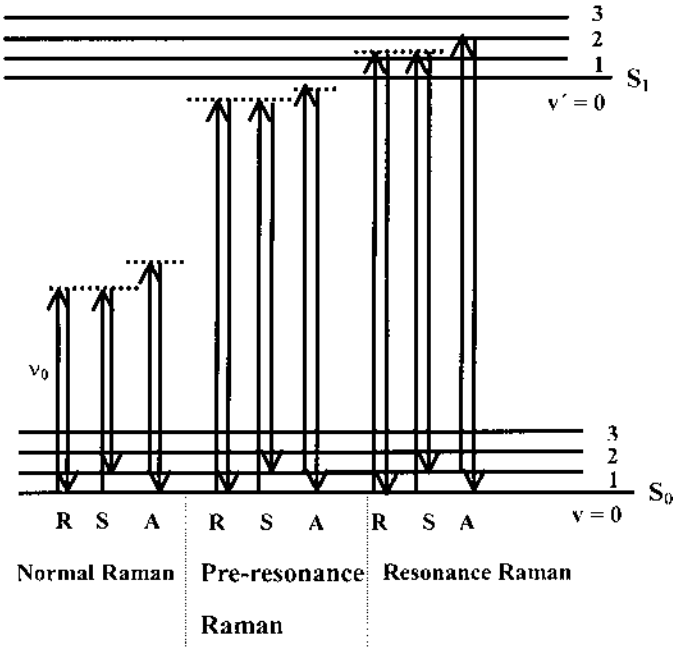

Fig. 5 Comparison of energy levels for the normal Raman, preresonance Raman, and resonance Raman.

spectroscopy. (d) High excitation frequency leads to an important advantage when conducting high temperature in situ Rman experiments: the higher the excitation frequency, the lower the black-body radiation background.

UV Raman spectrosocopy was first introduced to catalysis research by Li and Stair (35–39) to measure Raman spectra from a variety of materials that would otherwise be very difficult to measure by conventional Raman spectroscopy. Later on, UV Raman was

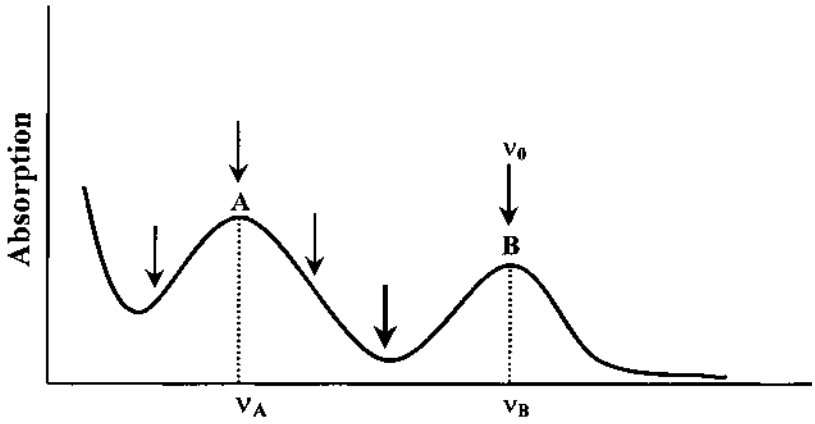

Fig. 6 Absorption spectrum of a compound containing two chromophoric groups (A and B).

demonstrated to be a powerful tool for the characterization of zeolite systems that are particularly suffering from fluorescence interference in the visible Raman spectroscopy (23–26,40–43). For example, the enhancement of Raman intensities by resonant scattering is very useful for detecting some species present at low concentrations in catalytic materials. Since the charge transfer between the framework metal atoms and the framework oxygen atoms occurs in the UV region, UVRRS is specially useful for identifying the transition metal species in the framework of zeolites, which is hard or impossible to be characterized by many other techniques.

A problem with recording Raman spectra of samples is that laser heating may lead to the loss of hydration water, phase transitions, partial reduction, or even decomposition due to photochemical or thermal effect. This problem may become more obvious in UV Raman measurements for some samples as the UV laser gives higher energy. Recently, a fluidized-bed catalytic reactor for in situ Raman spectroscopy measurements was devised to avoid this problem (41). A diagram of the apparatus is shown in Fig. 7. For a detailed description of this reactor, see Ref. 41.

It should be pointed out that solid-state NMR spectroscopy is as powerful a method (44,45) as vibrational (IR and Raman) spectroscopies, particularly after the recent development of 2D multiple-quantum MAS NMR techniques (46). Generally speaking, these two techniques are more complementary than competitive in the characterization of zeolites.

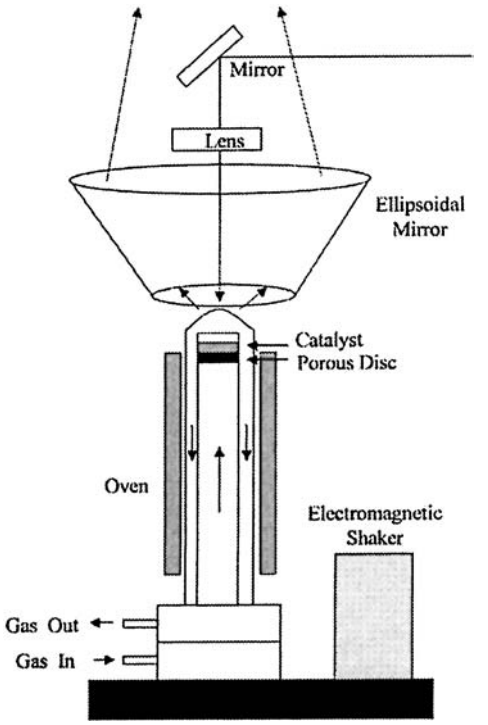

Fig. 7 Schematic diagram of the in situ fluidized bed reactor for UV Raman studies. (From Ref. 41.)

III. INFRARED SPECTROSCOPIC CHARACTERIZATION OF MICROPOROUS MATERIALS

The vibrational spectrum of a zeolite originates from several contributions, namely, the vibrations from the framework of the zeolite, from the charge-balancing cations, and from the relatively isolated groups, such as the surface OH groups.

A. Framework Vibrations

The zeolite framework is composed of the network formed by TO_4 (T = Si or Al) with tetrahedra corners. Vibrations of the frameworks of zeolites give rise to typical bands in the mid-IR and far-IR regions. A distinction is made between external and internal vibrations of the TO_4 tetrahedra. The terms *internal* and *external* have been used in the IR spectroscopy of zeolites to describe the vibrations in the tetrahedral building units and between them (i.e., double rings as in A-, X-, Y-type and pore openings as in mordenite), respectively. The vibrational frequencies of the so-called lattice modes of aluminosilicate zeolites (stretching and bending modes of the T-O linkages, plus specific vibrations of discrete structural units) were first studied in detail by Flanigen et al. (47) 60 years ago. Spectral frequencies of a series of synthetic zeolites are available (47,48).

An overall classification of the lattice vibration of zeolites can be drawn as Fig. 8 (48). The most predominant bands occur in the ranges from 1250 to 950, from 790 to 650, and from 500 to 420 cm^{-1}, assigned tentatively to the asymmetrical stretching mode (← OTO →), the symmetrical stretching mode (← OTO →), and the T-O bending mode of the TO_4 tetrahedra, respectively. Similarly, bands around 650–500 cm^{-1} and 420–300 cm^{-1} are due to external linkage vibrations, namely, vibrations of double four-membered rings (D4R), double five-membered rings (D5R), or double six-membered rings (D6R), and pore opening vibrations, respectively. For example, structural information can be easily identified by IR spectroscopy for zeolites containing five-membered rings (49). The absorption bands near 550 cm^{-1} have been assigned to the presence of five-membered rings in the structure (50,51). There are three types of five-membered ring blocks: a 5-5 block (A), a 5-3 block (B), and a 5-3-1 block (C).

The MFI and MEL topologies both contain A and B blocks, while the mordenite group [mordenite (MOR), ferrierite (FER), epistilbite (EPI), and dachiardite (DAC)] contains only B blocks. Bikitaite (BIK) contains only C-type five-ring blocks. The IR

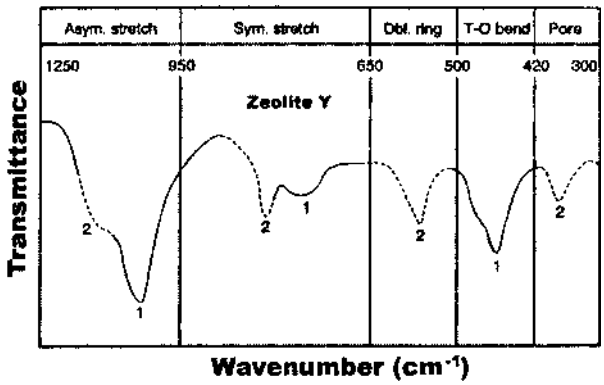

Fig. 8 Lattice vibrations of zeolite Y. (From Ref. 48.)

spectra of five-membered ring zeolites and molecular sieves have been reported and are listed in Table 2 (48–52). The structure-sensitive vibrations near 1200 and 550 cm^{-1} provide information on the differentiation of the zeolite types and are also useful for identifying some framework features of zeolites of undetermined crystal structures. As an example, the vibrational band at 550 cm^{-1} for siliceous MEL-type (silicalite-2) zeolite splits when the nano-sized silicalite-2 crystals are synthesized with average particle size less than 100 nm (53).

Table 2 IR Data Between 1500 and 400 cm^{-1} of Aluminosilicates Containing Five-Membered Rings

	Asymmetrical stretch[a]		Symmetrical stretch[a]	
Zeolite types	External	Internal	External	Internal
Silicate	1225(sh)	1093(s)	790(w)	—
ZSM-5	1225(sh)	1093(s)	790(w)	—
Boralite	1228(sh)	1096(s)	800(w)	—
ZSM-11	1225(sh)	1093(s)	790(w)	—
Mordernite	1223(sh)	1045(s)	800(w)	720(w)
Ferrierite	1218(sh)	1060(s)	780(w)	695(w)
Epistilbite	1175(sh)	1050(s)	795(w)	690(w)
Dachiardite	1210(sh)	1050(s)	775(w)	670(w)
Bikitaite	1105(sh)	968(s)	782(w)	680(w)
ZSM-39	—	1090(s)	790(w)	—
Melanophlogite	—	1118(s)	795(w)	—
ZSM-34	—	1060(s)	785(w)	—
ZSM-35	1232(sh)	1070(s)	790(w)	—
Aerosil	—	1100(s)	810(w)	—

Zeolite types	Double ring[b,c]	T-O bend[b]
Silicate	550(m)	450(s)
ZSM-5	550(m)	450(s)
Boralite	550(m)	450(s)
ZSM-11	550(m)	450(s)
Mordenite	580, 560(w)	450(s)
Ferrierite	563(w)	455(s)
Epistilbite	563(w)	455(s)
Dachiardite	558(w)	440(s)
Bikitaite	—	460(s)
ZSM-39	—	460(s)
Melanophlogite	—	465(s)
ZSM-34	635, 580, 550(w)	465(s)
ZSM-35	590(m)	460(s)
Aerosil	—	468(s)

sh, shoulder; s, strong; w, weak.
[a] IR assignments according to Ref. 48.
[b] IR assignments according to Ref. 56.
[c] 5-member ring block vibrations according to Refs. 52 and 53.
Source: Ref. 51.

Recently, Mozgawa (54) investigated in detail the vibrational (IR and Raman) spectra of natural zeolites belonging to six structural groups. It is concluded that the bands in the IR spectra of nature zeolites in the range of 760–700, 610–560, and 635–570 cm^{-1} are due to four-membered rings, five-membered rings, and six-membered rings, respectively. In the region of the so-called pseudolattice vibrations (in the range of 800–300 cm^{-1}), increase in the number of ring members results in the shift of characteristic band positions toward lower wavenumbers in the IR spectra (55). Such a tendency is not so evident in the Raman spectra. This study also proves that vibrational spectra are useful for the identification of zeolite structures. The assignments of the main IR bands in Fig. 8 are listed in Table 3 (48) and have been substantiated by data obtained for a large number of zeolites with a great variety in structure and composition. It turns out that the internal vibrations are not very sensitive to structure by comparison of spectral and structural features, whereas the position of the bands due to vibrations of external linkages is often very sensitive to structure. For example, the bands of internal tetrahedra vibrations persist when the structure of, say, a Y-type zeolite is successively destroyed by thermal treatment while the bands of the external linkage vibrations disappear following treatment.

Zeolitic vibrational spectra are usually very complicated because, in addition to the framework structure, the spectra are also influenced by other factors such as the existence and the nature of charge-balancing cations, the degree of hydration, and the Si/Al ratio. However, theoretical attempts (56–59) in recent years have proposed a modification of the approach by Flanigen et al. and a reassignment of the bands observed in the mid-IR of zeolite frameworks. Geidel and coworkers (56,57) carried out a normal coordinate analysis of the framework vibrations of NaX with the help of subunit cluster modeling. It was concluded that the Flanigen concept of strictly separated external and internal tetrahedral vibrations should be modified: Since the vibrations of zeolite framework are strongly coupled with each other, each mode is supposed to exhibit simultaneously the character of internal tetrahedral and bridging vibrations. Moreover, the coupling between adjacent tetrahedra is more significant than that within a tetrahedron.

The bands of framework vibrations are often sensitive to both the composition of the framework and the structure. For example, Jacobs et al. (60) showed that the T-O stretching frequencies of different zeolites correlate with the average electronegativity of the zeolite framework. Campbell et al. (61) reported that the frequencies of lattice vibrations could be correlated to changes in the lattice aluminum content of HMFI zeolites after hydrothermal treatment or used as a catalyst in the conversion of methanol to hydrocarbons. Figure 9 shows the plots (61) of the frequencies of the lattice modes at 544 and 790 cm^{-1}, due to deformation modes of the MFI lattice and the T-O-T stretching mode, respectively, vs. the lattice aluminum content determined by solid-state ^{27}Al and ^{29}Si NMR for fresh and treated MFI zeolites. The correlation in this case is not linear but is useful to estimate the extent of lattice dealumination.

Table 3 Assignments of Zeolite Lattice Vibrations

Internal tetrahedra	Vibrations (cm^{-1})	External linkages	Vibrations (cm^{-1})
Asym. stretch	1250–920	Double ring	650–500
Sym.stretch	720–650	Pore opening	420–300
T-O bend	500–420	Asym. stretch	1150–1050
		Sym. stretch	870–750

Source: Ref. 48.

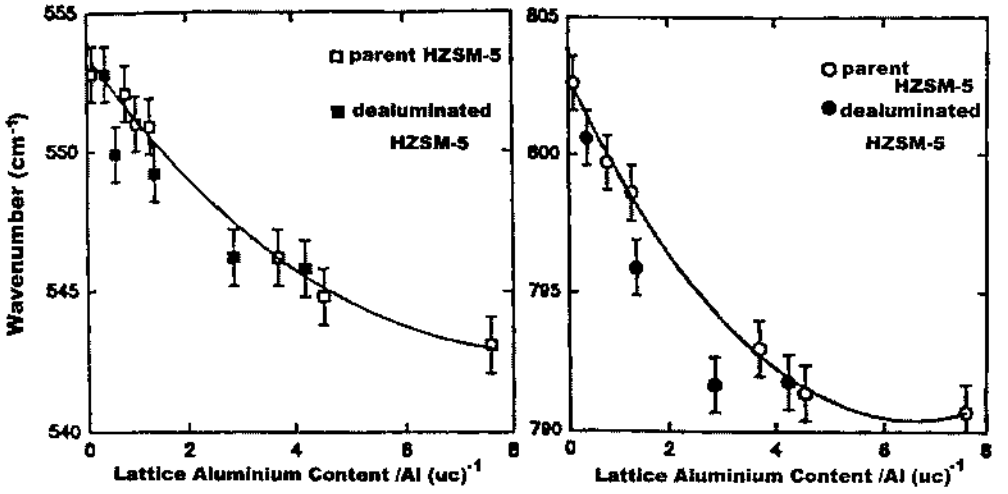

Fig. 9 Dependence of lattice frequencies on lattice aluminum content for HMFI zeolites. (From Ref. 55.)

B. Cation Vibrations

The bands of zeolites in the far-IR region (250–50 cm^{-1}) are mainly attributed to the stretching vibrations of the zeolite cations relative to the zeolite lattice. The positions of the corresponding IR bands of the cations depend on their charge, mass, as well as the interaction with the zeolite. Ozin and coworkers (62,63) carried out pioneering studies on the translational vibrations of extraframework cations in zeolites. For faujasite zeolites, they demonstrated (62,63) that a combination of the frequencies and intensities of far-IR modes of site-specific metal cation could be assigned reasonably to the metal cation vibrations for sites I, I′, II, III′, and III‴, and distinguish different cations and the occupancies and locations of cations in the zeolite framework. Esmann et al. (64) found that the IR bands of alkali metal ion-exchanged zeolites X, Y, and ZSM-5 shift to lower frequencies in the sequence of Na^+, K^+, Rb^+, Cs^+, i.e., with increasing cation size.

The charge-compensating cations within the channels and cages of zeolite also have an influence on the position of framework bands (58). For example, the antisymmetrical stretching mode at 1000 cm^{-1} in zeolite A shifts to 1080 cm^{-1} upon replacement of Na^+ by H^+ (65). The band also shifts slightly upon substitution with K^+, Li^+, and divalent cations, while much smaller shifts were reported for the symmetrical stretching bands at 675 and 550 cm^{-1}, and for the bending modes at 465 cm^{-1}. Broclawik et al. (66) found that the frequency shift of antisymmetrical T-O-T vibration of oxygen rings is sensitive to both the framework interaction with cations and the interaction with adsorbed molecules. It has been measured and estimated theoretically from parameters characterizing framework distortion by Cu^+ and Cu^{2+}, with MgZSM-5 and NaZSM-5 used as "reference samples." It is found that the ordering of the cation-perturbing effect was $Na^+ < Cu^+ < Mg^{2+} < Cu^{2+}$.

The cations in zeolites can be also identified and analyzed by employing probe molecules such as pyridine or carbon monoxide. The IR bands of pyridine coordinatively bonded to the various cations in different zeolite structures have been well studied by Ward (67). The author found a close relationship between the position of the IR band, which originates from the ν_{19b} mode of pyridine attached to a cation and the Coulomb field of this

adsorbent site. For clarity, this relationship is illustrated in Fig. 10 for a series of alkaline-metal cations in Y-type zeolites. Similar relationships were found for alkaline earth metal cations using pyridine or water as a probe (67–69), whereas for transition metal cations no simple relationship between the IR band position of adsorbed pyridine and the physcial properties of the respective cations was observed (70). When CO is adsorbed on alkali-metal (M = Li, Na, K, Rb, Cs)–exchanged zeolites (71), M^+-CO adduct is formed showing a main (cation-specific) IR band in the range 2150–2180 cm^{-1}, due to the fundamental C-O stretching mode. Meanwhile, a weaker band is often observed some 90–140 cm^{-1} higher than the main band. This weaker band can be assigned to the combination mode $\nu(CO) + \nu(MC)$ [$\nu(MC)$ is the vibration frequency of the cation–carbon bond]. This assignment is supported by direct observation of the corresponding band (at 139 cm^{-1}) for CO adsorbed on Na-Y, which was detected by using far-IR radiation from a synchrotron source (71). Observation of the combination mode is relevant to zeolite characterization by IR spectroscopy, since the cation–carbon stretching vibration is very sensitive to the specific cation present in the zeolite.

C. Hydroxyl Groups

Hydroxyl groups attached to zeolite surfaces are most important to the chemistry of the zeolitic materials because hydroxyls are associated with acidity and responsible for the catalytic activities of the acid sites of the materials. The IR spectra of hydroxyl groups have been studied extensively and described in several reviews (72,73). Hydroxyls

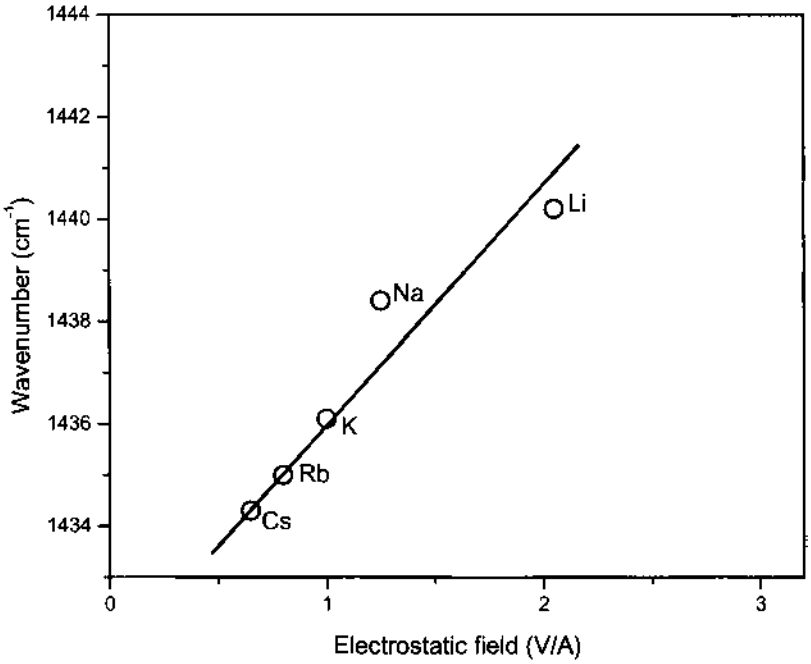

Fig. 10 Frequency of the IR band of pyridine coordinatively bound to alkali metal cations in M^+-Y. (From Ref. 69.)

typically give rise to O-H stretching frequencies around 3600 cm^{-1} as summarized in Table 4 (74–91). A problem in distinguishing different IR bands of hydroxyls in this region of the IR spectrum is the presence of adsorbed water, which suppresses the desired hydroxyl features. So the samples examined must be rigorously dried and maintained in vacuum during acquisition of the IR spectra.

A distinction is made among (a) lattice termination silanol groups, (b) OH groups occurring at defect sites (hydroxyl nests), (c) OH groups attached to extraframework T atom–containing species, (d) OH groups attached to multivalent cations that compensate the negative charge of the framework, and, most importantly, (e) bridging OH groups (e.g., ≡Al(OH)Si≡ groups with Brønsted acidic character). Hydroxyls of type a–e give rise to bands in the fundamental stretch region at about 3740, 3720, 3680, 3580–3520, and 3600–3650 cm^{-1} (free bridging OH group), respectively. As an example, Fig. 11 shows the IR spectra of ZSM-5 (MFI) with different Si/Al ratios and the resulting effect on the development of the bands due to different hydroxyls, such as the bands associated with surface silanols (~3700 cm^{-1}) and the broad band associated with hydroxyl defects within the structure (92). In fact, the relationship between ν_{OH} and Si/Al ratio may suggest a correlation between the acidic strength of the OH groups and its band wavenumber. The low values of ν_{OH} correspond to high acid strength and higher values to weak acid strength, and this semi-empirical approach has been frequently used to rationalize experimental results. However, Barthomeuf (93) concluded that the acid strength could not be correlated simply to the wavenumber of the band of acidic hydroxyl alone, but rather to the charge density of the framework that also depends on the aluminum content. Mortier (94) and Jacobs et al. (72,95) have correlated the wavenumbers of IR bands originating from acid hydroxyls in zeolites with the Sanderson electronegativity and the

Table 4 Hydroxyl Stretching Freqencies of Framework OH Groups of Zeolites

Zeolite	n_{Si}/n_{Me3+} (lattice)	ν_{OH} (cm^{-1}) (bridged OH)	Ref.
H-mordenite		3610	
H-ZSM-5		3610	
H-Y		3644	
H-ferrisilicate		3630	
Al-HZSM-5	23.8	3618	69
	35	3610	70
	65	3610	71
	24	3617	72
	13.6	3617	73
Ga-HZSM-5	29.5	3622	69
	99	3620	70
	34	3615	71
Fe-HZSM-5	35	3630	70, 71
B-HZSM-5	42	3725	70
$H_{95}Na_5Y$	2.90	3643	73
$H_{90}Na_{10}Y$	2.47	3640	74
$H_{70}Na_{30}Y$	2.50	3647	73
$H_{40}Na_{60}Y$	2.50	3648	73
$H_{20}Na_{80}Y$	2.50	3650	73

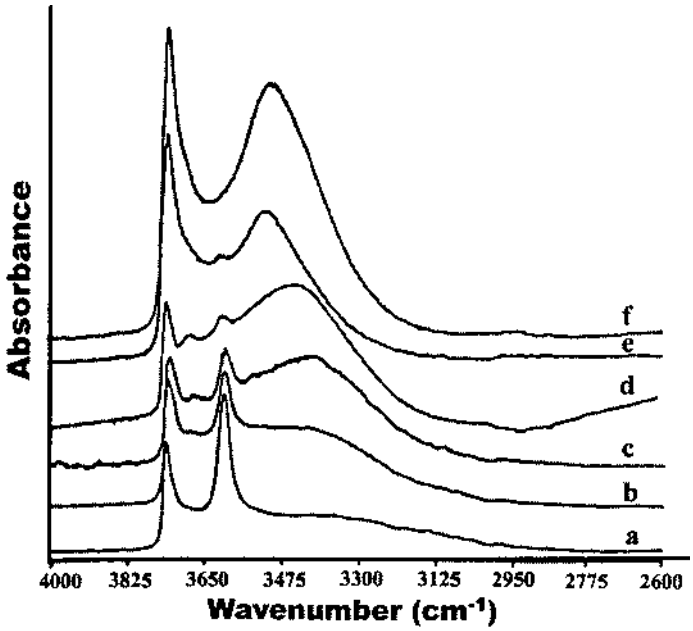

Fig. 11 IR spectra of HZSM-5 (MFI) at varying SiO_2/Al_2O_3 ratios: (a) 70, (b), 140, (c) 200, (d) 500, (e) 600, (f) 26,000. All spectra recorded at 298 K, 10^{-5} Torr. (From Ref. 81.)

acidity strengths. It was concluded that, in particular with siliceous zeolites, the ν_{OH} is not a direct measure of acidity strength (72).

In general, the framework hydroxyl group exhibiting additional electrostatic interactions due to adjacent oxygens are indicated by lower wavenumbers, e.g., at about 3550 cm^{-1} in the case of the hydrogen forms of faujasite type (X and Y) zeolites and at 3520 cm^{-1} in the case of H-ZSM-5. The band position of the hydroxyl vibration also reflects the nature of the trivalent cations in the $\equiv$T(OH)Si$\equiv$ configuration and thus can provide further evidence for structural incorporation of the T element. It is, for instance, frequently observed that the respective wavenumbers decrease in the sequence of T = Al, Ga, Fe, B (96). Such a shift correlates well with the resultant acidities of these materials.

Investigation of the overtone and combination vibrations of hydroxyl by DRIFT spectroscopy is a valuable means of characterization of zeolite materials since it frequently reveals more detailed features than those from the fundamental stretching region (97–100). The IR region above 4000 cm^{-1} includes the overtone vibrations of the hydroxyls as well as their combinations with the hydroxyl bending modes and some lattice vibrations. For instance, this range is very interesting with respect to the construction of the potential curves of the oscillators, such as Si-OH. Kazansky et al. (97) investigated a series of zeolites, including very siliceous ones, using diffuse reflectance IR spectroscopy. The IR spectra obtained in the range from 3400 to 7400 cm^{-1} are displayed in Fig. 12. It shows bands at 3610 (fundamental stretch of the bridging acidic hydroxyls, ν[Si(OH)Al]), 3745 (fundamental stretch of silanol groups, ν[SiOH]), 4540 (combination of stretching and bending, $\nu + \delta$[SiOH]), 4660 ($\nu + \delta$[Si(OH)Al]), 7065 (overtone, $\nu_{O^{2-}}$[Si(OH)Al]) and 7325 cm^{-1} ($\nu_{O^{2-}}$[SiOH]). Beck et al. (99) were able to evaluate, by careful analyses of their DRIFT spectra, the Si-OH and Si(OH)Al bending modes that appear above 4000 cm^{-1}

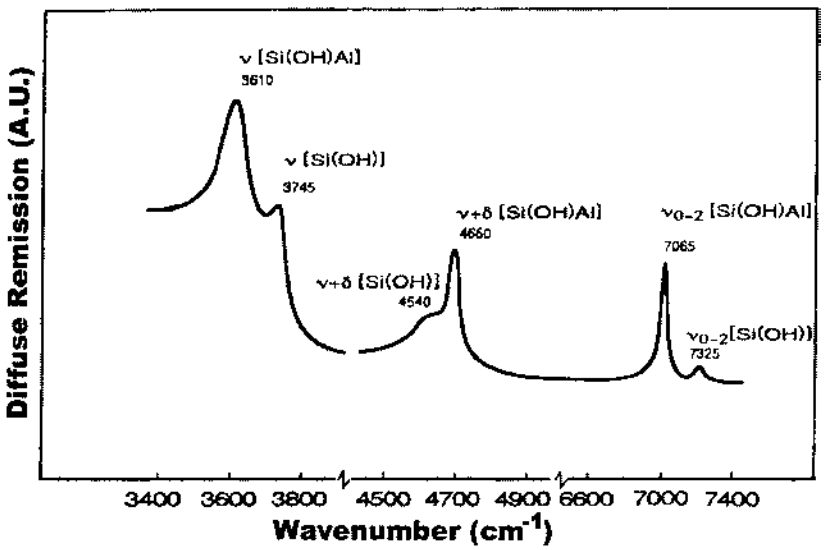

Fig. 12 Diffuse reflectance IR spectra of H-ZSM-5. (From Ref. 96.)

in combination with ν_{OH} and lattice vibration. The proposed assignments are shown in Table 5 (see also Ref. 100).

D. Acidity and Basicity Characterization

Acidity and basicity are paired concepts that are often invoked to explain the catalytic properties of zeolites. Usually, hydroxy groups (Brønsted acid or basic sites, BAS or BBS), coordinatively unsaturated (cus) cations (Lewis acid sites, LAS) and anions (Lewis basic sites, LBS, e.g., O^{2-} ions) are exposed on the surface of a zeolite. As a consequence, the surface possesses acidobasic properties. Extensive reviews on acidobasic and catalytic properties of acidic (1,2,101–109) and basic zeolites (1,2,107–112) are available. A detailed understanding of acidic or basic zeolite-catalyzed reactions requires knowledge of the

Table 5 Assignments of Combination Bands Measured by DRFIT of H-ZSM-5 and Derived Lattice Vibrations Modes (cm^{-1})

Measured frequencies	Combination vibrations	Derived assignments	Computed (80)
3614	ν(OH) of Si-OH-Al	—	—
4060	ν(OH) + δ(OTO)	δ(OTO): 446	470
4340	ν(OH) + ν_s(TO)	ν_s(TO): 726	765
4661	ν(OH) + δ(OH)	δ(OH): 1047	—
4760	ν(OH) + ν_{as}(TO)	ν_{as}(TO): 1146	1130
4800	ν(OH) + δ(OTO) + ν_s(TO)	δ(OTO) + ν_s(TO): 1186	1196
5700	ν(OH) + 2δ(OH)	δ(OH): 1043	—

Source: Ref. 79.

surface acidobasic properties in terms of quality (nature of the sites), acid and base strength, and densities of the sites.

1. Characterization of Acid Sites

An acid zeolite surface may provide protonic (Brønsted) sites and aprotonic (Lewis) sites. The former are typically structural OH groups in H forms of zeolites; the latter are *cus* surface cations or charge-compensating cations in zeolites. Thus, the acid sites are an integral part of the zeolite structure. Lewis acid sites can be derived due to several factors: (a) Heating treatment may lead to partial disintegration of the zeolite lattice and the formation of subnanoscale metal oxide particles within the channels of the microporous material (113). (b) The exchangeable metal cations affiliated with the tetrahedrally coordinated aluminum act as Lewis acid site (114). (c) Larger and, hence, accessible di-or trivalent metal cations, e.g., Co, Mg, Cr, are incorporated in the lattice (115). (d) Reversible hydrolysis of metal–oxygen bonds allows access of polar molecules to the metal cation (116). These acid sites may be detected and characterized by IR spectroscopy as such, owing to their vibration modes (OH fundamental, overtone, and combinational vibrations) or with the help of probe molecules. Direct investigations of the acid hydroxyl groups (bridging OH) have been described in detail above. This section will provide a description of the acidity of zeolites characterized by probing molecules.

Acid sites and their properties are most efficiently analyzed at a molecular level by suitably selected probe molecules. Ammonia, pyridine, and less basic molecules (e.g., CO, benzene, alkanes, C_2Cl_4, H_2, and N_2) are often used to probe acid sites of zeolites. The spectral properties of different probes are briefly described as follows.

a. Ammonia

Ammonia is probably the most frequently used probe molecule for acidity assessment. Its small molecular size allows one to probe almost all acid sites of both micro- and mesoporous zeolites. In terms of Pearson's hard and soft acid and base (HSAB) principle, ammonia is a relatively hard base and is, thus, expected to strongly interact with hard acid sites, such as protons of hydroxyl groups or small metal cations. The protonated (ammonium ion) molecule and the coordinatively bound ammonia can be differentiated spectroscopically by their NH deformation and stretching vibrations. The ammonium ion shows absorptions at 1450 and 3300 cm^{-1}, coordinatively bound ammonia at 1250, 1630, and 3330 cm^{-1}. The deformation vibrations at 1450 and 1630 cm^{-1} are often used as most reliable indicators for the presence of BAS and LAS, respectively. Thus, adsorption of NH_3 can be used to discriminate among BAS and LAS on zeolites. Such examples can be found in the recent literature (117–121).

b. Aliphatic Amines

Alkylamines are stronger bases than ammonia. Therefore, they can be used to determine the gross concentration of BAS or LAS but are not suitable for differentiation of acid strength. In general, it is possible to distinguish adsorbed protonated amines from unprotonated amines based on their IR spectra. The most frequently used molecule is *n*-butylamine. Lewis-bound *n*-butylamine gives rise to a characteristic band at 1605 cm^{-1} (-NH_2 deformation band), and protonated butylamine is characterized by IR bands at 1590^{-1} and 1510 cm^{-1}. Since the kinetic diameter of aliphatic amines can be varied by choosing different alkyl groups, the accessibility of acid sites can be probed by selecting a series of amines with varied molecular size (122).

c. Pyridine and Substituted Pyridine

Pyridine is favored as a probe molecule for quantification of BAS and LAS separately since its adsorption on BAS and LAS gives discrete IR bands. The frequencies of IR bands of pyridine interacted with acidic zeolites and their assignment are summarized in Table 6. Pyridinium ions formed via protonation of the pyridine molecule reacted with a BAS are most conveniently detected by an IR band at about 1540 cm^{-1}, whereas pyridine that is coordinatively adsorbed on a LAS gives rise to a well-resolved band at about 1450 cm^{-1} (123). Thus, pyridine is the most frequently used probe molecule to characterize the acidic properties of zeolites, e.g., beta and ZSM-20 zeolites (124), HY (125), M-ZSM-5 (MBa^{2+}, Al^{3+}, and La^{3+}) (126), MCM-41 (127,128), H-MCM-22 (129), SO_4^{2-}/ZrO_2-modified and Al-containing SBA (130), NaHMOR (131), etc.

Pyridine is a strong base, which can probe almost all of the Brønsted and Lewis acid sites with various strengths. From the IR spectra of adsorbed pyridine and the extinction coefficients of the bands concerned (132), the concentration of the LAS and BAS of the zeolite can be estimated. Instead of absolute concentrations, a [BAS]/[LAS] ratio is often derived from the spectra:

$$[\text{BAS}]/[\text{LAS}] = A_{\text{py-B}}/A_{\text{py-L}}(\varepsilon_{\text{py-L}}/\varepsilon_{\text{py-B}}) \tag{18}$$

where $A_{\text{py-B}}$ and $A_{\text{py-L}}$ represent the absorptions at about 1540 and 1450 cm^{-1}, respectively, and $\varepsilon_{\text{py-L}}$ and $\varepsilon_{\text{py-B}}$ are the respective extinction coefficients. An often used value for the extinction coefficient ratio, $\varepsilon_{\text{py-L}}/\varepsilon_{\text{py-B}}$, is 1.50 (132).

Alkyl substitution of pyridine in the 2- and 6-position enhances the base strength but induces steric constraints in coordination to acid sites, as the electronic lone pair of the nitrogen atom is shielded by the alkyl groups, This makes it very difficult to achieve the optimal adsorption geometry necessary for strong bonding to LAS, especially to those located on low index surface planes. Adsorption of the bulky probe molecule on the more exposed and also mobile hydroxyl groups seems easier. Thus, it was suggested that 2,6-dimethylpyridine be used as a specific probe molecule for characterizing BAS (133,134).

In summary, pyridine and substituted pyridines are excellent probe molecules that allow us to differentiate the acidity and the strength of the acid sites and to tell the differences between BAS and LAS.

d. Nitriles

Nitriles are relatively weak bases and coordinate via the nitrogen of the nitrile group to the acid sites. Upon interaction, the IR band of the CN stretching vibration is shifted to higher wavenumbers. Coordination to accessible metal cations results in upward shifts of approximately 30–60 cm^{-1} (135), whereas upon coordination to a hydroxyl group shifts of

Table 6 IR Region (1700–1400 cm^{-1}) of Pyridine Adsorbed on Solid Acids

Hydrogen-bound pyridine	Coordinatively bound pyridine	Pyridinium ion
1400–1477	1447–1460	
1485–1490	1488–1503	1485–1500
		1540
1580–1600	~1580	
	1600–1633	~1640

approximately 10–30 cm^{-1} are observed (136). Because of its small size, acetonitrile is frequently and successfully used for probing the acid sites of zeolites (91,137–139).

e. Less Basic Molecules (Hydrocarbons, CO, N_2, etc.)

Due to their weak base strength, hydrocarbons, CO, and N_2 are undoubtedly much more specific than strongly interacting probes. Therefore, in principle they can be used to detect the acid strength distribution via the different interaction between the probe molecules and the acid sites. Upon interaction of a hydroxyl group with the π electrons of olefins, CO, or N_2, the O-H stretching frequency undergoes a bathochromic shift, with the extent of the shift increasing with the acid strength.

CO, with its small kinetic diameter and molecular size, can reach all BA sites of many zeolites and can be used to probe zeolites with a high concentration of BAS. The carbonyl stretching frequency in CO is sensitive to the interactions with LAS and is suitable for the determination of the LAS strength (140). Due to its weak basicity, low-temperature adsorption experiments are necessary for more quantitative studies (1,80,81,141–148). CO forms H-bonded complexes with hydroxyl groups. These H-bonding interactions can easily be detected by IR spectroscopy in the O-H and C-O stretching regions. Table 7 summaries the O-H stretching frequency shifts $\Delta\nu_{OH}$ as induced by low-temperature adsorption of CO for several types of hydrogen-exchanged zeolites. By a comparison of the shifts, the following sequence of Brønsted acidities can be predicted:

$$[Al]\text{-HZSM-5} > [Ga]\text{-HZSM-5} \approx [Fe]\text{-HZSM-5}$$

This sequence was found to be consistent with the catalytic activities of the three zeolites for the disproportionation of ethylbenzene (143). The data in Table 7 also demonstrate that the acid strength of HNa-Y zeolites increases with decreasing Na^+ content and that the acid strengths of [Ga]- and [Fe]-HZSM-5 fall into the range of the highly H^+-exchanged Y zeolites.

Table 7 O-H Stretching Frequencies of Zeolites Prior to and After CO Adsorption at Liquid N_2 Temperature and the Corresponding Frequency Shifts $\Delta\nu_{OH}$

		ν_{OH}/cm^{-1}			
Zeolite	n_{Si}/n_{Me}	Free OH	O-H $\cdots$ CO	$\Delta\nu_{OH}/cm^{-1}$	Ref.
[Al]-HZSM-5	13.6	3617	3305	312	120
	24	3620	3305	315	121
	26.8	3618	3305	313	122
	27	3621	3314	307	123
[Ga]-HZSM-5	29.5	3622	3330	292	122
[Fe]-HZSM-5	35	3637	3348	289	124
H-MOR		3609	3315	294	125
$H_{70}Na_{30}$-Y	2.90	3652	3377	275	126
$H_{95}Na_5$-Y	2.90	3643	3347	296	120
$H_{70}Na_{30}$-Y	2.50	3647	3369	278	120
$H_{20}Na_{80}$-Y	2.50	3650	3385	265	120
$H_{90}Na_{10}$-Y	2.47	3640	3350	285	120

CO can also interact with charge-balancing cations, which may be considered as LA sites. The cations in zeolite cages or channels act as strong electric fields and thus attract and polarize adsorbed CO, resulting in IR shift to higher frequency relative to the frequency in gas phase (2143 cm^{-1}). Figure 13A shows a series of IR spectra of adsorbed CO on LiY, NaY, KY, RbY, and CsY zeolites (2). As shown in Fig. 13B, the frequency shift $\Delta\nu_{CO}$ linearly decreases with increase in cation radius. This suggests that the frequency of adsorbed CO is influenced by the electric field strength of cations in zeolites. When adsorbing CO on M^+-ZSM-5 (M^+Na^+, K^+, Rb^+, and Cs^+), very similar spectra were obtained (149) and the $\Delta\nu_{CO}$ values have a linear correlation with $1/(R_x + R_{CO})^2$ (this being proportional to the electric field strength F), where R_x is the cation radius. The CO probe can thus be applied for the determination of the electric field strength produced by cations in zeolite cages.

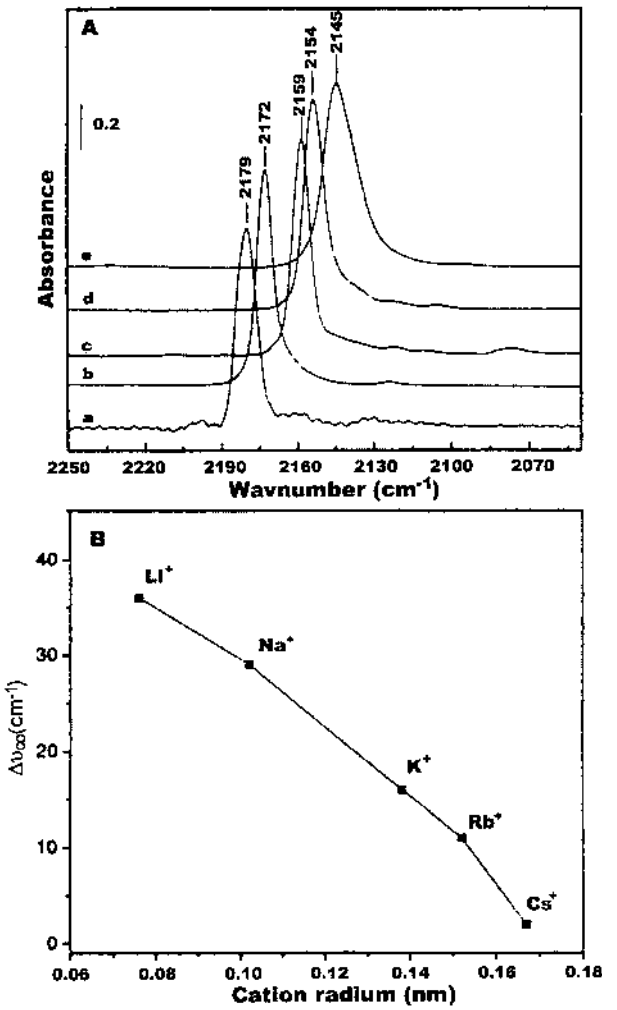

Fig. 13 Interaction of CO with exchangeable alkali metal cations in Y-zeolites: (A) carbonyl IR spectra of CO adsorbed on (a) LiY, (b) NaY, (c) KY, (d) RbY, (e) CsY at 0.5 mbar and ~90 K; (B) Correlation of C-O stretching frequency shift with cation radius. (From Ref. 2.)

Busca and coworkers carried out detailed studies on the interaction of hydrocarbons with zeolites (150–152). For the interaction of hydroxyl groups of HZSM-5 with different classes of hydrocarbons, the shifts of the O-H stretching bands, $\Delta\nu_{OH}$ (which can be taken as a measure of the strength of the hydrocarbon–site interaction), are reported in Table 8. Steric hindrance effects have been observed for the interaction between aromatics and the internal OHs in HZSM-5. Analysis of the data reported in Table 8 provides further evidence for such steric hindrance effects. In fact, the olefins interact more strongly than aromatics with the internal OHs but less strongly than aromatics with the external OHs. This suggests that the aromatic–OH interactions are partly hindered in the internal zeolite cavities.

The N_2 molecule, isoelectronic with CO, is highly specific as a probe for strong acid site (2) and the gas phase N_2 does not contribute to the IR spectra. It has often been used as a probe molecule at low temperatures for characterizing surface acidity of HY zeolites (153), H-mordenite (154), [Al]-HZSM-5 (143,155), [Fe]-HZSM-5 (156), CoAPO-18 (157), and MCM-22 (145).

Makarova et al. (132) gave an elegant example of the use of IR spectroscopy for quantitative studies of zeolites and aluminophosphates by the adsorption of weak bases. Their results, summarized in Fig. 14, show that Ar, H_2, O_2, N_2, CH_4, C_2H_6, C_3H_8, CO, and C_2H_4 probe molecules interact with the Brønsted hydroxyl groups of H-ZSM-5 and form a kind of weak acid–base complex in the zeolite. The spectroscopic features are linearly correlated by the equation $\Delta A/A_0 = 0.018\Delta\nu_{OH}$, in which A_0 represents the initial IR band intensity of OH groups (before the adsorption), and ΔA and $\Delta\nu_{OH}$ represent the variation of the OH intensity and the frequency shift, respectively, after the interaction with the base molecules.

In summary, the nature of the acid sites (BAS vs. LAS) of zeolites can be clearly distinguished by the adsorption of pyridine or ammonia, whereas the distribution of site strength can be determined by adsorption of weaker bases (benzene, CO, N_2, etc.).

2. Basicity Characterization

Basic sites on zeolite surfaces may be constituted by surface OH^- (Brønsted base, BB) or O^{2-} (Lewis base, LB) anions. In aluminosilicate zeolites, BBS, i.e., framework basic OH

Table 8 Position and Shift of OH Stretching Bands of HZSM-5 upon Hydrocarbon Adsorption

		Bridging internal OHs (cm^{-1})		Terminal external OHs (cm^{-1})	
Adsorbate	T(K)	ν_{OH}	$\Delta\nu_{OH}$	ν_{OH}	$\Delta\nu_{OH}$
None	170	623	—	3749	—
	300	3612	—	3746	—
Butenes	170	ca.3000	~600	3500–3520	220-245
Propene	170	ca.3080	~540	~3560	ca.190
Ethylene	179	ca.3230	~390	3580	ca.170
p-Xylene	300	3185	~430	3500	ca.245
o-Xylene	300	3612	—	3500	ca.245
Toluene	300	3200	~400	3500	245
Benzene	300	3250	~350	3510	235
n-Heptane	300	3460	150	3650	95
n-Butane	300	3485	130	3650	95
i-Butane	300	3560, 3500	50, 110	3665	80

Source: Refs. 130 and 131.

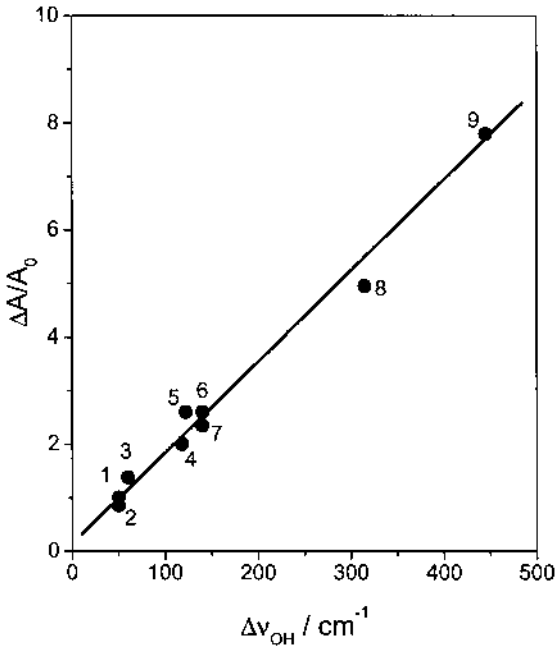

Fig. 14 Variation of the OH intensity ($\Delta A = A_{OH...B} - A_{OH}$) after the interaction with Ar (1), H_2 (2), O_2 (3), CH_4 (4), N_2 (5), C_2H_6 (6), C_3H_8(7), CO (8), and C_2H_4 (9) plotted against the frequency shift ($\Delta\nu_{OH}$). $A_0 = A_{OH}$ is the OH intensity before the interaction. (From Ref. 132.)

groups, do not occur. Hydroxyls with basic properties may behave as ligands coordinated to nonframework charge-compensating multivalent cations. There are several possible ways to produce basic sites in aluminosilicate zeolites, such as exchange of alkali metal cations, deposition of clusters of alkali metals in the pores of faujasite-type zeolites, and deposition of occluded oxides.

The studies of basic sites are far less extensive than those of acidic sites because the acidic zeolites are more important in petroleum chemistry and a large number of basic molecular probes are available for characterizing the acid sites. Carbon dioxide and pyrrole are frequently used probes to characterize the basis sites of zeolites. IR studies on the adsorption of these two probes on zeolites are described as follows.

a. Carbon Dioxide

CO_2 adsorption on alkaline zeolites has been widely studied. An IR band generally appears at about 2360 cm^{-1} due to the asymmetric stretching vibration ν_3 of adsorbed CO_2, and its intensity is pressure dependent. The higher the polarization strength of the cation ($Li^+ > Na^+ > K^+ > Rb^+ > Cs^+$), the more pronounced is the shift of this band to higher frequencies. CO_2 can also be chemisorbed on zeolites to form carbonate species (158–161). When CO_2 is adsorbed on X-type zeolites, a pair of bands at 1711 and 1365 cm^{-1} was observed. These bands have been assigned to the bicoordinated CO_2 (species I) to both a T atom and a residual cation. The bicoordinated species can be converted to a true carbonate structure (species II) (shown in Fig. 15), characterized by bands at 1488 and 1431 cm^{-1} (162).

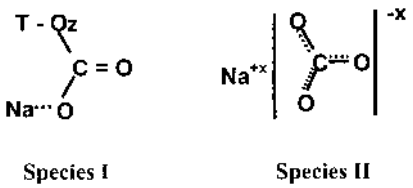

Fig. 15 Two species formed from CO_2 adsorption on X-type zeolites. (From Ref. 162.)

The formation of carbonate species from CO_2 adsorption proves that alkaline zeolites possess O^{2-} basic sites. They are less abundant in Y than in X zeolites. This could be attributed to the higher Si/Al ratio in the former, leading to a lower average negative charge on the lattice oxygen anions.

b. Pyrrole

Barthomeuf (111) studied pyrrole adsorption on faujasite, L, and mordenite zeolites with different alkali–metal cations. The frequency shift $\Delta\nu_{NH}$ was used to monitor the framework basicity and correlated well with the charge on oxide ions as calculated with the Sanderson electronegativity equalization principle. The wavenumber of the ν_{NH} vibration mode decreases when the negative charge on oxide ion increases. Investigations by Huang et al. (163) and Lavalley (112) confirmed that the basic strength of cationic zeolites increases in the order Li < Na < K < Rb < Cs, which is shown in Fig. 16 where a bathochromic shift of ν_{NH} is observed. They specified that basic sites are framework oxygens adjacent to the exchanged cations.

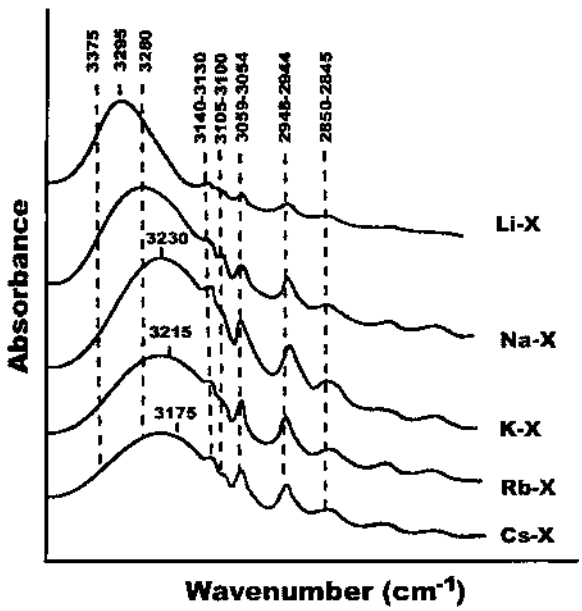

Fig. 16 IR spectra of the N-H stretching region of alkali metal exchanged X-type aluminosilicates (FAU topology) after adsorption of pyrrole. (From Ref. 163.)

For faujasite zeolites exchanged with alkali metal cations, Barthomeuf (111) established a ranking according to acid and base strength using the pyridine and pyrrole probes by IR spectroscopy. Table 9 reflects that the faujasites constitute a family of solids with dual acid–base properties, since an increase in base strength is inevitably coupled with a decrease in acid strength (and vice versa). These materials can be regarded to have amphoteric properties.

Using pyrrole as probe molecule, Murphy et al. (164) reported the basicity of Na-EMT zeolites exchanged with alkali–metal cations. The envelope of ν_{NH} stretching vibrations of adsorbed pyrrole could be deconvoluted into different components. By considering the relative intensities of these bands and the population of cations over the possible positions, the IR bands could be assigned to pyrrole interacting with specific cation coordination sites. The strongest basic sites are located in the supercages, the weakest ones in the hexagonal prisms and the sodalite cages. Some recent investigations using pyrrole as probe molecule to detect the basic properties of zeolites are reported (165–167).

Liu et al. (168) showed that boric acid trimethyl ether (BATE) can be used as a novel probe molecule to detect LB sites of zeolites and their basic strength. $B(OCH_3)_3$ is a typical Lewis acid with a planar geometry. Strong interaction with surface oxygen anions would convert its planar structure into a pyramidal one, leading to the splitting of the degenerate vibration at 1360 cm^{-1} involving the B-O bond into two bands and the shift toward higher wavenumbers of the ν_{CO} band at 1036 cm^{-1}. Figure 17 displays the IR spectra of BATE adsorbed on Al_2O_3/SiO_2, NaY, and HY. The species in Y zeolites with bands at 1373 and 1320 cm^{-1} are assigned to BATE interacting with the framework oxygen anions. The splitting of bands at 1373 and 1320 cm^{-1} is stronger for HY than NaY, which is explained by the fact that the average basic strength of basic sites in NaY may be stronger than that in HY, but the basic sites in HY are not as uniform as NaY and the basicity of some sites in HY may be even stronger than that in NaY. This study shows that different basic sites and different forms of zeolites could be distinguished using BATE as a probe by IR spectroscopy.

Other acid probes, e.g., SO_2 (169), Cl_3CH (170), acetylene (2), H_2S (171), methanol (172), etc., were also employed to characterize the basicity of zeolites. SO_2, being more acidic than CO_2, is less specific for the adsorption sites (173). Chloroform does not appear to be a sensitive probe and it partially decomposes on basic sites, giving rise to surface formate species (174). Adsorption of molecules like alcohols and thiols on basic surfaces is unsuitable to the study of basic sites because spectra are not directly correlated with the

Table 9 Ranking of Alkali Meta–Exchanged Faujasite Zeolites According to Their Acid and Base Properties

	Acid	Base	
	↑ LiY		
Increasing acid strength	NaY		
	NaX	KY	
	KY	RbY	
		NaX	Increasing basic strength
		KX	
		RbX	
		CsX ↓	

Source: Ref. 111.

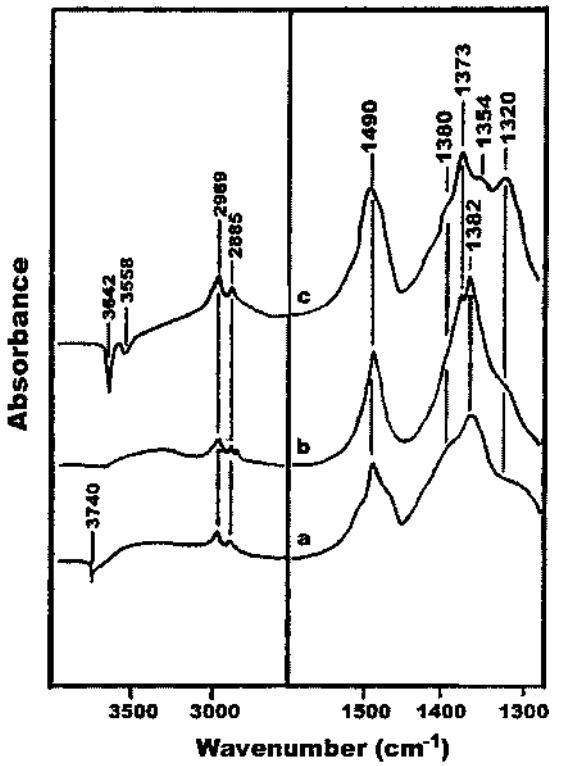

Fig. 17 IR spectra of BATE adsorbed on (a)Al_2O_3/SiO_2 (1:2), (b) NaY, and (c) HY after evacuation at 298 K for 15 min. (From Ref. 168.)

surface basicity due to the dissociative adsorption of these molecules. In such case, IR spectroscopy is only informative on the nature of species formed (112).

In conclusion, characterization of the acidity and basicity of zeolites can be established by IR spectroscopy of adsorbed probe molecules. Many potential probe molecules have been investigated in detail for a wide variety of zeolite samples. For most of these molecules consensus has been reached with respect to the interpretation of the IR spectra and their role in assessing the acid and base strength of zeolites. Currently, evaluation of the sorbate-sorptive interactions and the corresponding IR spectra by theoretical calculations (175,176) are becoming available.

The strength of the interaction between probe molecules and the acidobasic sites is often taken as a measure of the acid–base strength and then the catalytic activity. For example, Sigl et al. (144) demonstrated that the strength of an H-bonding interaction between the acidic group and weak bases, e.g., H_2, N_2, and CO, correlates very well with the catalytic activity of isomorphously substituted MFI zeolites for the acid-catalyzed disproportionation of ethylbenzene. However, Farcasiu et al. (177) demonstrated that a correlation of the hydrogen bond donor ability with the acid strength and catalytic activity of acid catalysts is not cogent unless there is a close structural similarity of the participating acids and bases. Very recently, Kotrel et al. (178) compared the acid strength of four types of zeolites (by adsorption of H_2, N_2, and CO using IR spectroscopy) with their intrinsic activities for the acid-catalyzed cracking of *n*-hexane. It is found that

catalytic and spectroscopic characterization of the acidity is consistent only within the same class of zeolites, e.g., comparison of differently pretreated faujasites. Spectroscopic and catalytic observations for different types of zeolites do not match perfectly because additional effects, such as interactions of larger molecules with pore walls and the stabilization of transition states and intermediates, can influence the course of an acid-catalyzed reaction. The discrepancies between spectroscopic and catalytic results draw attention to additional factors that would have been missed had the zeolitic acidity be monitored by only one of the two techniques.

Therefore, although the use of IR spectra of adsorbed probe molecules allows general measurement of the strength and the concentration of acid and base sites of zeolites, it is not straightforward to use these data to estimate the turnover frequencies of a reaction or to predict catalytic behavior. This is due to the fact that the probe molecule and the reactant interact with the catalyst surface in a different way. IR spectroscopy combined with proper probe molecules chemically similar (in shape, polarizability, and acid or base strength) to the reactants is an important way to understand the acid–base properties of zeolites (112). However, it is strongly recommended the reactant molecules themselves be used (if possible) to probe the acid–base properties of the catalyst, if the acidity or basicity scale can directly correlate to the catalytic activity. The combination of spectroscopic experiments with theoretical calculations should facilitate the assessment of the acidity and basicity of zeolites and, in turn, to provide ways of fine tuning and optimizing their acid–base properties for a particular use in catalysis.

E. Adsorbed Molecules and Intermediates Formed in Microporous Materials

1. H/D Exchange

H/D exchange between surface OH groups and adsorbate molecules is a valuable method for the investigation of acid strength of OH groups and the mechanism of acid-catalyzed reactions. Lee et al. (179) investigated the H/D exchange between several light alkanes, i.e., CH_4, C_2H_6, C_3H_8, and C_6H_{14}, with the acidic OH groups of deuterated ferrierite. By comparison of the activation energies of the H/D exchange reaction determined experimentally (130–143 kJ/mol) with data calculated by quantum mechanical methods, the authors derived a reaction mechanism which involves a neutral transition state.

Kondo et al. (180–183) studied the mechanism of the double-bond migration of 1-butene on mordenite and ZSM-5 zeolites. With deuterated zeolites the authors were able to establish a mechanism in which a reaction to *cis*- and *trans*-2-butene occurred starting from the π complex of 1-butene on Brønsted acidic OD groups even below 230 K without an H/D exchange of the acidic OD groups. Namely, at temperatures below 230 K, the DBM of 1-butene occurs without the formation of protonated intermediate species. This process is depicted in Fig. 18A. The isotope exchange reaction of the hydrogen-bonded OD group took place above 230 K, as evidenced by the decrease in the intensity of the OD stretching band and the simultaneous increase of the OH stretching band of the π complex. In this temperature range almost all of the adsorbed 1-butene had already transformed to the adsorbed 2-butenes. Therefore, the isotope exchange reaction of the hydrogen-bonded OD to OH groups is regarded as a result of the reaction with the adsorbed 2-butenes (Fig. 18B).

On D-ZSM-5 zeolite (183), H/D isotope exchange reaction of Brønsted acid sites with the adsorbed 2-butene proceeds in parallel with the cis-trans isomerizaton of

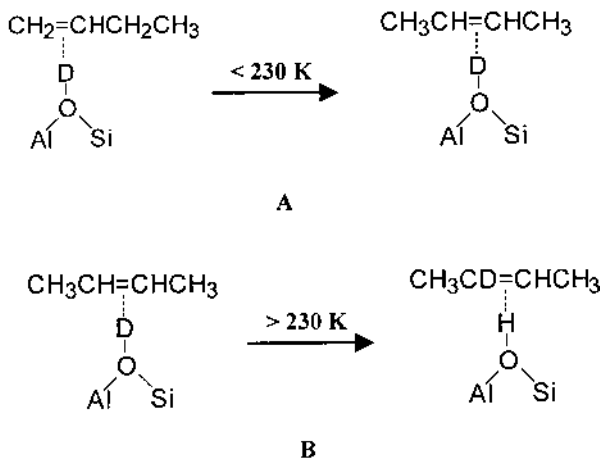

Fig. 18 Mechanisms of DBM of 1-butene over ZSM-5 at temperatures (A) below 230 K and (B) above 230 K. (From Refs. 180 and 181.)

2-butenes below 270 K, and the existence of a common alkoxy intermediate is suggested. The adsorbed 2-butene is found to be mobile below the temperature of alkoxy formation, which results in a successive dimerization. The reaction of 2-butene adsorbed on D-mordenite is found to allow more bulky paraffinic alkoxy species even at temperatures as low as 230 K due to less restriction from the larger pore size.

Kotrla et al. observed the formation of dimethylketimine [$(CH_3)_2C{=}CNH$, DMKI] in the reaction of acetone and ammonia on the acidic zeolites H-ZSM-5, H-Y, H-beta, and H-mordenite (184). An IR band at 1707 cm^{-1} was assigned to the C=N stretching band of the $>C{=}NH_2^+$ group of the protonated $DMKIH^+$, which forms ion-pair complexes with framework oxygen anions. This assignment was confirmed by a H/D exchange between the catalysts and the reactants as the C=N stretching band shifts from 1707 to 1683 cm^{-1} of the $>C{=}NHD^+$ group.

After a study of the low-temperature adsorption (175 K) of methane over H-ZSM-5 zeolite, Chen et al. (185) carried out the adsorption of deuterated methane (CD_4) at high temperatures (673–873 K) on H-ZSM-5 in order to clarify whether the hydroxyl groups also play an important role in the activation of methane at high temperatures. The spectra are illustrated in Fig. 19. Reverse bands at 3757 and 3590 cm^{-1} and new bands at 2750 and 2635 cm^{-1} appear simultaneously when the temperature is higher than 773 K. The O-D bands at 2750 and 2635 cm^{-1} are obviously from the exchange of CD_4 with the terminal silanol hydroxyl groups at 3757 cm^{-1} and the bridging hydroxyl groups at 3590 cm^{-1}, respectively. Thus, the authors supposed that during the interaction of CD_4 with H-ZSM-5, the C-D bond breaks first, followed by the exchange with hydroxyl groups present on the zeolite.

2. Adsorption and Reaction of Hydrocarbons

a. Acid-Catalyzed Reactions

SKELETAL ISOMERIZATION OF *N*-BUTENES. Because of the need for isobutene in the synthesis of methyl tert-butyl ether (MTBE), the isomerization of *n*-butene to produce isobutene has been the focus of many investigations (186–190) in recent years. Ferrierite

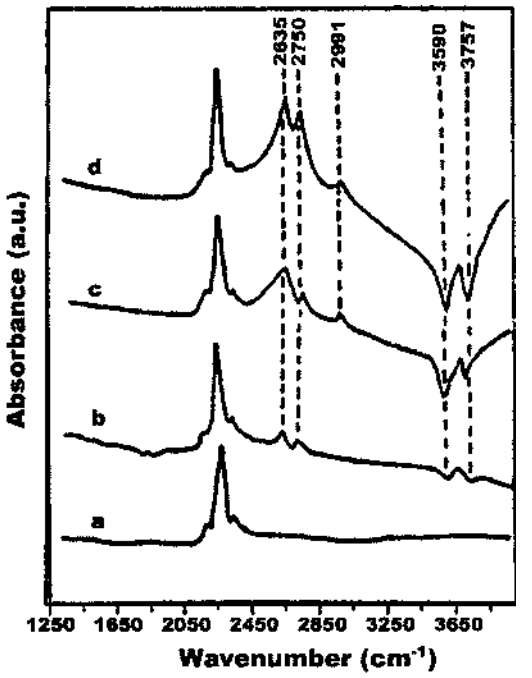

Fig. 19 IR difference spectra depicting the exchange of CD_4 with the OH groups of H-ZSM-5. (a) 673 K, (b) 773 K, (c) 873 K, 5 min and (d) 873 K, 20 min. (From Ref. 185.)

(FER) has exceptional selectivity for isobutene in the skeletal isomerization process of *n*-butene and gained a successful commercialization in 1993 (187). The specific pore structure of FER zeolite composed of 8- and 10-membered rings is considered to be a plausible cause bringing about the selective skeletal isomerization of *n*-butene (191).

Seo et al. (192) investigated the adsorption of butene on four types of zeolites [FER, clinoptilolite (CLI), ZSM-5 (MFI), and beta (BEA)] with different pore structures and acidities with an attempt to elucidate the reaction mechanism of the skeletal isomerization. The IR spectra of butene adsorbed on zeolites recorded with heating (shown in Fig. 20) are different according to their pore structures. The formation of polymeric species on MFI and BEA zeolites (Fig. 20A) is confirmed by a band at 1505 cm^{-1} that is absent in the spectra on FER and CLI zeolites (Fig. 20B). IR spectra recorded under the reaction conditions suggest that the molecularity of the predominant reaction on zeolite catalyst is dependent on its pore structure, and the difference in the molecularity induces the difference in the selectivity. FER and CLI zeolites, both showing good selectivity to isobutene, have a similar two-dimensional channel system consisting of 10-rings intersected by 8-rings (193), so the cross-sectional area of the pore must be reduced periodically. The potential energy of an adsorbed butene molecule approaches its minimum at the channel intersection; thus, butene molecules are sparsely distributed in the pore of FER and CLI zeolites. The sparse distribution suppresses bimolecular oligomerization, enhancing the monomolecular skeletal isomerization. While the pore of the MFI zeolite is composed of 10-rings and that of the BEA zeolite 12-rings (194), the potential barrier of these two zeolites for transfer of the butene molecule along the pore is negligible compared to that of FER and CLI zeolites. The easy transfer of activated butene molecules brings

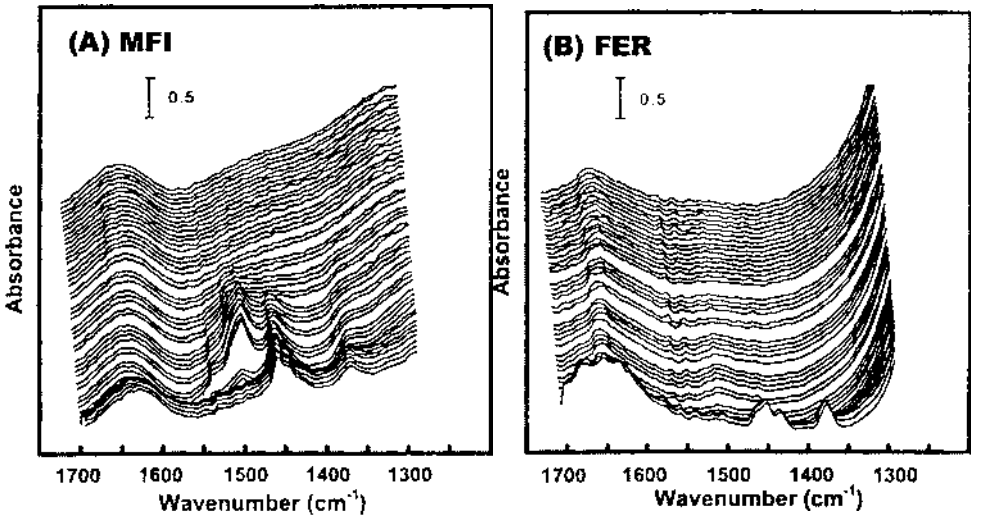

Fig. 20 Three-dimensional IR spectra of adsorbed 1-butene on MFI (A) and FER (B) zeolites. Zeolite was exposed to 1-butene at 303 K and evacuated with temperature increasing to 823 K with a ramp of 16 K/min. (From Ref. 192.)

about collision with each other and formation of oligomers. Various hydrocarbons are produced from oligomers, thus showing low selectivity for isobutene.

Ivanov et al. (195) compared the adsorption and reaction of 1-butene, *cis*- and *trans*-2-butene, and isobutene on silicalite, H-ZSM-5, and H-FER by IR spectroscopy. On silicalite the different butenes are only physisorbed and no interaction takes place. Over H-ZSM-5, hydrogen-bonded *cis*- and *trans*-2-butenes are initially formed followed by dimerization. Over H-FER, the adsorbed 1-butene is converted to *cis*- and *trans*-2-butenes which are hydrogen bonded to the acidic OH groups of the zeolite, and no further dimerization is found. Since the Brønsted acidity of H-FER and H-ZSM-5 is comparable, it is concluded that the pore size and pore structure but not the acidity play the important role for the observed behavior. A monomolecular mechanism is proposed for the isomerization of *n*-butenes to isobutene over the H-FER and H-ZSM-5 zeolites.

Pazé et al. (196) studied the interaction of 1-butene with zeolite H-FER at increasing temperatures (300–673 K) with the aim of isolating the precusor species to isobutene and high-temperature coke under in situ conditions. Since low branched C_8 chains are observed, the bimolecular mechanism of coversion of butene to isobutene on the fresh catalyst is confirmed. From the reaction of the protonated intermediate with butene, two reaction paths are hypothesized: (a) a butene hydride abstraction, with formation of dienic carbocations, and (b) dimerization to form octane carbocations and (by successive cracking) isobutene. The reaction of allylic carbenium ions with butene molecules, followed by H transfer, leads to the formation of long, unsaturated, resonant neutral and carbocationic chains. At temperatures $\geq$623 K, these unsaturated chains cyclize to form mono- and polycyclic aromatics, the precusors to coke.

Wichterlová et al. (197) studied the effect of the presence of Brønsted and Lewis sites in ferrierites on the skeletal iosmerization of *n*-butene to isobutene and other products. Results show that the formation of isobutene by skeletal isomerization of *n*-butene in H-FER is proportional to the concentration of bridging OH groups (Brønsted sites) present in

10-member ring main channels of ferrierite accessible to isobutene molecules, in contrast to OH groups in eight-member ring channels. The presence of Lewis sites changes substantially the selectivity of the reaction, supporting their catalytic function in transformation of *n*-butenes, besides their possible enhancement of the strength of the Brønsted sites.

XYLENE ISOMERIZATION. Xylene isomerization on zeolites has been often studied in situ by IR spectroscopy because it is a good model for hydrocarbon isomerizations and because of its industrial interest. Figure 21 shows time-resolved difference spectra measured on exposure of H-ZSM-5 to flowing *o*-xylene at 473 K (198). These spectra show the rapid initial adsorption of the reactant onto Brønsted acid sites (the negative peak in the difference spectra at 3610 cm^{-1}) and slower development of bands due to adsorbed *m*-xylene. After 1 h on steam approximately 15% of the acid sites are covered with *m*-xylene molecules. Under steady-state conditions, all three isomers of xylene react at the same rate (gas chromatographic analysis) and give the same surface concentrations at 473 K, namely, at this temperature surface reaction and not reactant diffusion is the rate-limiting step. At higher temperatures (e.g., 573 K) the diffusivity of the reactant molecules begins to influence the overall reaction rate and the concentrations of adsorbed molecules increase in the order *m*-xylene < oxylene < *p*-xylene. The results are considered to be completely consistent with a unimolecular 1,2-methyl shift mechanism for the isomerization reaction.

Mordenites have been applied industrially to xylene isomerization and the catalysts employed contain Na^+ ions in such an amount as to eliminate acidic OH groups in the side pockets (199), acid being therefore only present in the main channels. Marie et al. (200), using an in situ IR approach, investigated the catalytic role of the various acid sites of acidic mordenites in *o*-xylene conversion. Xylene conversion measured in constant contact time or isoconversion conditions indicates an increase of initial disproportionation selectivity with proton content in NaH-Mor. The presence of acidic OH groups inside the side pockets seems to benefit the disproportionation selectivity. However, accessibility measurements show that the OH groups located inside the side pockets are never

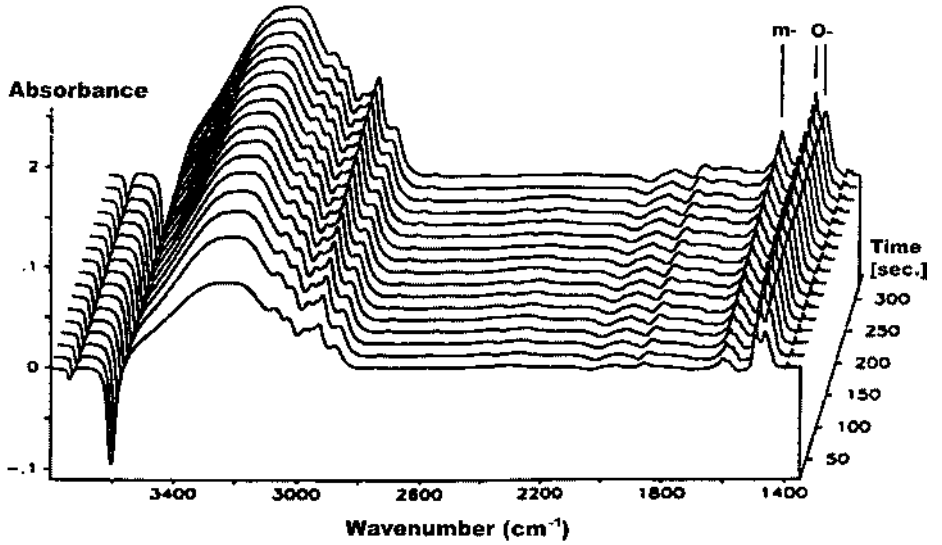

Fig. 21 Time-resolved difference IR spectra of the adsorption and reaction of *o*-xylene with H-ZSM-5 at 473 K under continuous-flow conditions. (From Ref. 198.)

accessible to the reactants. Moreover, the presence of Na^+ ions inside the side pockets does not increase the strength of acid sites in the main channels. The presence of OH groups inside the side pockets has thus an indirect effect on reaction selectivities, even leading to higher amounts of coke. It is proposed that the main effect of Na^+ substitution by OH groups inside the side-pockets is a change of global accessibility in the micropores.

Thibault-Starzyk et al. (201) applied 2D correlation IR spectroscopy (2D-COS) to the in situ IR study of *o*-xylene isomerization in H-MFI zeolite under working conditions. This approach led to improvement in the quantitative monitoring of xylene isomers in the micropores of the solid and to the detection of traces of coke in the catalyst. A correlation was found between coke and the perturbation of specific OH groups in the zeolite.

ALKYLATION. For alkylation of aromatic compounds with olefins, alcohols, and alkyl halogenids, acidic zeolites are suitable candidate catalysts (202). As the surface species generated upon adsorption of alkyl aromatics can be detected spectroscopically, Flego et al. (203) studied the adsorption of propene, benzene, their mixtures, and cumene on H-beta zeolites to follow the formation of cumene. It is found that when benzene is adsorbed alone on the zeolite surface, its adsorption is reversible up to 473 K. On the contrary, propene undergoes several transformations even at 295 K. Cumene behaves as propene, giving the same intermediates and products by decomposition at higher temperatures. Isopropyl cations formed upon chemisorption of propene on Brønsted acid sites are the key intermediates for the alkylation reaction and are responsible for the faster deactivation via unsaturated carbenium ion formation.

Flego et al. (204) studied the hydrocarbon deposition arising during the alkylation of isobutane with 1-butene on a LaH-Y zeolite. They observed a decrease in oligomerization of 1-butene with an increase in the fraction of isobutane in the reaction mixture. Attempts at desorption of the coke deposition at temperatures above 523 K led to the formation of a band at 3050 cm^{-1} attributed to aromatic compounds.

DISPROPORTIONATION. Trombetta et al. (152) investigated the interaction of toluene with H-ZSM-5 in the temperature range 300–700 K by IR spectroscopy. At 300 K, toluene does not give rise to very evident perturbations in spectra, as far as their strong IR bands are concerned. But a slight shift upward of the out-of-plane C-H modes can be observed, which is evidence that toluene adsorbs, interacting through the π-electron cloud of the aromatic ring with the zeolite hydroxyl groups, which act as electron attractors. A sharp band at 672 cm^{-1} clearly appears and grows by increasing temperature up to 673 K, typically due to the strongest IR-active band of benzene in gas phase. Also, a sharp band at 740 cm^{-1} grows upon elevating the temperature, attributed to the C-H wagging of adsorbed *o*-xylene. Thus, the disproportionation of toluene on H-ZSM-5 is clearly identified and a scheme is given in Fig. 22.

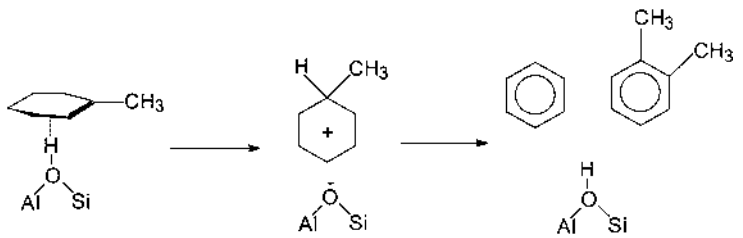

Fig. 22 A scheme for the disproportionation of toluene on H-ZSM-5. (From Ref. 152.)

The disproportionation of ethylbenzene on H-Y zeolite has been investigated by Arsenova et al. (205) under flow conditions. It was found that from the start of the reaction to the establishment of the steady state the composition of the adsorbed species on the catalyst changes continuously, with a constant decrease in the ethylbenzene concentration. After an induction period of about 1 h the steady state is reached simultaneously on the adsorbent and in the gas phase. This experimental result suggests that the induction period in the disproportionation of ethylbenzene is caused by a delayed establishment of the equilibrium between the gas phase and the adsorbate species consisting of benzene, ethylbenzene, and the different diethylbenzenes. Other acid-catalyzed reactions of hydrocarbons (206–213), recently studied by IR spectroscopy, are shown in Table 10 together with the reactions mentioned above.

b. Base-Catalyzed Reactions

Compared with the case on acid zeolites, rather few studies have been devoted to the development of zeolite catalysts for base-catalyzed reactions. One reaction investigated by several groups is the alkylation of toluene with methanol which is directed to side chain alkylation by basic zeolite catalysts. King et al. (214) studied the side chain alkylation of toluene with methanol over various alkali-exchanged X zeolites (Cs-X, Rb-X, K-X, Na-X, and Li-X). In the reaction of methanol on Cs-X, Rb-X, and K-X zeolites, IR bands of surface monodentate and bidentate formate species are observed. IR experiments show that only the surface monodentate formate species contribute to the side alkylation of toluene.

Lercher and coworkers (215) also utilized in situ IR spectroscopy to study the adsorption and reaction of toluene and methanol over Cs-X, Rb-X, K-X, and Na-X zeolites. IR studies of adsorbed and coadsorbed toluene and methanol have shown that less basic alkali-exchanged zeolites (e.g., Na-X) preferentially adsorb methanol over toluene. Methanol interacts with the cation of the zeolite primarily via the lone electron pair of the alcohol oxygen and, secondly, via the hydrogens of the OH and the methyl group with the lattice oxygens of the zeolite. In this case, xylenes appear to be the main

Table 10 Some Acid-Catalyzed Reactions of Hydrocarbons Studied by IR Spectroscopy

Reaction	Catalyst	Ref.
Skeletal isomerization of *n*-butenes	H-ZSM-5, H-FER	192–197
Xylene isomerization	H-ZSM-5, H-MFI, NaH-Mor	199–201
Benzene alkylation with propene	H-beta	203
Isobutane alkylation with 1-butene	LaH-Y	204
Toluene disproportionation	H-ZSM-5	152
Ethylbenzene disproportionation	H-Y	205
Propene oligomerization	H-mordenite	206
Polymerization of acetylene	H-ZSM-5	207
Polymerization of methylacetylene	H-ZSM-5	207
Polymerization of ethylacetylene	H-ZSM-5	207
Diels-Alder cyclodimerization of 1,3-butadiene	H-Y, Cu-Y, Cu-Beta, Cu-EMT	208
Cracking of hepane	H-Y	209,210
Dimerization of isobutene	D-mordenite	211
Amination of methanol	H-mordenite	212
Rearrangement of cyclohexanone oxime	MFI, FAU zeolites	213

products formed. More basic zeolites (i.e., Cs-X and Rb-X) preferentially adsorb toluene over methanol. Toluene interacts with the cation of the zeolite primarily via the electrons of the aromatic ring and, secondly, via the hydrogens of the methyl group with the lattice oxygens. Here the main reaction products are the alkylation ones, styrene and ethylbenzene. The IR spectra of the surface species formed during the reaction of toluene and methanol on Cs-X and Na-X zeolites are shown respectively in Fig. 23A and B. With both

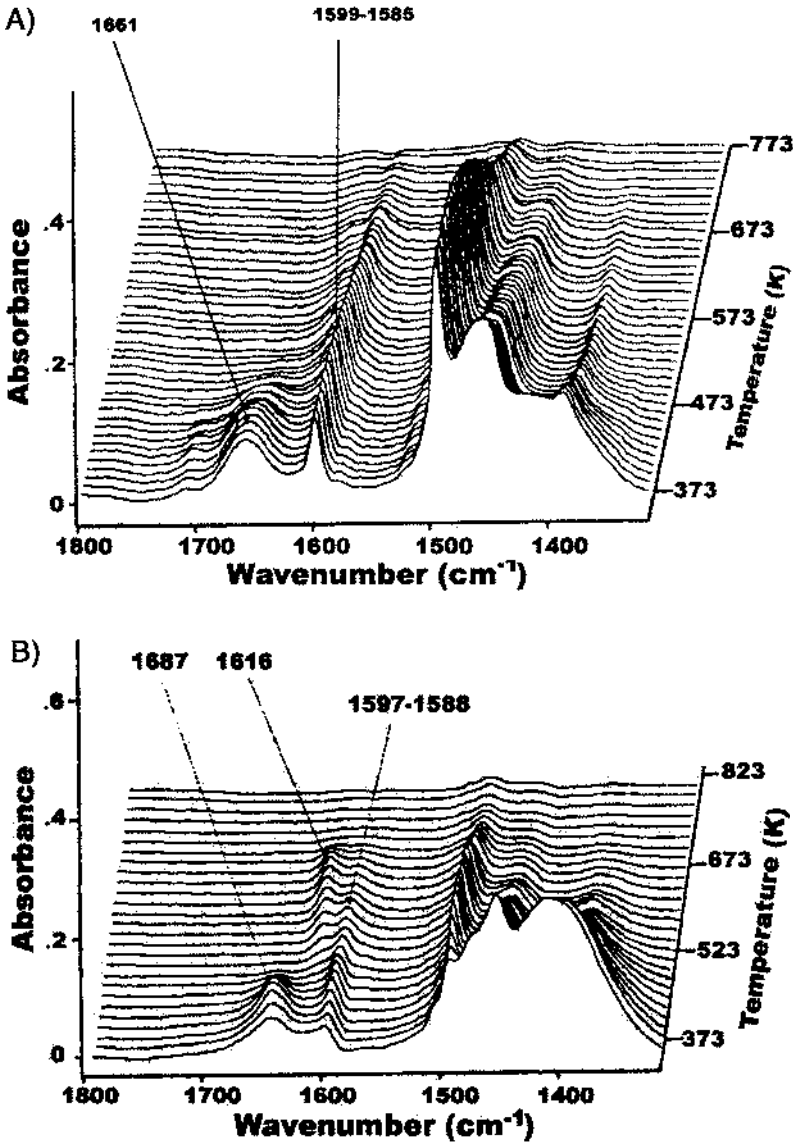

Fig. 23 (A) Difference IR spectra of Cs-*X* during the reaction of toluene and methanol as a function of the reaction temperature (T = 423–743 K). (B) Difference IR spectra of Na-X during the reaction of toluene and methanol as function of the reaction temperature (T = 423–743 K). (From Ref. 215.)

samples studied, a new band is observed around 1660–1690 cm^{-1} at 433 K. The disappearance of this band is correlated with the onset of the formation of formaldehyde in the gas phase, suggesting that this band may be due to the precursor species for the formation of formaldehyde. At 523 K, when the alkylation of toluene started, the spectra of the two zeolites show significant differences. For Cs-X, apart for the relatively intense bands characteristic of adsorbed toluene, no additional bands appear, indicating that at reaction temperature a high coverage of toluene remains in the pores of the catalyst. With Na-X, as the band at 1687 cm^{-1} disappears a new band appears at 1616 cm^{-1}, due to the formation of some type of formate on the catalyst. The different IR results lead to the conclusion that the adsorption and activation of toluene (together with the formation of formaldehyde) are the critical factors initiating the side chain alkylation of the toluene.

In a later study (216), Lercher and coworkers compared the adsorption and reaction of toluene and methanol over various basic catalysts (MgO, hydrotalcites, and alkali-exchanged X zeolites) with the purpose of knowing how to correlate the catalytic properties with the chemisorption and stabilization of the reactants at the surface of the different basic materials. Based on the IR results three requirements for an active catalyst for side chain alkylation of toluene with methanol could be formulated: (a) sufficient base strength to dehydrogenate methanol to formaldehyde, (b) sites for the stabilization of toluene and for the polarization of the methyl group of this molecule, and (c) establishment of a suitable sorption stoichiometric relationship between toluene and methanol. Cs-X is the only material that fulfills the former two conditions. The results demonstrate that side chain alkylation does not depend solely on basic properties of a catalytic material and is therefore inadequate for probing the base strength of unknown materials.

3. Environmental Catalysis

a. NO_x Reduction

In the past decades, zeolite-based catalysts, such as Cu-ZSM-5, have been extensively investigated for the selective catalytic reduction (SCR) of NO (217). In an IR study (combined with ESR and TPD) of NO reduction with propane over Cu/ZSM-5 catalysts (218), the Cu^{2+}-O-NO complex is formed on the surface of Cu-containing zeolites under reaction conditions. Its transformation rate to reaction products as measured by the spectrokinetic method appears to be equal to the reaction rate of the overall reaction. Coincidence of these two values implies that the Cu^{2+}-O-NO complex is a true intermediate in the SCR process and takes part in the rate-determining stage. Isolated Cu^{2+} ions (Cu_{isol}^{2+}) in the catalysts are the centers where one of the first stages of the reaction (NO activation) proceeds. The next stages occur possibly over other surface states of the copper. Thus, the Cu_{isol}^{2+} ion is a necessary part of the complex active center of the reaction. On the adsorption of NO on Cu-ZSM-5 zeolite, Ganemi et al. (219) observed IR bands at 1631, 1589, 1575, and 2130 cm^{-1} that are due to nitrate groups bridged to Cu^{2+}-O-Cu^{2+} dimers, monodentate nitrate species bonded to isolated copper ions, and NO^+ ions on the zeolite framework. They postulated N_2O_3 species bound to dimmers as the reactive intermediates, which are not detectable spectroscopically because of their short lifetime.

Konduru and Chuang (220) combined different transient species techniques to study the dynamic behavior of adsorbates, reactants, and product profiles in the decomposition of NO on over- and underexchanged Cu-ZSM-5 zeolites. NO decomposition over over-exchanged Cu-ZSM-5 zeolite allows a rapid equilibrium between gaseous NO and

$Cu^+(NO)/Cu^{2+}(NO_3^-)$. The fact that N_2 formation is accompanied by the presence of $Cu^+(NO)$ suggests that Cu^+ initiates the NO decomposition process. Thus, due to the presence of more surface Cu^+ sites, the overexchanged Cu-ZSM-5 shows higher NO decomposition activity at lower temperatures than the underexchanged sample. There exist two pathways for O_2 formation during the NO decomposition: oxygen produced from the decomposition of Cu^{2+} (NO_3) and oxygen from the desorption of adsorbed oxygen on Cu-ZSM-5.

Recently, overexchanged Fe-ZSM-5 materials have received much attention (221–224) because they are not poisoned by water or sulfur dioxide. Significant features of the catalytic reaction mechanism were elucidated by IR studies (223,225–228). Bell and coworkers (225) studied the interaction of NO, O_2, and NO_2 with Fe-ZSM-5, as well as the reduction of NO by C_3H_8 in the presence of O_2 by *in situ* IR spectroscopy. Figure 24A and B, respectively, show the IR spectra acquired during the temperature-programmed reactions of NO + O_2 and NO + C_3H_8 + O_2. IR bands at 1620 and 1577 cm^{-1}, due to NO_2 and NO_3 species, respectively, persist up to 673 K without the addition of C_3H_8 (Fig. 24A), but they disappear by 523 K in the presence of C_3H_8 (Fig. 24B). This indicates that C_3H_8 reacts with adsorbed NO_2/NO_3 species at temperatures above 423 K. But the band at 1876 cm^{-1}, due to adsorbed NO species, behaves similarly under these two different conditions. The authors proposed that the adsorbed NO_2/NO_3 species are active intermediates but adsorbed NO is not. NO_2/NO_3 species are formed via the reaction of NO with adsorbed O_2 and by the adsorption of NO_2 formed in the gas phase via homogeneous reaction of NO with O_2. The reaction of gas phase C_3H_8 with adsorbed NO_2/NO_3 species results in the formation of nitrogen-containing deposits that are oxidized to form N_2 and CO_2.

Sun et al. (227), using isotopic labeling and IR spectroscopy, investigated the reduction of NO with ammonia on Fe/MFI catalysts. Results show that a preferred path for the reduction of NO_x with ammonia is via ammonium nitrite, NH_4NO_2, which decomposes to N_2CH_2O. In this mechanism one N atom of the N_2 products stems from NO, the other from NH_3, and the consumption ratio of NO and NH_3 is 1:1. Heinrich et al. (228) performed a first DRIFT spectroscopy investigation of Fe-ZSM-5 catalyst with concomitant measurement of activities during the selective catalytic reduction of NO by isobutane. It was demonstrated that catalytic data obtained in a microcatalytic flow reactor are in principle reproduced by employing the DRIFT spectroscopy cell as a flow reactor. Stable adsorbates, transient intermediates, and interactions of zeolite OH groups have been monitored between 873 and 523 K, with concomitant NO conversion measurement.

Studies of NO_x reduction over non-metal-containing zeolites are helpful in understanding the promoting effect of exchanged cations and may reveal the issues regarding zeolite structure that are essential for high SCR activity in zeolite-based catalysts. The mechanism of the SCR of NO with NH_3 on H-ZSM-5 zeolites and H-mordenite has been investigated by Eng et al. (229). IR results show the appearance of an NO_2-type intermediate in SCR on both H-ZSM-5 and H-mordenite. It is proposed that the mechanism involves NO_2 interaction with pairs of adsorbed NH_3 resulting in the formation of an active complex that then reacts with NO to form N_2. An IR study of the reaction between NO_2 and propene over H-MOR (230) shows that nitrosonium ions, NO^+, formed upon reaction of NO_2 with NO over acidic zeolites, are likely to be important intermediates of NO_x reduction over this type of catalyst. They react rapidly with propene, thereby forming acrylonitrile. Hydrolysis of acrylonitrile yields adsorbed ammonium ions, which can reduce NO_x to N_2 efficiently. A reaction mechanism is suggested with 3-nitrosopropene and propenal oxime as intermediates.

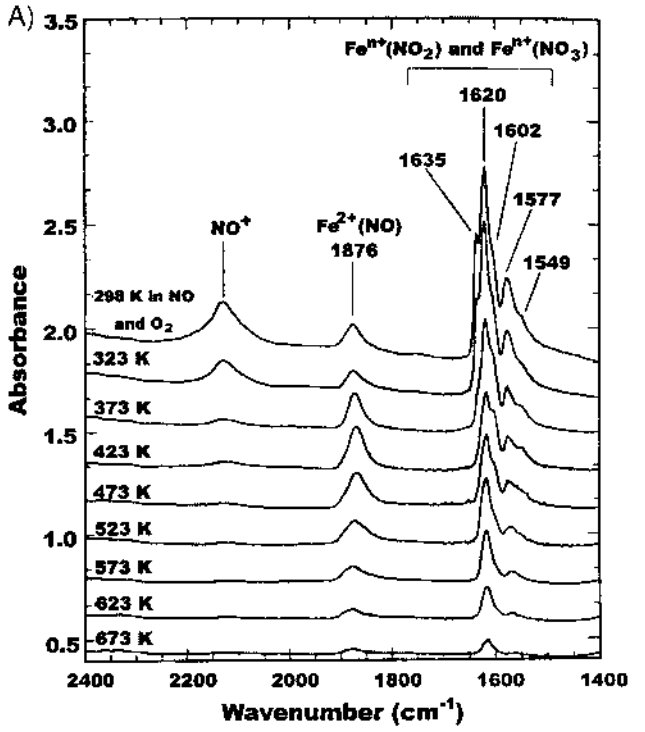

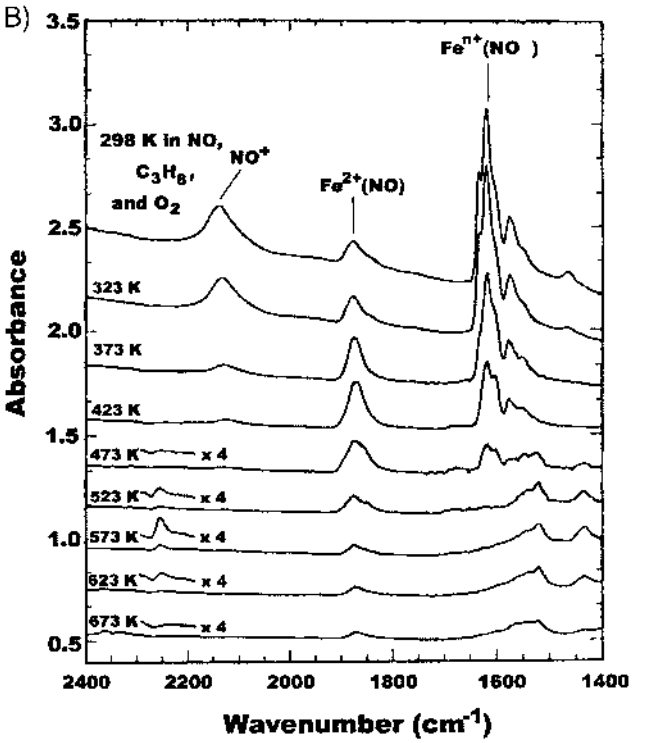

b. Decomposition of Chlorofluorocarbons

In the 1990s, zeolites have been used as catalysts for the oxidative decomposition of chlorofluorocarbons (CFCs) (231). Hannus et al. (232) carried out spectroscopic investigations of the decomposition of CCl_2F_2 (CFC-12) on three different types of zeolites (HY-FAU, HM-MOR, and H-ZSM-5). It is shown that CFC-12 decomposes over zeolites both with and without the presence of oxygen. While reactions take place in the cavities of zeolites and within the zeolite framework, surface reaction intermediates are formed. At the first stage of transformation, phosgene-like surface intermediate bound to the acidic OH groups of zeolite is generated. The desorption and decomposition of CFC-12 results in the formation of gaseous phosgene, hydrogen chloride, and carbon dioxide. At the same time, it was found that aluminum removal from zeolite framework takes place upon the decomposition and reactions. It is suggested that the decomposition of CFC-12 over zeolites is a simple reaction resulting in the collapse of the crystal structure of the zeolites, which explains the possible reason for catalyst deactivation.

4. Intermediates Formed in Zeolites

a. Intermediates in Hydrocarbon Conversion

In zeolite-catalyzed reactions of hydrocarbons conversion, carbenium and carbanion ions are generally considered as the reaction intermediates over acidic and basic zeolite catalysts, respectively. Here we summarize recent progresses in detecting these intermediates using IR and UV-vis spectroscopies.

Many efforts have been made to identify and characterize the intermediates involved in the transformation of hydrocarbons catalyzed by Brønsted acid sites (BAS) of zeolites (181,183,233–243). Carbenium ions, which were well characterized in superacids (240), have been considered to play important roles in hydrocarbon transformations. However, due to high reactivity and transient existence, simple alkyl carbenium ions on zeolites usually fail to be detected by various techniques, such as NMR, UV Raman spectroscopy, and IR, whereas oligomers (183,206,236) or alkoxy species (211,234,235,238) are relatively easily observed. Recently, formation of alkenyl carbenium ions on zeolites was reported by NMR studies (241–244) because alkenyl carbenium ions are more stable, since the positive charge is delocalized over adjacent C═C bond.

Very recently, to get additional information on the formation and transformation of alkenyl cations, Yang et al. (245–249), using in situ FTIR and UV-vis spectroscopies, investigated the adsorption of cyclic olefins on various zeolites at 150–573 K. Upon the adsorption of cyclopentene (CPE), 1-methylcyclopentene (MCPE), methylenecyclopentane (MECP), cyclohexene (CHE), and 1,3-cyclohexadiene (diene) on faujasite (Y), ZSM-5, mordenite, and beta zeolites, the formation of alkenyl carbenium ions, characterized by an IR band at about 1490–1530 cm^{-1}, was observed over a wide temperature range. UV-vis absorption results also confirm the formation of alkenyl carbenium ions (249). As an example, Fig. 25 show the IR results on the adsorption of MCPE on DY (246). The olefinic

Fig. 24 (A) IR spectra taken during a temperature ramp while 5000 ppm NO and 1% O_2 is passed over the catalyst after it had been exposed to this mixture for 20 min at room temperature. (B) IR spectra taken during a temperature ramp while a gas stream containing 5000 ppm NO, 5000 ppm C_3H_8, and 1% O_2 is passed over the catalyst after it had been exposed to this mixture for 20 min at room temperature. (From Ref. 225.)

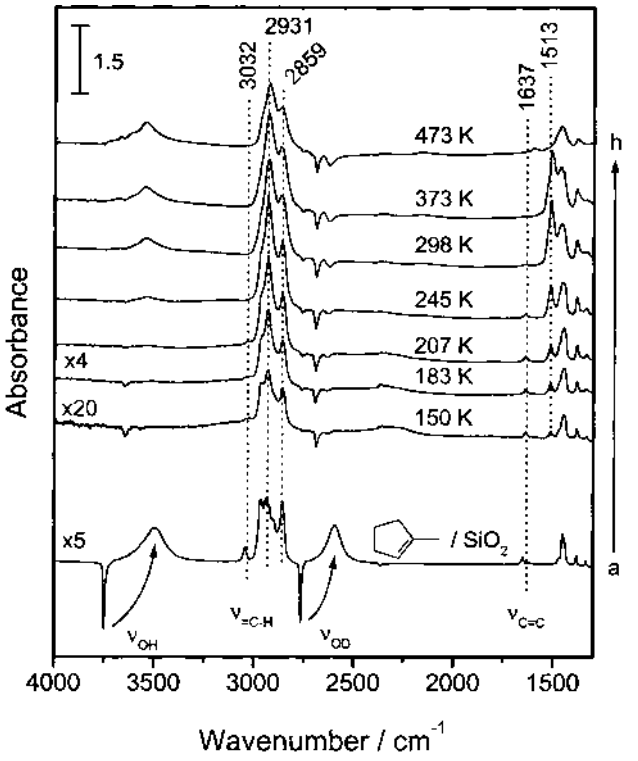

Fig. 25 IR spectra of 1-methylcyclopentene adsorbed on DY at various temperatures: (b) 150 K; (c) 183 K; (d) 207 K; (e) 245 K; (f) 298 K; (g) 373 K; and (h) 473 K. The spectrum of 1-methylcyclopentene adsorbed on SiO_2 at 215 K (a) is given as reference. The reverse peaks indicate the consumption of the OH and OD groups (From Ref. 246).

C-H stretching band at 3032 cm^{-1} and the $\nu_{C=C}$ band at 1637 cm^{-1} (23 cm^{-1} lower than that of 1-methylcyclopentene free molecules) can still be observed at 150 K, suggesting the presence of molecularly adsorbed species, i.e., π-OH complex. In the low-frequency region (1600–1300 cm^{-1}), a new band at 1513 cm^{-1}, which can be attributed to the formation of alkenyl carbenium ions, appears soon after introducing the adsorbate at 150 K.

With increasing temperature, the bands at 2931, 2859, and 1513 cm^{-1} grow in intensity, and the band at 3032 cm^{-1} due to olefinic C-H stretching almost disappears at 245 K due to desorption and/or reaction of the molecularly adsorbed species at higher temperatures. Upon heating to 373 K, the 1513 cm^{-1} band reaches maximal intensity and disappears with further increase in temperature. UV-vis spectra of MCPE adsorbed on DY show that three bands at 323, 400, and 480 (shoulder) nm appeared after the sample was exposed to MCPE at liquid nitrogen temperature and then warmed to room temperature, attributed to p–p* transitions of mono-, di-, and trienylic carbenium ions, respectively. The intensities of the three bands clearly show that monoenylic carbenium ions are predominant on the surface, along with a considerable amount of dienylic ones and a small amount of trienylic ones.

After an evacuation at 453 K, only dienylic and trienylic carbenium ions were left. This is in good agreement with IR results, which show that the band at 1513 cm^{-1}

disappears at 423 K and above. The authors also proposed the possible pathways for the formation of alkenyl carbenium ions from 1-methylcyclopentene, in which alkyl carbenium ions are proposed to play an important role in the formation of alkenyl carbenium ions. Monoenylic carbenium ions are formed through hydrogen transfer between alkyl carbenium ions and 1-methylcyclopentene and its oligomers. Then they lose more hydrogen atoms to form di- and trienylic carbenium ions. The formed carbenium ions are stabilized in the cyclic structure and are very stable.

By a comprehensive study of the adsorption of cyclic olefins on different zeolites, the authors (249) were able to draw following conclusions: (a) The ability to generate alkenyl carbenium ions ordered in the following sequence: diene $\geq$MCPE = MECP > CPE $\approx$ CHE. For 1-methylcyclopentene, methylenecyclopentane and 1,3-cyclohexadiene adsorbed on zeolite Y, the IR band at 1490–1530 cm^{-1} develops at temperatures as low as 150 K. The band increases in intensity with the elevation of temperature, and can be stable up to 373 K (b) Although alkenyl carbenium ions were formed on all of the acidic samples upon adsorption of cyclic olefins, different species may coexist on HZSM-5 and H-beta zeolites, which have smaller pores and stronger acidity than those of faujasite Y. Also, the small pores of zeolites like ZSM-5 can confine the access of cyclic molecules to acidic OH groups at low temperatures.

b. Intermediates in NO_x Decomposition

The reactive surface species that are formed during the decomposition of NO and the SCR of NO_x on zeolites exchanged with different metals are shown in Table 11. This table also gives the corresponding characteristic IR band(s) of these surface species.

G. Host–Guest Chemistry

Zeolites and zeolite-related microporous solids are ideal inorganic hosts for a large variety of guest species. Zeolite-based host–guest nanocomposites are a type of advanced material in which zeolites act as host for encapsulating and organizing molecules, crystalline nanophase, and supramolecular entities inside the zeolite pores. Space confinement and host–guest interaction results in composite materials possessing novel optical, electronic, and magnetic properties. Host–guest chemistry and catalysis in zeolites have been previously reviewed (262). IR (5,263) and Raman (59,264) spectroscopic studies of the host–guest interaction in zeolites have also been reviewed recently. Here, only spectroscopic characterization on the following topics is presented: (a) cluster in cavity; (b) assembling semiconductor; and (c) immobilization of homogeneous catalysts.

1. Cluster in Cavity

Crystalline zeolites and mesoporous supports have been widely used as stabilizing matrix for the preparation of highly dispersed metal particles because their microporosity/mesoporosity and molecular sieving behavior can provide selectivity in a variety of reactions.

a. Platinum-Based Clusters

Serykh et al. (265) investigated the electronic properties of Pt clusters in contact with the NaX zeolite matrix using DRIFT spectroscopy of chemisorbed H_2 and CO. The Pt clusters were prepared by the decomposition of negatively charged Pt carbonyl Chini complexes $[Pt_3(CO)_6]_n^{2-}$. According to the DRIFT and UV-vis spectroscopic data, the

Table 11 Intermediates in NO*x* Decomposition and Reduction

Reaction, catalyst	Intermediates	Characteristic IR band (cm^{-1})	Ref.
NO + propane + O_2 on Cu/ZSM-5	Cu^{2+}-O-NO	1630	218
	NO_2, NO_3^-(monodentate), NO_3^- (bidentate)	1628, 1594, 1572	250
NO on Cu-ZSM-5	N_2O_3ads	—	219
	$Cu^+(NO)_2$, $Cu^{2+}(NO)$, $Cu^{2+}O^-$ (NO), NO^+ads, $Cu^{2+}(NO_3^-)$	1816, 1910, 1895, 2123, 1624	220
	NO_2-containing species	1535–1630	251
	ON-Cu_2^+-NO_2^-	1630–1600	252,253
	$Cu^+(NO)_2$	1824, 1733	254
	Cu^+NO	1811	255
	$NO^{\delta-}$, $(NO)_2^{\delta-}$	1813, 1827, 1734	256
	NO_2^+-hydroxyl	2133	257
NO + O_2 on Cu-ZSM-5	Nitrate species	1630, 1613, 1577	258
NO + propene + O_2 On Cu-ZSM-5	Organic NO_2	1570	260
NO + O_2 On H-ZSM-5	NO^+-$O_{lattice}$	2133	259
NO + propane + O_2 on Fe-ZSM-5	NO_2ads, NO_3ads	1620, 1577	225
NO + NH_3 + O_2 on Fe/MFI	NH_4NO_2	—	226
NO + isobutane + O_2 on Fe-ZSM-5	Fe(NO)	1880	228
NO + NH_3 + O_2 on H-ZSM-5 and H-Mordenite	NO_2-type	1632	229
NO_2 + propene + O_2 on H-MOR	NO^+	2202	230
NO + CH_4 On Co-FER	Co(NO_2)	1630, 1600	261

decomposition of carbonyl complexes above 573 K in vacuum leads to the formation of small negatively charged metallic Pt clusters that can be reversibly carbonylated into the same initial Chini complexes. Adsorption of CO reveals that during evacuation of preadsorbed CO at elevated temperatures linear Pt-CO complexes are transformed into a new type of Pt-CO species with extremely low frequency of CO stretching vibrations at 1958–1976 cm^{-1} and a stronger metal–carbon bond. This transformation is explained by the redistribution of the negative charge between desorbing bridged CO molecules and metallic platinum particles. Similar low frequencies of linearly adsorbed CO were also reported for metallic Pt dispersed on basic carriers, i.e., alkaline-earth forms of zeolites (266–269) and hydrotalcites (270). The strong decrease of the frequencies in those cases was also explained by negative charging of the supported Pt particles due to electron transfer from basic oxygen anions to the metal.

Platinum-based bimetallic catalysts are of considerable importance for the petrochemical industry (271). Tkachenko et al. (272) studied the surface state of Pt particles in Pt/ZSM-5 and Pt-Cr/ZSM-5 catalysts by FTIR spectroscopy using CO as a probe molecule. Adsorbed CO on Pt/H-ZSM-5 catalysts gives a high-frequency band at 2089 cm^{-1} related to CO adsorption at electron-deficient Pt clusters inside the highly acidic zeolite matrix. This band shifts to 2120 cm^{-1} when CO is adsorbed on Pt-Cr/H-ZSM-5 catalysts and is assigned to the adsorption of CO on Pt-Cr alloy particles. This indicates the additional electron deficiency of surface Pt atoms in an alloy in the zeolites. Rades et al. (269) gave the evidence of the formation of Pt-Pd alloy on NaY zeolite by diffuse reflectance IR spectroscopy. The spectroscopic study shows that both monometallic Pt/NaY and Pd/NaY catalysts adsorb CO in linear and bridging forms. The stable form is linear for Pt and bridging for Pd, as usually observed. Pt/NaY contains a negatively charged Pt species in addition to the neutral one. Since the spectrum of the bimetallic catalyst is not the arithmetical superposition of Pt and Pd, it is concluded that the formation of a highly dispersed Pt-Pd alloy in or on the NaY zeolite.

b. Palladium

Sheu et al. (273) first save evidence of the formation of Pd carbonyl culsters by adsorption of CO on Pd/NaY catalyst. FTIR spectra, shown in Fig. 26A, which are indicative of Pd carbonyl clusters located inside supercages of NaY, are obtained after adsorption of CO

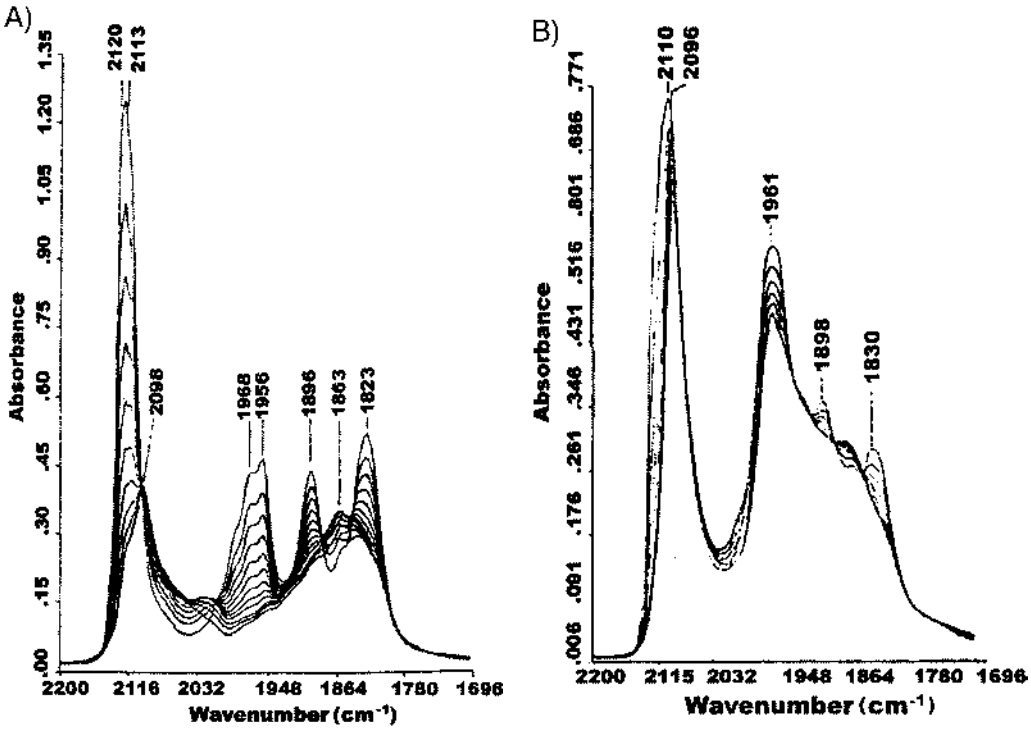

Fig. 26 (A) IR spectra of CO adsorbed on Pd_4NaY (500/200/20) after different purging times with Ar at 298 K. Purging time (min): 20, 25, 30, 35, 40, 45, 50, 55, 60, 70, 80, 100. (B) IR spectra of CO adsorbed on Pd_4NaY (500/500/60) after different purging times with Ar at 298 K. Purging time (min): 20, 25, 30, 35, 40, 45, 50, 60, 70, 80, 90. (From Ref. 273.)

on Pd/NaY reduced at 473 K. The spectra (Fig. 26B) of CO on the sample reduced at 773 K are characteristic of adsorbed CO on fairly large Pd particles that are presumably located at the external surface of NaY or voids. This is due to the migration of agglomerated Pd clusters. The geometry of the NaY supercages suggests that the core of the clusters could accommodate 13 Pd atoms; such clusters, including the bridging CO ligands, would fit perfectly inside these cages, while the terminal CO ligands would point outward through cage windows. The IR spectra change drastically upon purging with Ar at room temperature (see Fig. 26A), indicating the release of CO from the clusters. The easy release of CO is incompatible with thermal desorption, attributed to a reaction involving zeolite protons. Changes in the IR spectra of the zeolite O-H band support this proposal. The process is suggested schematically as:

$$\mathrm{Pdn(CO)_a} + \mathrm{H^+} \rightarrow [\mathrm{H - Pd}_n\mathrm{(CO)}_x]^+ + (\mathrm{a} - x)\mathrm{CO_{gas}}$$

Zhang et al. (274) made an IR study of the effect of Ca^{2+} and Mg^{2+} ions on the formation of electron-deficient $[Pd_nH]^+$ adducts in zeolite Y. The IR spectra of adsorbed CO on Pd particles in supercages of zeolite Y show that positively charged Pd_n clusters are formed when the concentration of protons in the supercages is high. This confirms that $[Pd_nH]^+$ adducts are the electron-deficient Pd clusters reponsible for catalytic superactivity. The fact that IR bands of adsorbed CO on PdMg-500 and PdCa-500 samples shift to higher frequencies than on PdNa-500 suggests that the formation of adducts is favored by a high concentration of divalent charge-compensating ions. The divalent ions preferentially populate sodalite cages and hexagonal prisms, thus preventing the migration of Pd^{2+} ions into these positions.

The electronic modification of supported Pd clusters in Pd/LTL by the addition of K into the zeolite was studied by Mojet et al. (275) using XPS and FTIR. The IR results show that both the bands of linear- and bridged-CO adsorption on Pd clusters shift to lower wavenumbers as the zeolite support varies from acidic to neutral to alkaline. The turnover frequency (TOF) of neopentane and propane hydrogenolysis increases with increasing support acidity from alkaline to acidic. The changes in spectroscopic and catalytic properties are proposed to be due to an electronic modification of the small Pd clusters caused by modification of the zeolite support.

c. Other Metal Clusters

Shen et al. investigated the intrazeolite anchoring of Ru carbonyl clusters (276) and Rh carbonyl clusters (277) by IR spectroscopy and other techniques. An in situ IR study (276) shows the formation of $[H_4Ru_4(CO)_{12}]$ guests in $Na_{56}Y$ zeolite by the reaction of $[Ru_3(CO)_{12}]$ with hydrogen, and the formation of $[Ru_6(CO)_{18}]^{2-}$ clusters in $Na_{56}X$ zeolite is confirmed by the thermal treatment of hexammineruthenium (III) complexes with a mixture of CO and H_2. The shifts of IR bands of CO stretching imply that the $[H_4Ru_4(CO)_{12}]$ or $[Ru_6(CO)_{18}]^{2-}$ should be encapsulsted in the α cages of the zeolites. The deposition of $[Rh(CO)_2Cl]_2$ vapor into the $Na_{56}Y$ cavities followed by a reductive carbonylation under a mixed CO and H_2O atmosphere produced $[Rh_6(CO)_{12}(\mu_3{-}CO)_4]$ clusters as evidenced by IR investigation (277). The decarbonylated species of the intrazeolitic $[Rh_6(CO)_{12}(\mu_3{-}CO)_4]$ is proposed to contain an Rh_4 cluster, which reacts with CO at low temperatures, generating $[Rh_4(CO)_9(\mu_3{-}(CO)_3]$ clusters, and with CO and H_2O at high temperatures to form$[Rh_6(CO)_{12}(\mu_3{-}(CO)_4]$ clusters. NMR and IR spectroscopy provided a direct picture of an interaction between clusters and the site II Na^+cations in supercages through involvement of the oxygen end of the face-bridging

carbonyl ligands. There are also many IR studies on other metal carbonyls or nitrosyls in zeolites, i.e., Cu (278), Co (279), W (280), Ir (281), and Au (282).

2. Assembly of Semiconductor

The assembly of semiconductor nanoclusters in the pores of zeolite molecular sieves has been actively explored as a means of producing tunable light-emitting materials (283,284). Zeolite molecular sieves and mesoporous materials offer a range of accessible pore sizes and channel morphologies that may allow an effective packaging of the guests to form structures resembling semiconductor.

a. CdS-Y

Telbiz et al. (285) monitored the preparation of CdY and the sulfidation of CdY by IR spectroscopy. Changes of IR bands in the framework vibrational region (400–650 cm^{-1}) and hydroxyl region clearly indicate the interaction between Cd cation and the zeolite lattice. During the interaction of H_2S with CdY, some changes of the vibrations of the zeolite framework are observed and can be explained in terms of framework charge delocalization caused by the CdS formation.

b. Selenium in Zeolites

Selenium has been loaded into a variety of molecular sieves like mordenite, faujasites (X, Y), zeolite A, and $AlPO_4$-5 in order to study the influence of spatial confinement on its structure using Raman spectroscopy (286–291) and other techniques. The structural analysis shows basically one-dimensional Se chains occupying the voids in the molecular sieves. Only for zeolite A do the experimental results support the formation of isolated clusters like Se_8 rings (287). The recent Raman spectroscopic study on selenium incorporated in Nd-Y zeolite presents new aspects of the photochemistry of selenium (290). The formation of Se_2^- radical anion in the zeolite host was established from its resonance Raman spectrum, consisting of 10 almost equidistant bands between 328 and 3220 cm^{-1} with the excitation laser at 476.24 nm. A broad band at 260 cm^{-1} due to amorphous selenium and selenium chain structures encapsulated in zeolite is continously deleted under illumination with the laser radiation. Simultaneously, the intensities of the characteristic bands due to Se_2^- increase gradually. These indicate a photoinduced decomposition of the Se chains with accompanying formation of Se_2^- fragments. There are also reports on ZnS-MCM-41 (292), BN-ZSM-5 (293), and Si cluster/NaHY (294) studied by FTIR, UV-vis, thermogrammetric analysis–mass spectrometry, and NMR spectroscopies.

3. Immobilization of Homogeneous Catalysts

a. Chiral Salen Manganese(III)-A-MCM-41

The embedding of a enantioselective homogeneous catalyst—the chiral manganese(III) cationic complex of salen type (Jacobsen complex I)—into the pores of mesoporous was investigated by different methods including TG-DTA (differential thermal analysis), UV-vis, and FTIR (295). The comparison of the IR vibrational spectra of the free and the molecular sieve–loaded Jacobsen complex is shown in Fig. 27A. The appearance of the spectrum of the embedded complex is very similar to that of the free complex, indicating that the structure of the complex is maintained in the immobilized state. The frequency shifts and relative intensity changes of the IR bands can be interpreted by the changes of the electronic structure of the complex caused by guest–host interaction. The interaction of

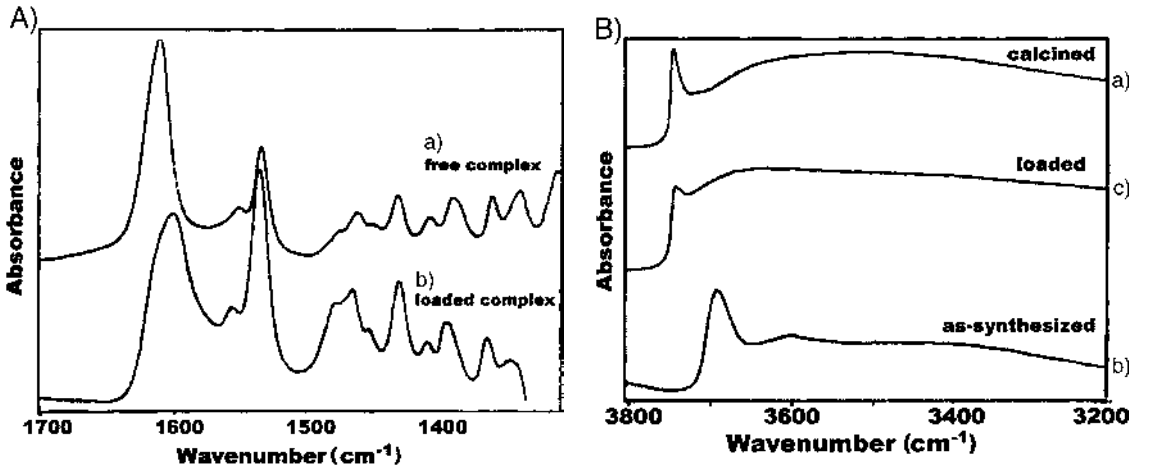

Fig. 27 (A) IR spectra of the Jacobsen complex I: (a) free (KBr pellet); and (b) loaded in A1-MS (self-supported pellet). (B) IR spectra in the range of hydroxyl stretching vibration mode of (a) calcined A1-MS sample; (b) as-synthesized A1-MS sample; (c) A1-MS sample loaded with Jacobsen complex I (in situ studies). (From Ref. 295.)

the complex with interior silanol groups is manifested in the OH vibrational spectra (Fig. 27B). After the complex embedding, the intensity of the band at 3740 cm^{-1} decreases remarkably. For comparison, the template cetyltrimethylammonium, present in the as-synthesized material, causes only a shift of this band to lower wavenumbers (3690 cm^{-1}). This shows conclusively that the Jacobsen complex interacts with the walls more strongly than the template. Catalytic tests in olefin epoxidation prove that catalytic activity and stereoselectivity of the complex after the embedding are preserved.

b. (salen)Mn-Y

Sabater et al. (296) accomplished for the first time the preparation of a chiral salen manganese complex analogous to the Jacobsen catalyst into the supercages of large-pore Y zeolite. The resulting salen Mn complex entrapped within Y zeolite exhibits similar catalytic activity as the same complex under homogeneous conditions. Characterization of this catalyst is made by TG-DSC, FTIR, and diffuse reflectance. The IR spectrum of the zeolite guest after the synthesis is compared with those recorded for authentic samples of the salen ligand and salen $Mn^{III}Cl$. The spectrum of the salen Mn^{III}-Y sample coincides with that of the chloride half of the same complex, thus establishing the purity and identification of the salen Mn^{III}-Y zeolite. The most characteristic band associated with the salen ligand appearing at 1500 cm^{-1} is absent for the zeolite sample, indicating that the amount of uncomplexed ligand is below the detection limit of IR spectroscopy.

c. [Mn(salen)Cl] in EMT

Ogunwumi and Bein (297) assembled and trapped the asymmetrical manganese salen catalysts in the cages of zeolite EMT through a multistep synthesis. The encapsulated Mn salen complexes were identified by UV-vis and IR spectroscopy. These heterogeneous catalysts produce high enantiomeric excess in the epoxidation of aromatic alkenes with NaOCl as the oxidant.

d. Co(salen)-MCM-41

New chiral (salen) complexes immobilized on MCM-41 were synthesized by multigrafting (298). The immoblized optically active Co(II) salen complexes show a very high enantioselectivity in the asymmetrical borohydride reduction of aromatic ketones. Both the homogeneous salen complex and the heterogenized one show an IR band at 1640 cm^{-1} attributed to C═N stretching and this band is not found in the IR spectrum of pure MCM-41. Thus the author suggested that the salen complexes are trapped into MCM-41 since the band at 1640 cm^{-1} is a characteristic band of the salen complex.

IV. RAMAN SPECTROSCOPIC STUDIES OF MICROPOROUS MATERIALS

A. Introduction

In the development of zeolite science, IR has been the major vibrational spectroscopy for structure and reactivity characterization. Like IR, Raman spectroscopy can also provide important information on the structure of zeolites and similar porous materials. Raman spectroscopy has been widely applied in the characterization of molecular sieve science during last decades (59,299). However, high-quality Raman spectra are difficult to obtain because of the low sensitivity and strong fluorescence interferences. These problems have been partly overcome since the invention of FT Raman spectroscopy; in particular, the recent progress of UV Raman spectroscopy makes it possible to completely avoid the fluorescence problem. Consequently, an extremely rapid growth of Raman studies of zeolites and molecular sieves has been achieved and is expected to occur in the future.

As summarized by Mestl and Knözinger (300), the vibrational modes of zeolites can be described as the sum of three main contributions from the framework of zeolites, the charge-balancing cations in the framework, and the hydroxyl groups with charge-compensating protons. The first two components can be conveniently determined by Raman spectroscopy, while the last one is usually studied by IR in most cases. At the beginning of development of Raman spectroscopy in the area of zeolite study, researchers focused their attention on framework vibrations in various zeolites with regular microporous structures. Based on a thorough understanding of the relationship between vibrational spectra and the framework structures, additional information on the synthesis of zeolites, the effects of nonframework species, and host–guest interactions on the framework vibration appeared in the literature.

B. Framework Vibrations

The vibrational frequencies of zeolite lattice, which result from stretching and bending modes of the T-O (T = Si or Al) units, are observed in the range between 200 and 1500 cm^{-1} (47,301), where three frequency regimes dominate, namely, 1000–1200 cm^{-1}, 700–850 cm^{-1}, and 250–500 cm^{-1}, corresponding to localized and delocalized antisymmetrical stretching vibrations, localized and delocalized symmetrical stretching vibrations, and bending vibrations, respectively (58,302). Based on similar taxonomies, the lattice modes can also be divided into structure-sensitive and structure-insensitive vibrations as displayed in Table 12 (303). The position of the strong vibration around 500 cm^{-1}, resulting from mixed stretching and bending modes, strongly depends on the T-O-T angles and, therefore, can be used to characterize the aluminum content of the lattice. A more detailed classification of framework vibrations was recently described (19).

Table 12 Structure-Sensitive and Insensitive Lattice Vibrations of Zeolites

Structure-insensitive vibrations	Wavenumber (cm^{-1})
Asymmetrical stretching vibrations	1200–1000
Symmetrical stretching vibrations	850–700
Bending vibrations	600–400
Structure-sensitive vibrations	**Wavenumber (cm^{-1})**
Asymmetrical stretching vibrations	1050–1150
Symmetrical stretching vibrations	750–820
Double-ring vibrations	500–650
Pore opening vibrations	300–420

1. Structure-Sensitive Bands Between 300 and 600 cm^{-1}

The strongest and most structure-sensitive bands in the Raman spectrum of zeolites are generally between 300 and 600 cm^{-1} and have been assigned to the motion of an oxygen atom in a plane, perpendicular to the T-O-T bond, representing the most characteristic vibrational information of framework structures (304–306). They have been well studied since the early application of Raman spectroscopy in the characterization of framework of zeolites, including 16 natural and synthetic zeolites (307). For example, the spectrum of mordenite has a band at 395 cm^{-1}, while it is at 480 and 520 cm^{-1} for faujasite and chabazite (306), respectively. Extension to many other topologies later allowed derivation of a correlation between the frequency of this Raman band and the ring size, the average T-O-T angle, and the Si/Al ratio in the framework of zeolites (305).

a. Ring Size

In general, smaller rings correspond to higher frequencies. The precise band shifts depend on the type of rings present. Zeolites built of four-membered rings as the smallest building block exhibit the Raman band around 480–520 cm^{-1} (304). Zeolites containing even-numbered rings (4, 6, 8, 10, or 12 MR) have the band around 500 cm^{-1}. The presence of 5-membered rings leads to a shift of this frequency to 390–460 cm^{-1}. For example, ferrierite has a band at 430 cm^{-1} for its 5-, 6-, 8-, and 10-membered rings. The absence of an 8 MR results in a band shift to 450 cm^{-1}, as in ZSM-23 and NU-10 with TON topologies. MFI and MOR aluminosilicates contain 4, 5, 6, 8, 10, or 12 MR, and have Raman frequencies of 390 and 460 cm^{-1} (305). The T-O-T bending motion frequencies of several common zeolites are exhibited in Table 13 with their corresponding number of ring members (42).

b. T-O-T Angle

Determined by the sizes of rings in zeolites frameworks, the frequency of Raman band corresponding to the bending motion of the oxygen atom also depends on the value of the average T-O-T angle, defined as the arithmetic mean of the four T-O-T angles around a T atom. A higher T-O-T angle results in a decreased bending force constant; thus, a lower $\nu_{S(TOT)}$ frequency is given. Dutta et al. studied the correlation between this Raman band and T-O-T angles in the structure of zeolites (304). Their results can be summarized in Table 14 and Fig. 28.

Table 13 Observed Frequencies and Assignments in the UV Raman Spectra of Zeolites

	Band position (cm^{-1})					
	T-O-T bending motion				T-O-T symmetrical	T-O-T asymmetrical
Samples	8MR	6MR	5MR	4MR	stretching vibration	stretching vibration
NaX		290, 380		508		995, 1075
NaY		305, 350		500		975, 1055, 1125
NaA	280	338, 410		488	700	977, 1040, 1100
L	225	314		498	800	986, 1098, 1125
ZSM-5		294	378	440, 470	820	975, 1028, 1086
MOR	240		405	470, 482	812	1145, 1165
Beta		336	396	428, 468		1064, 1120

Source: Data from Ref. 42 and references cited therein.

c. Si/Al Ratios

The basic building of common zeolites is the tetrahedral units sodalite cage, consisting of alternating corner-shared SiO_4 and AlO_4, which may be arranged to give many different structures (19). In fact, one of the most immediate reasons for the difference of the number of ring members and the T-O-T angle is the incorporation of Al atoms in most aluminosilicate zeolites. Therefore, the Si/Al ratio is an important factor that affects the Raman frequencies of zeolites as T-O-T angles and number of ring members.

The incorporation of aluminum atoms at a low level in the faujasitic zeolite framework broadens the Raman bands at 298, 312, 492, and 510 cm^{-1} for the purely siliceous zeolite. This broadening is attributed to the random distribution of Al^{3+} cations within the framework, which leads to the disorder interaction of the oxygen atoms in the T-O-T units with the charge-balancing cations and solvent molecules (308). The frequency of these vibrational modes depends mainly on the polarity and length of the Al···O···Si bonds, since Al and Si have similar masses (309). For the incorporation of aluminum atoms at high level, marked changes in band intensity as well as frequency shifts were observed for the most Raman-active bands. This effect is most prominent for the antisymmetrical stretching modes around 500 cm^{-1}. Such frequency shifts in the Raman spectra of zeolites

Table 14 Raman Frequencies and Structural Data

Material	Raman frequency (cm^{-1})	T-O-T angle (degrees)
Cs-D	521	136.1
Na-X	515	139.2
Na-Y	505	142.2
Li-A	497	141.2
Na-A	490	148.3
Na-P	487	147.6
K-R	486	146.8
Magadiite	472	151 (predicted)

Source: Data from Ref. 304 and references cited therein.

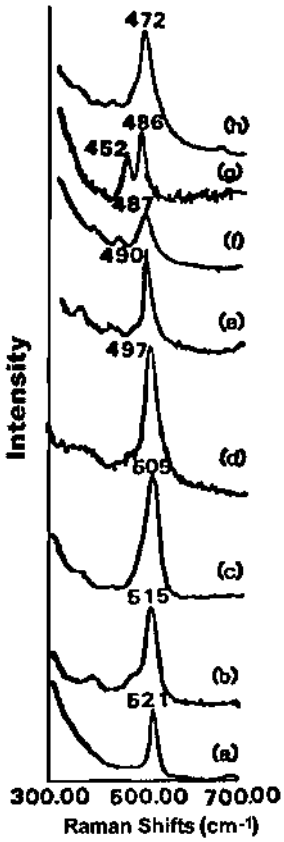

Fig. 28 Raman spectra of (a) Cs-D, (b) Na-X, (c) Na-Y, (d) Li-A, (e) Na-A, (f) Na-P, (g) K-R, and (h) synthetic magadiite; laser line, 457.9 nm; slit width, 6 cm^{-1}; power at the sample, 10–15 mW. (From Ref. 304.)

A, X, and Y were observed by Dutta and coworkers (308,310). For the zeolite A with LTA topology, the frequency increases with increasing Si/Al ratio (310), while for the FAU group including X, Y, and siliceous faujasite, the frequency tends to decrease (308). The different trends indicate the opposite changes of the T-O-T angle determined by Si/Al ratio between the two topologies of LTA and FAU. Another example is shown in Fig. 29, the strong, sharp bands at 488 and 510 cm^{-1} in the completely siliceous faujasite, corresponding to average Si-O-Si angles of 141° and 147°, are broadened and shift slightly to higher frequencies with the decreasing of the Si/Al ratio (308).

2. High-Frequency Bands in 850–1210 cm^{-1}

The Raman bands in the range of 850–1210 cm^{-1} are generally ascribed to the asymmetrical stretching vibration of the Si-O bond. In zeolite A, the different frequencies of the Si-O stretching are related to the three crystallographically different oxygen positions in the lattice (309,311). The vibrational coupling between the adjacent SiO_4 and AlO_4 tetrahedra in the NaA framework is expected to be small, and this allows consideration of the vibrations as being perturbed by those of the individual tetrahedra units. For a larger T-O-T angle and a shorter Si-O bond length, the coupling between adjacent SiO_4

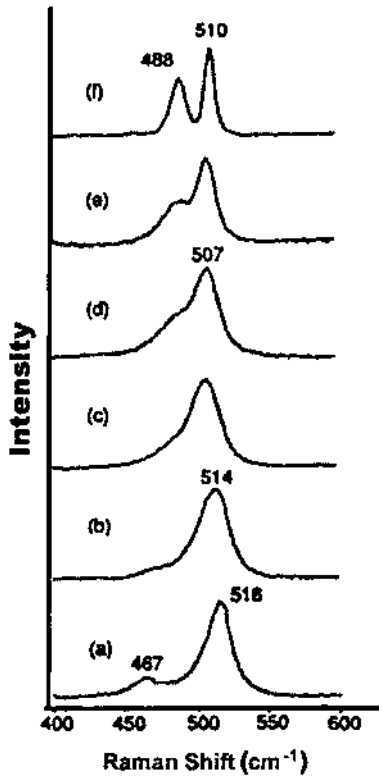

Fig. 29 Raman spectra of faujasitic zeolites as a function of Si/A1 ratio in the region between 400 and 600 cm^{-1}. The Si/A1 ratios of the framework are (a) 1, (b) 1.3, (c) 2.6, (d) 3.3, (e) 4.5, and (f) ∞. (From Ref. 308.)

and AlO_4 tetrahedra increases, giving an increase of the Si-O stretch frequency and a decrease of the Al-O frequency. The two bands at lower frequency then correspond to the vibrations involving the O_1 and O_3 atoms. These assignments were confirmed by studying the effect of gradual exchange with other monovalent cations. The site preferences for mixed cation populations have been studied well and could be related satisfactorily to the observed changes of the Raman stretching bands.

For faujasitic-type zeolites like X and Y with an Si/Al ratio of 1.0, the four bands in the 900–1250 cm^{-1} region are assigned to the Si-O stretching vibrations of Si attached to the four different oxygens of the framework (308). At intermediate Si/Al ratios, bands in the 900–1250 cm^{-1} region show an increase in frequency as the Si/Al ratio increases. In zeolites X (Si/Al = 1.2), there are few Si-O-Si bonds, and the Si-O stretch vibrations can again be treated as those of individual SiO_4 tetrahedra, with weak vibrational coupling to the adjacent AlO_4 units. In analogy with the assignment in zeolite A, four bands in the Raman spectrum of zeolite X (between 954 and 1066 cm^{-1}) can be associated with four different lattice O atoms, even if the differences are less marked than for A zeolites (308). An increase of the faujasite Si/Al ratio increases the number of adjacent SiO_4 tetrahedra. Consequently, the four distinct framework sites are no longer distinguishable in the spectrum, and merging of bands is observed. Concurrently, a large shift toward higher

frequencies results from the much stronger coupling between the adjacent SiO_4 tetrahedra. For fully siliceous faujasite, the Si-O stretching vibrations are eventually shifted up to 1186 and 1209 cm^{-1} (308).

3. Other Framework Vibrations

In most zeolites, framework bands between 600 and 850 cm^{-1} and at low frequency seem to be of little diagnostic value. The Raman bands of 703 and 738 cm^{-1} of zeolite A were assigned to asymmetrical Al-O stretching modes at first (309). In ZSM-5 spectra, symmetrical Si-O stretching bands are clearly observed between 800 and 900 cm^{-1} (312). Later the bands were considered to be T-O_1-T and O_3-T-O_3 bending modes in the presence of double rings instead (310). In the case of faujasitic zeolites, a group of three or four bands is observed in the region of 750–900 cm^{-1}, which is more sensitive to the ion-exchange ratio rather than the Si/Al ratio. These bands are related to the motion of Si atom in the tetrahedral cage (308).

In the frequency scale of 300–450 cm^{-1}, the spectrum of zeolite A has two Raman bands at 337 and 410 cm^{-1}. They are insensitive to either the Si/Al ratio or different cation exchange except Li^+. So they can be assigned to the twisting motion and the ring breathing mode of the double ring involving the motion of oxygen atoms (313).

There are also some Raman bands at lower frequency below 200 cm^{-1} that have been well studied by Brémard and coworkers (314). They are corresponding to some ν(T-O-T) vibrational modes and the translation of exchanging cations.

C. Heteroatoms Incorporation

Raman spectroscopy has become one of the most powerful tools to identify the framework heteroatoms owing to the developments of novel technologies like FT Raman and UV Raman spectroscopies. The most common isomorphously substituted heteroatoms are Al atoms in the framework of aluminosilicate zeolites. The moderate incorporation of Al atoms in the framework of silicon-rich zeolites with the MFI structure can be described as a solid solution of [AlO_4] in [SiO_4]. This implies that the general features of the vibrational spectra of silicalites should not be altered substantially by the substitution of Si by Al (58,315,316). It is almost the same when other elements, such as Ga, Ge, Be, Fe, and Ti, are isomorphously substituted for Si in silicalite, although frequency shifts can occur due to the changing polarities and length of T-O bond and because of the different masses of the heteroatoms.

Scarano and coworkers (315) have investigated the IR and Raman spectra of pure and Al-, B-, Ti-, and Fe-substituted silicalites in the Si-O stretching region (1500–700 cm^{-1}) systematically (Raman spectra are given in Fig. 30). Along with the characteristic stretching modes of the zeolite skeleton, silicalites containing hydroxylated nests show also broad bands at about 960 cm^{-1} (IR) and at about 976 cm^{-1} (Raman), associated with O_3Si-OH group modes, with prevailing Si-OH stretching character. The replacement of Si with transition metals (like Ti or Fe) causes the appearance of new IR- and Raman-active modes (a) at 960 cm^{-1} (IR and Raman) and at 1127 cm^{-1} (Raman) in Ti silicalite; (b) at 1015 cm^{-1} (IR) and at 1020 cm^{-1} (Raman) in Fe silicalite. Neither the Raman nor the IR spectra of the skeletal modes are substantially modified by the introduction of Al (ZSM5). The presence of boron induces the Raman bands at 1417 and 976 cm^{-1} in the Raman spectra. Their assignments are shown in Table 15 (315).

Prakash and Kevan studied Nb atoms in the framework of silicalite-1 using Raman spectroscopy (317). The Raman bands at 930 and 970 cm^{-1} that are absent in the spectrum

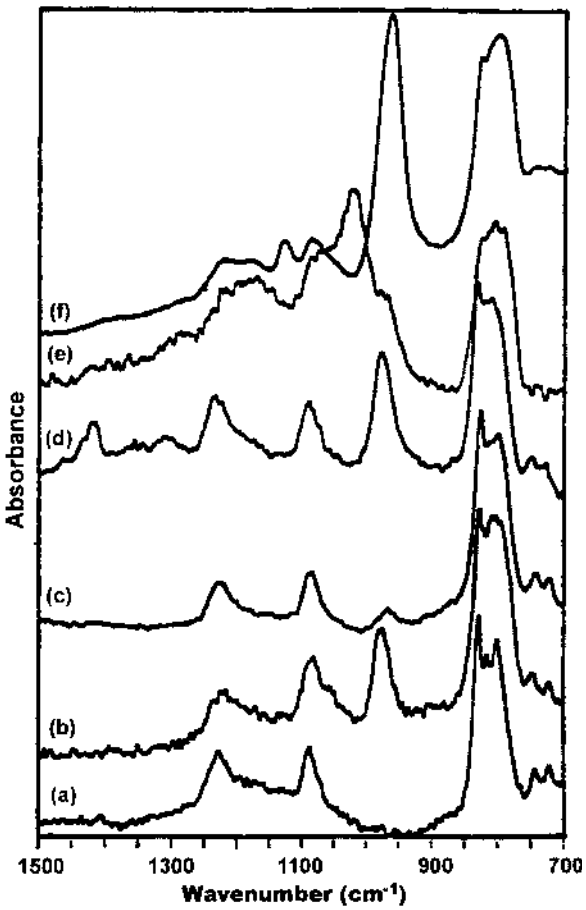

Fig. 30 Raman spectra of pure and substituted silicalites (pellets) outgassed at room temperature: (a) defect-free silicalite; (b) defective silicalite; (c) H-ZSM-5; (d) B silicalite; (e) Fe silicalite; (f) Ti silicalite. (From Ref. 315.)

of silicalite-1 appear and were assigned to the stretching modes of Nb-O-Si and can be regarded as an evidence of tetrahedral Nb atoms in the framework.

The effect of isomorphous substitution of the MFI framework with Ge atoms has also been investigated by Kosslick et al. (318). Besides the most intensive Raman bands of Si-O-Si or Si-O-Ge deformation vibrations at 350–400 cm^{-1}, the Raman band at 685 cm^{-1} was found to become stronger with increasing Ge content. Thus, it is due to the tetrahedrally coordinated Ge in the framework and was assigned to the corresponding symmetric Si-O-Ge stretching vibrations. With increasing Ge content, the T-O-T deformation band is shifted to higher wavenumbers, while the symmetrical Si-O-Si band is shifted to lower frequency by about 8 cm^{-1}, indicating a decrease in the T-O-T angle caused by the incorporation of Ge.

The assignment of the Raman band around 960 cm^{-1} for most isomorphously substituted zeolites has been in debate for a long time. It was once assigned to the localized $\equiv$Si-OH stretching mode of [O_3Si-OH] groups by Scarano et al. (315). Based on quantum mechanical calculations on cluster models, it was proposed by de Man and

Table 15 Raman Frequencies of Active Modes of Pure, Defective, and Substituted Silicalites

	Skeletal modes (cm^{-1})		Stretching modes involving O_3Si-OH (cm^{-1})			Stretching modes involving heteroatoms (cm^{-1})		
				After interaction			After interaction	
Sample	Asym.	Sym.	Before interaction	a	b	Before interaction	a	b
Silicalite	1227–1174 1084	824–796	—	—	—	—	—	—
Defective silicalite	1227–1174 1084	824–796	976	~982	~1050	—	-	-
H-ZSM-5	1230–1174 1084	824–796	~970			-	-	-
Ti-silicalite	1230–1176 ~1080	824–796	960	976	994	1127 960	Disappears 976	Disappears 994
Fe-silicalite	1230–1176 ~1080	824–796	976	Disappears	Disappears	1020 976	1032 Disappears	1036 Disappears
B-silicalite	1230–1180 1088	824–796	976	~982	~1050	1417	Disappears	Disappears

Source: Ref. 315.

Sauer (319) that the mode is a simple antisymmetrical stretching of the Si-O-Ti bridge. Camblor et al. (320) have concluded that the 960 cm^{-1} band is an Si-O vibration in defects. Deo et al. have attributed this band to the Si-O stretching vibration of a SiO_4 tetrahedron with one nonbridging oxygen atom (321). Very recently, it has been proposed, based on UV Raman study (23), that the 960 cm^{-1} band may be only a minor, secondary manifestation of the presence of heteroatoms in the framework. Detailed application of UV Raman to Ti, Fe, V, and B heteroatoms will be presented in Sec. V of this chapter.

D. Synthesis Mechanism of Zeolites

A detailed understanding at a molecular level of every step from the solution to solid state during zeolite synthesis is very important for optimal control of the synthesis process. Raman spectroscopy can detect amorphous zeolite units that do not yet have long-range order, which cannot be studied by XRD. Raman spectroscopy enables us to obtain vibrational spectra recorded from solution species as well as from solid phases presented during the zeolite synthesis since the minimal concentrations for detection of spontaneous Raman from liquids are typically 0.05–0.1 M (19,322) and the Raman cross-section of the $Al(OH)^-_4$ species is much stronger than silicate or aluminosilicate anions (323). There have been extensive Raman spectroscopic studies on the mechanisms of structural formation of zeolites in both solid and liquid phases (19,22,306, 322–324).

Usually the Raman study on the synthesis of zeolites includes two main parts. One is the framework vibration during the crystallization of zeolites, the other is the interaction between shape-directing templates and the solute silicate species that leads to the formation of the final framework topology. The Raman investigations of the synthesis of some often used zeolites are presented in the following sections.

1. Zeolite A

McNicol et al. studied the synthesis of zeolites A using Raman spectroscopy (325). They found no changes in the vibrational spectra of the liquid phase during crystallization but observed a change in the position of the Raman band of the tetramethylammonium cation present in the solid phase of the gel. They postulated that crystallization took place in the solid gel phase. Angell and Flank (326), on the other hand, found a change in the concentration of the aluminate species during crystallization of zeolites A and suggested a solution transport mechanism. Later on, Roozeboom and coworkers also reported Raman studies of the crystallization process of zeolites A, X, and Y (323).

A detailed investigation on the synthesis of zeolite A, including the formation of gels and their transformation to zeolite crystallite, was presented by Dutta et al. (306). Figure 31 clearly shows the evolution of Raman bands due to zeolite A at 336, 407, 491, 700, 733, 745, 970, 1040, and 1102 cm^{-1} as a function of crystallization time. The XRD amorphous gel has a structure consisting of predominantly four-membered rings of SiO_4 and AlO_4 tetrahedra connected in random fashion with the corresponding Raman band at 504 cm^{-1} in Fig. 31. During the gel-to-crystal transformation, the spectral changes include a decrease in intensity of the 450, 847, and 960 cm^{-1} bands and a shift in frequency of the 504 and 496 cm^{-1} bands. The shift of the 504 cm^{-1} band to lower frequencies suggests an alteration in the structure of the four-membered rings by interaction between gel and those $Al(OH)_4^-$ ions and forms nuclei of zeolite A during the nucleation period.

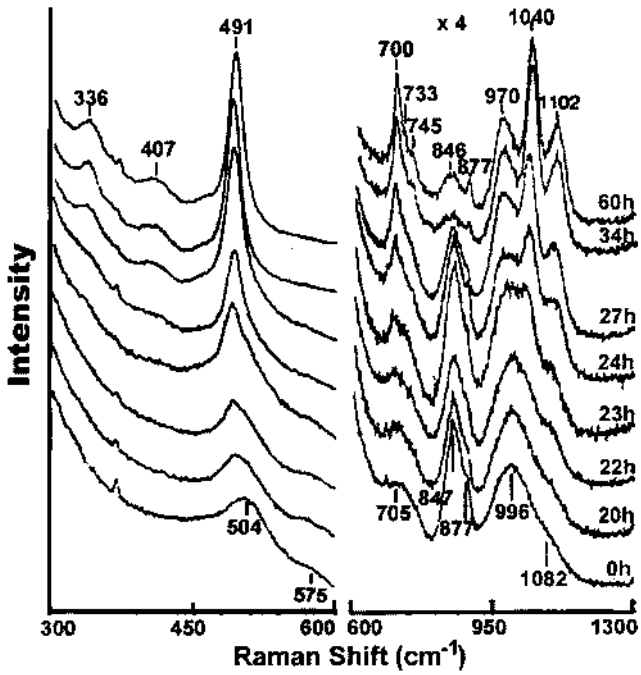

Fig. 31 Raman spectra of the solid phase during zeolite A synthesis at 50°C at various times (starting composition $8.6Na_2OlAl_2O_31SiO_2556H_2O$). (From Ref. 306.)

2. Zeolite X, Y

Faujasitic zeolites are denoted as zeolites X and Y and are distinguished by the Si/Al ratio of an identical framework. For frameworks of Si/Al ratio between 1.0 and 1.5, the zeolite is called zeolite X, and for values greater than 1.5, it is typically called zeolite Y (327). Roozeboom and coworkers studied the synthesis of zeolite X and Y together with zeolite A using Raman spectroscopy (323). In the Raman spectra of liquid phase, a Raman band at 620 cm^{-1} was observed in the initial stage of both zeolite X and Y synthesis, and this band is assigned to the Al-O symmetrical stretching mode of aluminate species in solution. Unlike the case of zeolite A, this band does not disappear after crystallization. Furthermore, some soluble species having Raman bands around 448, 600, 777, and 936 cm^{-1} for zeolite X, and 600, 777 cm^{-1} for zeolite Y, are also observed in the course of crystallization, indicating the depolymerization of polymerized silicate species into monomeric and dimeric silicate ions. In the Raman spectra of solid phase in zeolite X and Y synthesis, the arising peaks at 512, 376, and 291 cm^{-1} for zeolite X and 511, 369, and 298 cm^{-1} for zeolite Y indicate the gradual formation of zeolite frameworks.

Dutta and coworkers (22) reported the Raman spectra of the solution and solid phases during zeolite Y crystallization and have explored the effects of aging. The strong Raman band at 620 cm^{-1} is also observed at the beginning of crystallization. After aging for 6 h, a strong band at 780 cm^{-1} and weaker bands at 441 and 919 cm^{-1} appear, which are characteristic of monomeric silicate species ($SiO_2(OH)_2^{2-}$). Weaker bands at 601 and 1025 cm^{-1} due to dimeric silicate species appear in solutions at longer heat aging. All of these show a similar aluminate transport mechanism to the results of Roozeboom et al. (323). In the Raman spectra of solid phase in zeolite Y synthesis, the bands at 440 and 361 cm^{-1} are typical of six-membered aluminosilicate rings, which show striking similarity to the Raman spectra between the solid phase and nepheline glass containing the six-membered ring. Based on the correlation between ring-size and $\nu_{S(TOT)}$ frequency, this can be regarded as the evidence that six-membered rings are present in the amorphous aluminosilicate phase during zeolite nucleation. Figure 32 resembles the formation of nuclei of zeolite Y involving these rings as building blocks, which are connected via four-membered rings to form sodalite cages.

Although the final framework topology is identical for zeolite X and Y, different synthesis mechanisms are reported on two crystallization systems (22). For the zeolite X with Si/Al ratio less than 1.5, the crystallization process favors the formation of four-membered aluminosilicate rings as main intermediate species, while six-membered rings dominate in the case of zeolite Y.

Another Raman study found that the formation of faujasitic zeolites (X, Y) from two silica sources (Ludox and N-brand) was different (328). Their Raman results indicate that the gel preceding the formation of crystals is composed of a solid phase with disordered four-membered aluminosilicate rings and soluble monomeric and dimeric silicate species.

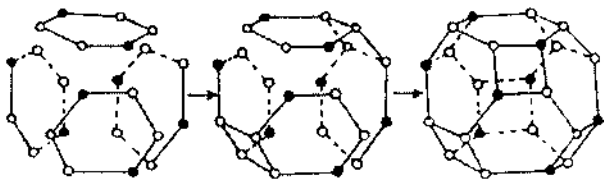

Fig. 32 Scheme for the formation of nuclei of zeolite Y. (From Ref. 22.)

The Ludox preparation has a more rapid crystallization rate than N-brand does, and zeolite X crystals are observed in the Raman spectrum at earlier times than by XRD, indicating more extensive nucleation in the early stage of the crystallization. Raman spectra recorded during synthesis of zeolite Y indicates that the structure of the solid phase in the initial stages of aging is different for the Ludox and N-brand preparations. At later stages, the spectra are dominated by soluble silicate species in both cases.

3. Mordenite

The formation of mordenite zeolites during crystallization was investigated by Dutta et al. using Raman spectroscopy (322). In the inorganic preparation, four-membered aluminosilicate rings are observed with the characteristic Raman band at 495 cm^{-1} due to T-O-T symmetrical bending at the early stages of crystallization. It is followed by a "mordenite-like" amorphous phase, with disordered four- and five-membered aluminosilicate rings that then quickly connect to form zeolite crystals. Such framework is characterized by the bands at 470 and 400 cm^{-1}, corresponding to the T-O-T symmetrical bending modes.

In the organic preparation, similar intermediates are also observed at the early stages of synthesis. The bands at 600, 780, and 1030 cm^{-1} are characteristic of monomeric and dimeric silicate species trapped in the gel, which is in contrast to the inorganic synthesis without soluble silicate species. The band at 490 cm^{-1} due to disordered four-membered rings is also observed as in the inorganic preparation. However, the bands at 390 and 470 cm^{-1} characteristic of the mordenite framework appear before the actual crystals are detected. Therefore, it can be concluded that the basic units do not readily condense to form zeolite crystals, thereby suggesting that the role of the quaternary ammonium cation may be to stabilize the mordenite nuclei for extended periods of time until the proper connectivity is established to form zeolite crystals.

4. Ferrierite

Ferrierite is distinct from other zeolites because it does not contain four-membered aluminosilicate rings, but is composed of five-, six-, eight-, and ten-membered rings. Thus, its Raman spectra do not show a strong band at higher frequency range (480–530 cm^{-1}) like those for zeolite A, X, Y. Similar to ZSM-5, mordenite and ZSM-48 with five-membered rings, the T-O-T bending mode results in a band at 435 cm^{-1}. It is difficult to synthesize ferrierite from a completely inorganic system, whereas the addition of organic structure directing agents such as pyrrolidine greatly speeds up the process.

The evolution of the ferrierite structure from an inorganic and organic gel system was investigated using Raman spectroscopy (324). In the inorganic system, Raman bands between 400 and 500 cm^{-1} correspond to the gel state, which is primarily made up of four-membered aluminosilicate rings. The addition of pyrrolidine results in rapid transformation of the gel to a more ferrierite-like structure characterized by the appearance of the Raman band at 438 cm^{-1}. The NH_2^+ rocking mode of the pyrrolidine associated with the gel at 898 cm^{-1} undergoes significant changes during nucleation. These data are consistent with a zeolite growth process that proceeds from a global ordering of the aluminosilicate gel at the initial stages to the subsequent buildup of smaller domains and finally to the assembly of the specific units with the characteristics of the zeolite itself.

5. ZSM-5

Dutta and coworkers also studied the formation of ZSM-5 during its crystallization stages, in both solid and liquid phases (312). Figures 33 and 34 show the Raman spectra of the

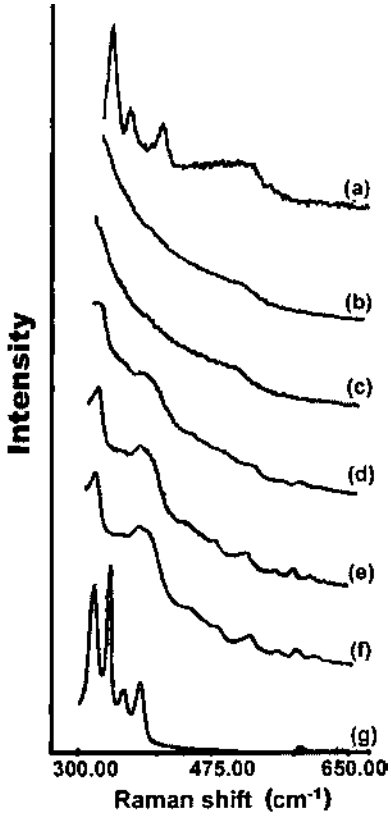

Fig. 33 Raman spectra in the region 300–650 cm^{-1} of (a) 0.5 M tetrapropylammonium bromide, and solid samples present during various stages of zeolite crystallization: (b) 1 day, (c) 3 days, (d) 4 days, (e) 6 days, (f) 9 days, (g) tetrapropylammonium bromide crystals. (From Ref. 312.)

solid phase between 300–650 cm^{-1} and 650–1550 cm^{-1} at various stages of the crystallization process. In the lower frequency region at the beginning period, a broad band centered at 460 cm^{-1} due to the aluminosilicate framework is observed. As the most prominent feature in the Raman spectrum at the earliest stages of the synthesis, this band is typical of amorphous or vitreous silica and has been assigned to ν_s(Si-O-Si) of five- and six-membered silicate rings.

The XRD-detectable crystals appear after 4 days of heating, with considerable changes in the Raman spectrum of solid phase. These changes include a marked increase in intensities of bands at 373, 432, 473, and 820–832 cm^{-1} due to aluminosilicate zeolite framework. In the intermediate stages of zeolite A and Y synthesis, a prominent band at 500 cm^{-1} emerges, which is assigned to the four-membered aluminosilicate rings (22,306,323,326). However, no such bands are observed in case of ZSM-5, indicating that there is no four-membered but five-membered ring structure that appears as the original structure units throughout the synthesis.

E. Charge-Balancing Cations

Charge-compensating cations exchanged within the channel and cage systems of zeolite structures give rise to the transitional vibrations which are located in the far-IR region

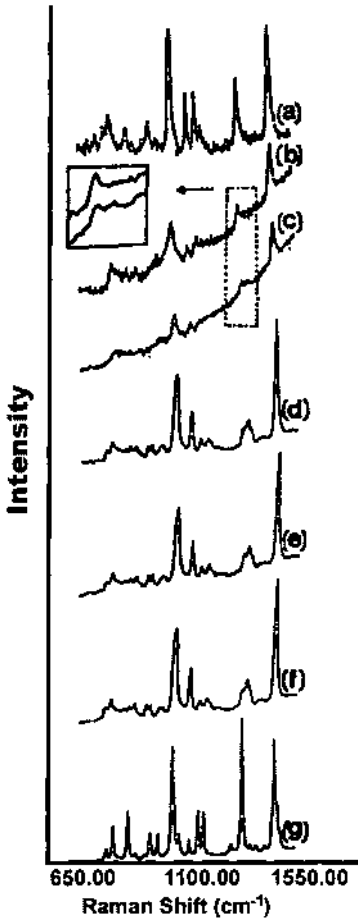

Fig. 34 Raman spectra in the region 650–1150 cm^{-1} of (a) 0.5 M tetrapropylammonium bromide, and solid samples present during various stages of zeolite crystallization: (b) 1 day, (c) 3 days, (d) 4 days, (e) 6 days, (f) 9 days, (g) tetrapropylammonium bromide crystals. (From Ref. 312.)

(59,62), but they also have an influence on the position of framework Raman bands (58). Brémard and coworkers obtained the low-frequency Raman spectra of the fully dehydrated zeolites with the cubic faujasitic topology (314,329). At higher aluminum content the intensities of some minor bands increase and the most striking feature is the appearance of supplementary bands in the low-frequency range near 75 and 120 cm^{-1}, which can be assigned to the translatory motions of the extraframework Na^+ cations (314,330). There are four positions for the extraframework cations in faujasitic zeolites: site I at the center of the prismatic cage, site I′ in the sodalite cage and site II and III in the supercage (331).

It has been observed by far-IR spectroscopy that some extraframework cation modes of fully dehydrated X and Y zeolites occur below about 200 cm^{-1} (62,332). The supplementary degrees of freedom introduced by the translation of motions of the charge-balancing cations in the sites I′, II, and III are expected to be seen by Raman scattering according to the factor group analysis (314). The translational motions of the

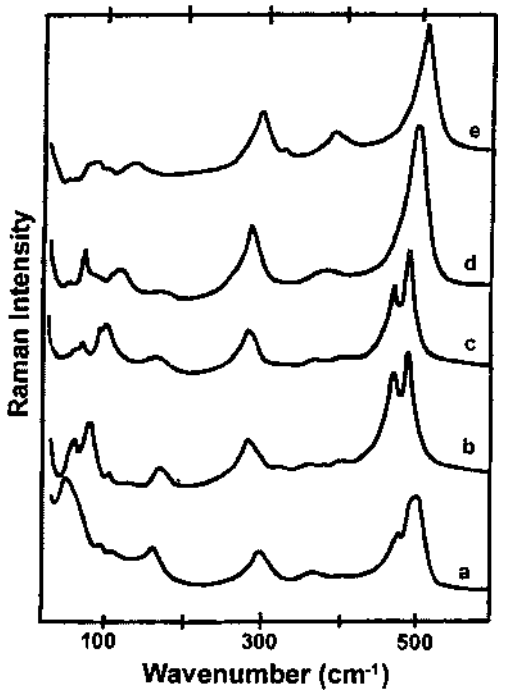

Fig. 35 Raman spectra (300 K) of the dehydrated exchanged Y zeolites: (a) Cs-Y, (b) Rb-Y, (c) K-Y, (d) Na-Y, (e) Li-Y. Excitation radiation: 568.2 nm. (From Ref. 314.)

cations located in the site I are not Raman active but IR active. The replacement of the Na^+ cations by H^+, Li^+, Rb^+, Cs^+, Tl^+, Ca^{2+}, and Mg^{2+} produces significant changes in the position and intensity of the most prominent bands corresponding to framework motions near 500 and 300 cm^{-1} (Fig. 35).

Nevertheless, depending on the nature and the number of the extraframework cations, all the high-frequency bands assigned to the framework vibrations hardly shift, whereas the relative intensity varies markedly. In contrast, the low-frequency bands whose frequencies are the most sensitive to the cation exchange are assigned to the translational motions of the extraframework cations (314). No Raman band can be detected in the 200–100 cm^{-1} region attributed to the IR-active translational motions.

Only one or two features assignable to the translational motions of cations can be distinguished in the low-frequency region (Fig. 36). Their wavenumbers decrease progressively as the mass of the cation increases from Li^+ to Cs^+. The remaining lowest frequency Raman bands are representative mainly of the framework deformation motions including the fluctuations of the pore windows (330,332,333). The frequency shifts around 300 and 500 cm^{-1} could be attributed to slight structural changes of the framework upon exchange of the extraframework cations.

Dutta and coworkers made a systematic study of the Raman spectra of hydrated zeolite A and the influence of exchangeable cations Li^+, Na^+, K^+, Tl^+, NH_4^+ (311). Figure 37 shows the Raman spectra of ion-exchanged hydrated zeolite A in 300–1200 cm^{-1}. The only bands observed above 1200 cm^{-1} are due to lattice water bands at ~1600 and 3300–3600 cm^{-1}. There are some significant changes in the vibrational spectrum as Na^+ is replaced by Li^+, K^+, Tl^+, and NH_4^+ ions.

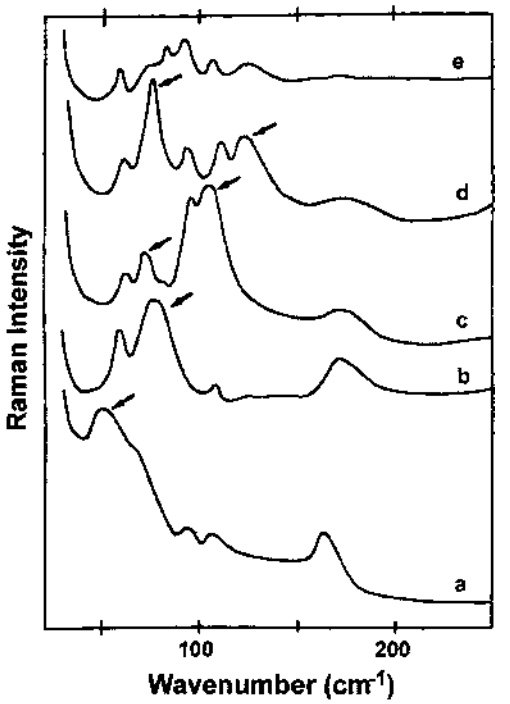

Fig. 36 Low-frequency Raman spectra (300 K) of the dehydrated exchanged Y zeolites (a) Cs-Y, (b) Rb-Y, (c) K-Y, (d) Na-Y, (e) Li-Y. Excitation radiation: 568.2 nm. (From Ref. 314.)

The small size of Li^+ considerably increases the electrostatic interaction between the cation and the zeolite framework. Li^+ is also strongly polarizing and has a great tendency toward coordination. These effects pull the zeolitic oxygen atoms toward the cation, distorting the framework structure and causing a decrease in Si-O-Al angles as compared to Na-A. The vibrations due to Si-O motion at 937 and 1084 cm^{-1} are lower than in the Na-A, whereas the 730 cm^{-1} band involving A1-O motion has increased in frequency. The increase in the SiO_4 deformation mode at 497 cm^{-1} on exchanging with Li^+ is also a reflection of the increased Si-O bond order that would arise from a decrease of the Si-O-Al angle.

The Raman frequencies of Na-A, K-A, and Tl-A exhibit a pattern of decreasing frequency on going from Na^+ through K^+ to Tl^+, e.g., 1099 > 1095 > 1084 cm^{-1}; 971 > 960 > 952 cm^{-1}; 699 > 694 > 665 cm^{-1}; and 490 > 487 > 482 cm^{-1}. The similar pattern of the Raman spectra of these ion-exchanged zeolites and the decrease in frequencies suggests that no major distortion of the lattice takes place and that these cations occupy similar sites.

There is a striking similarity between the general Raman spectrum of Na-A and NH_4-A, indicating that no distortion of the zeolite lattice takes place and the increase in frequencies is a reflection of the electronic environment of T-O bonds.

F. Raman Spectroscopic Studies of Adsorbed Molecules

The relatively low intensity of the Raman bands of zeolite in the low-frequency region may make it easy to detect the vibrational bands of adsorbed molecules in the far-IR region.

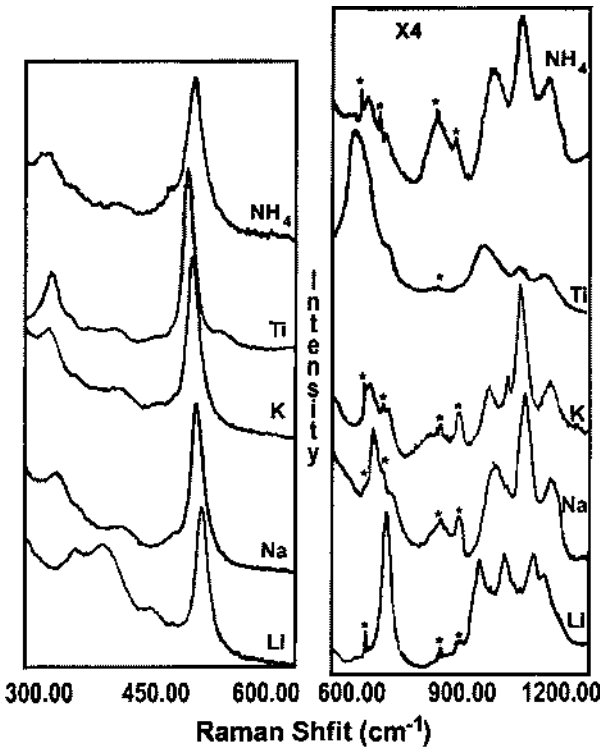

Fig. 37 Raman spectra of hydrated zeolite A exchanged with Li^+, Na^+, K^+, Tl^+, and NH_4^+ ions: laser line, 4579 Å; laser power, 150 mW; slit width, 5 cm^{-1}. (The asterisks denote plasma lines.) (From Ref. 311.)

This is in contrast to the situation of IR spectroscopy. The IR signals (below 1200 cm^{-1}) of the adsorbed molecules are often masked by the very strong adsorption bands of the zeolite framework, which restricts the IR study to the limited spectral region between 4000 and 1200 cm^{-1}. Since Raman spectra of the adsorbate–zeolite system are often obscured by strong fluorescence in the visible region, the adsorption/reaction of molecules in zeolites has been studied mainly by FT Raman spectroscopy and UV Raman spectroscopy. FT-Raman spectroscopy has been used to study the adsorption of a series of aromatic compounds, including benzene, chlorobenzene, toluene, *p*-dichlorobenzene, *p*-xylene, and *p*-chlorotoluene on completely siliceous zeolites with the MFI structure (334–341). The aromatic C-H stretching frequency was shown to be sensitive to the interactions with the pore walls and could be used to detect zeolite structural phase transitions as a function of adsorbate loading.

Taking the adsorption of *p*-xylene (334) as an example, the spectrum of *p*-xylene on ZSM-5 with low loadings of 1.5–4 molecules/u.c. (unit cell) differs mainly in frequencies from that of pure *p*-xylene in the ring C-H stretching region, i.e., the ring C-H stretching modes in the spectrum of adsorbed *p*-xylene shift to higher frequencies in contrast to those of the pure *p*-xylene. The observed large shifts to higher frequencies are attributed to the restriction of the C-H stretching motions from the surrounding framework. Interestingly, the frequencies of the C-H stretching modes for the methyl groups remain essentially unchanged upon adsorption. It is suggested that the long axis of *p*-xylene is oriented along

the channel axis and, consequently, the methyl C-H stretching vibrations are much less restricted by the framework. With increasing the loading of *p*-xylene from 4 to 5 molecules/u.c., the spectrum of adsorbed *p*-xylene shows distinct changes, indicating the phase transition of the host framework at a loading of 5 molecules/u.c. The phase transition behavior of the ZSM-5 framework is readily followed by the changes in the linewidth of the vibrational modes of adsorbed *p*-xylene. For example, the width of ν_8 shows a sudden increase at a loading of 5 molecules/u.c. (see Fig. 38A). Also, many of the Raman modes of *p*-xylene show quite large shifts to higher wavenumbers upon transition from the low- to high-loaded form. Figure 38B shows an abrupt change in the wavenumber of the C-CH_3 in-plane bending mode, where the phase transition occurring at a loading of 5 molecules/u.c. is evident. The phase transition of ZSM-5 is also evidenced by the changes of zeolitic framework vibrations upon *p*-xylene adsorption. The results of *p*-xylene/ZSM-5 system are in agreement with those of NMR and XRD (334).

Subsequent experiments (335–341) show that similar phase transitions of the host zeolite occur with the other aromatic sorbates as well. These results demonstrate two important points. First, Raman spectroscopy is a useful tool for monitoring changes in zeolite structure. Second, the results show that transformations in the zeolite structure commonly accompany the adsorption of molecules into the zeolite pores. These structural transformations contribute to the adsorption energy, the activation energy, and

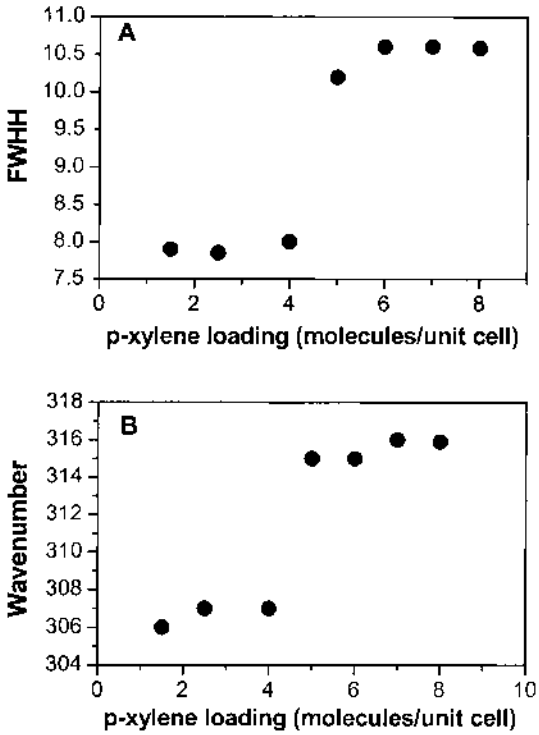

Fig. 38 (A) Plot of the full width at half height (FWHH) in cm^{-1} of the Raman band ν_8 (1620 cm^{-1}), an aromatic C-C stretching mode, of *p*-xylene adsorbed in H-ZSM-5 as a function of the loading. (B) Plot of the frequency in cm^{-1} of the C-CH_3 bending mode of *p*-xylene adsorbed in H-ZSM-5 as a function of loading. (From Ref. 334.)

enthalpy associated with zeolite-catalyzed reactions involving the formation of aromatic compounds such as in coke formation in the zeolite. The phase transitions of zeolite should be further studied in order to arrive at a complete understanding of zeolite catalysis (342).

In recent years, Brémard and coworkers, using the situ FT Raman spectroscopy, studied the adsorption of several aromatic molecules in different zeolites, e.g., benzophenone and benzil molecules in faujasitic zeolites (343), 2,2′-bipyridine in faujasitic zeolites (344), in nonacidic MFI zeolites (345), and in acidic ZSM-5 zeolites (346); biphenyl occluded in ZSM-5 (347), Al-ZSM-5 (348), faujasitic zeolites (349), NaX zeolites (350), nonacidic MFI-type zeolites (351), and nonacidic faujasitic Y zeolites (352); 4,4′-bipyridine in Na(n)ZSM-5 zeolites (353) and acidic ZSM-5 zeolites (346). In combination with theoretical calculation, these Raman investigations give information on the location, conformation, and diffusion of the guest molecules inside the pores or supercages of different types of zeolites (e.g., acidic, nonacidic, and cation-modified zeolites).

V. UV RAMAN SPECTROSCOPIC STUDIES OF MICROPOROUS MATERIALS

A. Difficulties of Visible Raman Spectroscopy in the Characterization of Microporous Materials

Raman spectroscopy is an important spectroscopic technique that is a powerful tool for characterizing the structures of microporous materials as well as many other materials (354). The visible laser lines are usually used as the excitation sources for conventional Raman spectroscopy. Unfortunately, the fluorescence frequently occurs in the visible or near-UV region, and the intensity of the fluorescence is much stronger than that of Raman signal by several orders of magnitude. As a result, the visible Raman spectra are often obscured by the strong fluorescence interference. Another shortcoming of conventional Raman spectroscopy is the inherently low Raman scattering intensity.

The fluorescence interference is extremely severe for most microporous materials because the fluorescence impurity, such as the templates, is frequently present in the samples. In particular, the hydrocarbon species, which has the strong fluorescence, inevitably derives under working conditions if microporous materials are used as catalysts. It is hard to obtain the visible Raman spectra once the surface fluorescence occurs. Therefore, avoiding or eliminating the fluorescence interference and increasing the sensitivity are the urgent requirements for the effective application of Raman spectroscopy in the characterization of microporous materials.

B. UV Raman Spectroscopy

It has been a challenging and important task to make the Raman spectroscopy more practical in the characterization of microporous materials, although there have been efforts made before. A recent advance in the Raman spectroscopic studies is the successful application of UV Raman spectroscopy in the study on catalytic materials, including microporous materials (38). Several advantages of UV Raman spectroscopy have been explained in the theoretical section. The advantages of UV Raman spectroscopy over conventional Raman spectroscopy are confirmed by a number catalyst examples (36): zeolites (ZSM-5, USY) (38), coke formation on zeolites (37), superacid catalyst (sulfated zirconia) (39), transition metal substituted zeolites (23,355), and supported oxides (356,357).

C. UV Raman Spectra of Microporous Materials

Figure 39 (42) shows the UV Raman spectra of various aluminosilicate zeolites. As compared with the visible Raman spectrum, the UV Raman spectrum exhibits the following obvious features: (a) Strong Raman bands with a high signal-to-noise ratio are obtained. The fluorescence is completely avoided in the UV Raman spectra because fluorescence interference does not normally occur in the UV region for aluminosilicate

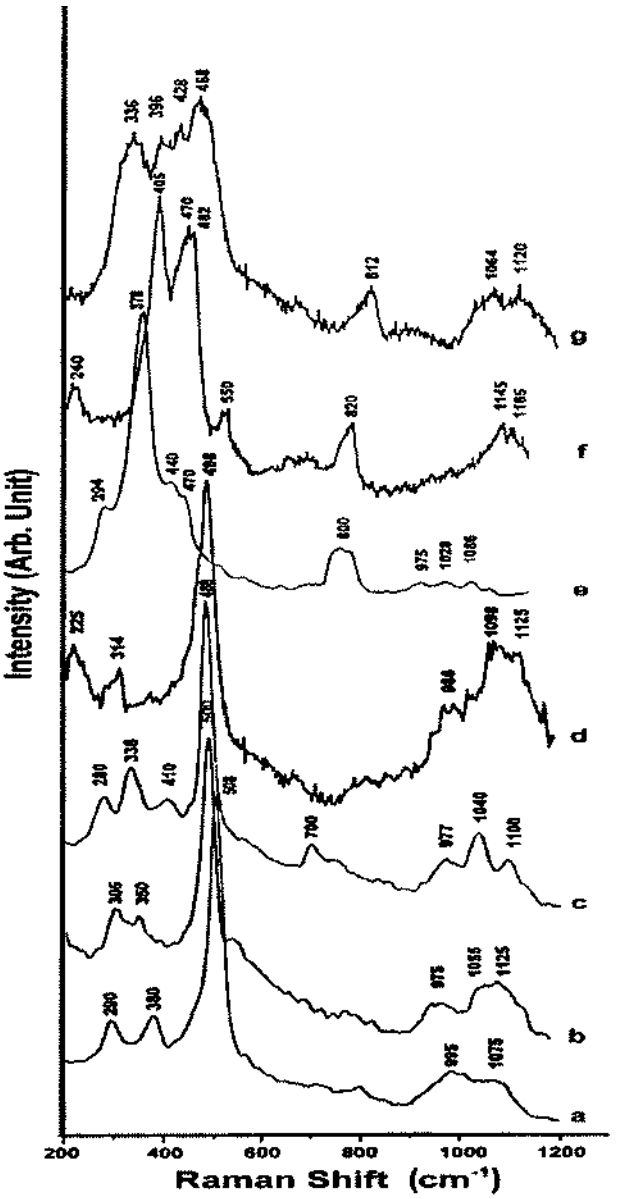

Fig. 39 UV Raman spectra of aluminosilicate zeolites (a) X, (b) Y, (c) A, (d) L, (e) ZSM-5, (f) MOR, and (g) beta (excitation at 244 nm). (From Ref. 42.)

zeolite (358). (b) The UV Raman spectra were collected for the samples do not need any further pretreatments (*e.g.*, heating, oxygen treatment, and evacuation). On the contrary, the visible Raman spectra were obtained only for the samples with careful pretreatments, such as calcination and dehydration (5–24 h) (359), and the fluorescence was often present, even if the sample was well pretreated. The detailed assignment of the UV Raman spectra listed in Fig. 39 is described as follows.

1. Zeolite X

The UV Raman spectrum of zeolite X with a Si/Al ratio of 1.08 shows bands at 290, 380, 508, 995, and 1075 cm^{-1} (Fig. 39a). The strongest band at 508 cm^{-1} is assigned to the bending mode of the characteristic four-membered rings (58,299,306,360), and the bands at 290 and 380 cm^{-1} are assigned to the bending mode of the six-membered rings (22,58,360–362). The bands at 995 and 1075 cm^{-1} are assigned to asymmetrical stretching frequencies of T-O in zeolite X (361,363).

2. Zeolite Y

The UV Raman spectrum of zeolite Y (Fig. 39b) shows bands at 305, 350, 500, 975, 1055, and 1125 cm^{-1}. The framework topology of zeolite X is the same as that of zeolite Y, and the only difference is the Si/Al ratio. Therefore, the assignments for zeolite Y are the same as those for zeolite X. As compared with the spectrum of zeolite X, the bands in the Raman spectrum of zeolite Y are shifted by several wavenumbers. For examples, the strongest band at 508 cm^{-1} for zeolite X is shifted to 500 cm^{-1} for zeolite Y; the band at 290 cm^{-1} for zeolite X is shifted to 305 cm^{-1} for zeolite Y. All these results are attributed to the change in the Si/Al ratio from 1.08 for zeolite X to 2.60 for zeolite Y.

3. Zeolite A

Figure 39c shows the UV Raman spectrum of zeolite A with a Si/Al ratio of 1.0. The bands appear at 280, 338, 410, 488, 700, 977, 1040, and 1100 cm^{-1}. As with faujasite, zeolite A contains four- and six-membered rings (364). Therefore, the assignment of the bands in the UV Raman spectrum for zeolite A should be similar to the one for zeolites X and Y. The strongest band at 488 cm^{-1} is assigned to the bending mode of four-membered Si-O-Al rings (267,313). The bands at 338 and 410 cm^{-1} are attributed to the bending mode of six-membered Si-O-Al rings (22,361,362). The bands at 977, 1040, and 1100 cm^{-1} are ascribed to asymmetrical T-O stretching motions (310,311,313,365). A new band at 700 cm^{-1}, which does not appear in the spectra of zeolites X and Y, could be assigned to the T-O stretching mode of zeolite A, in particular to the contribution of the four-membered rings present in zeolite A (310).

Zeolite A exhibits a band at 280 cm^{-1}, in addition to the three bands at 290–305, 338–380, and 500–508 cm^{-1} assigned to four- and six-membered rings in zeolites X and Y. In early reports (304,305,310), no band at about 280 cm^{-1} appeared in the visible Raman spectra for zeolite A due to the strong background fluorescence. On the other hand, the correlation between the Raman bands in the region 300–600 cm^{-1} and the size of the rings in silicate and aluminosilicate materials as well as in aluminosilicate zeolites has already been observed, and it was found that the smaller rings give bands at higher frequencies (299). Therefore, the band at 280 cm^{-1} is attributed to the bending mode of higher rings than six- and four-membered rings, possibly of the eight-membered rings of zeolite A.

4. Zeolite L

The UV Raman bands of zeolite L are shown in Fig. 39d. Bands appear at 225, 313, 498, 986, 1098, and 1125 cm^{-1}. Again, the strongest band at 498 cm^{-1} is assigned to the bending mode of four-membered rings, and the band at 314 cm^{-1} is assigned to the bending mode of six-membered rings present in zeolite L (363). The bands at 986, 1098, and 1125 cm^{-1} are also attributed to asymmetrical stretching vibration frequencies of the T-O bonds in the sample. Interestingly, zeolite L exhibits a band at 225 cm^{-1}, which has not been observed in visible Raman spectroscopy. The band at 225 cm^{-1} should be assigned to the bending mode of eight-membered rings (T-O-T) of zeolite L (299).

5. Zeolite ZSM-5

Figure 39e shows the UV Raman spectrum of zeolite ZSM-5 with bands at 294, 378, 440, 470, 800, 975, 1028, and 1086 cm^{-1}. The strongest band is observed at 378 cm^{-1} rather than near 500 cm^{-1} as for zeolites X, Y, A and L (Fig. 39a–d). We assign this band to the bending mode of five-membered rings (299,305,312). The band at 294 cm^{-1} is assigned to the bending mode of six-membered rings (22,299,361,362). The bands at 440 and 470 cm^{-1} are assigned to four-membered rings (299,305). The band at 800 cm^{-1} is assigned to symmetrical stretching, and the bands at 975, 1028, and 1086 cm^{-1} to asymmetrical stretching vibrations of Si-O bonds in ZSM-5, which is consistent with previous assignments in visible Raman spectroscopy (312,361).

6. Zeolite Mordenite

The UV Raman spectrum of zeolite mordenite is shown in Fig. 39f. Bands appear at 240, 405, 470, 482, 550, 820, 1145, and 1165 cm^{-1}. The framework structure of mordenite consists of four-, five-, and eight-membered T-O-T rings. Therefore, the band at 405 cm^{-1} is assigned to the bending mode of five-membered rings, and the bands at 470 and 482 cm^{-1} are assigned to the bending modes of four-membered rings. The band at 820 cm^{-1} is assigned to symmetrical stretching motions of T-O bonds, and the bands at 1145 and 1165 cm^{-1} are assigned to asymmetrical stretching motions of T-O bonds. These assignments are in good agreement with those for mordenite in visible Raman spectroscopy (322). Notably, a broad band appears at 240 cm^{-1}, which has not been observed in visible Raman spectroscopy. Similarly, this band is assigned to the bending mode of eight-membered rings in mordenite, in agreement with our assignments for zeolite A and L.

The Raman bands for zeolite mordenite are relatively broad, as compared with those of ZSM-5 and zeolites X and A. For example, the band near 480 cm^{-1} (Fig. 39c) is split into two bands at 470 and 482 cm^{-1} (Fig. 39f). This may be interpreted in terms of the order of the zeolite framework. The arrangement of zeolite building units in mordenite is not as uniform as in ZSM-5 and zeolites X and A, resulting in broad bands in Raman spectroscopy.

7. Zeolite Beta

It is difficult to obtain the Raman spectrum of zeolite beta by conventional Raman spectroscopy because of its low symmetry (299) and strong background fluorescence. Zeolite beta is an intergrowth of two distinct but closely related structures. Polymorph A is a tetragonal system, whereas polymorph B is monoclinic (366). The UV Raman spectrum of zeolite beta shows obvious bands appearing at 336, 396, 428, 468, 812,

1064, and 1120 cm^{-1}, as shown in Fig. 39g. According to the assignments of this work and results from the literature (299), it is suggested that the band at 336 cm^{-1} is assigned to the bending mode of six-membered rings, the band at 396 cm^{-1} is ascribed to the bending mode of five-membered rings, and the bands at 428 and 468 cm^{-1} are attributed to four-membered rings. The band at 812 cm^{-1} is due to the T-O symmetrical stretching mode, and the bands at 1064 and 1120 cm^{-1} are assigned to T-O asymmetrical stretching mode.

D. Aluminosilicate Zeolites With Various Si/Al Ratios

It has been reported that the Si/Al ratio of zeolites strongly influences the band position and band intensity of Raman spectra (308,310,367), but it is difficult to distinguish the species of Si-O-Si and Si-O-Al in Raman spectroscopy (308,367). Yu et al. (42) recorded the UV Raman spectra of two typical zeolites, zeolite X (with low Si/Al ratio) and ZSM-5 (with high Si/Al ratio). Figure 40 shows the UV Raman spectra of zeolite X with Si/Al ratios of 1.00–1.20. The sample with Si/Al = 1.20 (Fig. 40a) exhibits the main band at 505 cm^{-1} with broad bands at 300, 369, 958, and 1076 cm^{-1}. For Si/Al = 1.10, the spectrum (Fig. 40b) shows a stronger band at 507 cm^{-1}. When the Si/Al ratio is further decreased to

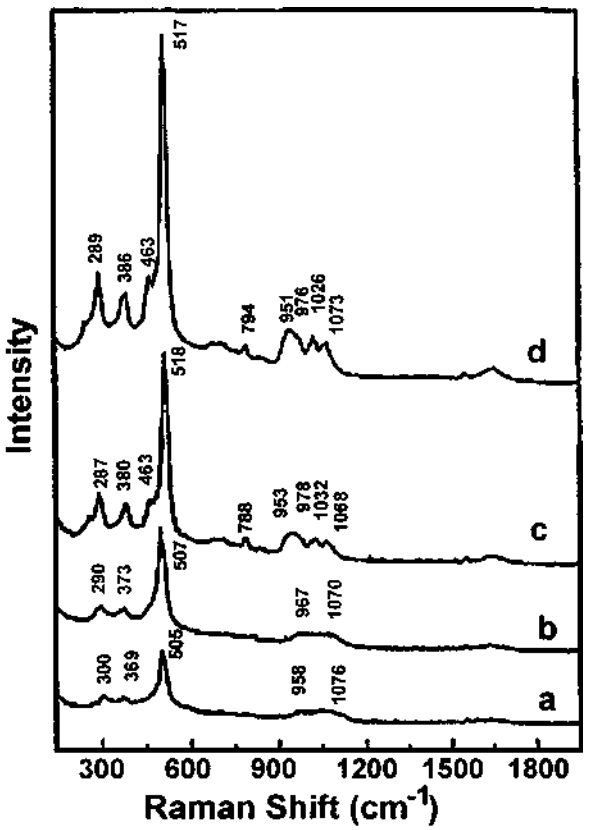

Fig. 40 UV Raman spectra of X zeolites with different Si/A1 ratios: (a) 1.20, (b) 1.10, (c) 1.06, and (d) 1.00 (excitation at 244 nm). (From Ref. 42.)

1.06, the spectrum (Fig. 40c) gives more intense bands at 287, 380, and 516 cm^{-1} together with small bands at 463 and 788 cm^{-1}. At the same time, the bands at 958 and 1076 cm^{-1} (Fig. 40a) are split into four bands at 953, 978, 1032, and 1068 cm^{-1}. Finally, for Si/Al = 1.00, the spectrum (Fig. 40d) shows still more intense bands at 289, 386, 463, 517, 794, 951, 976, 1026, and 1073 cm^{-1}.

The signal-to-noise ratio (*S*/*N*) in the UV Raman spectra of zeolite X increases with decreasing Si/Al ratio. This phenomenon may be attributed to the change in the structural order of zeolite X with the Si/Al ratio. At an Si/Al ratio of 1.20, most T-O-T of the sample are Si-O-Al, but there are still some of Si-O-Si. In this case, the Raman spectrum mainly exhibits the bands associated with Si-O-Al vibrations. When the Si/Al ratio is 1.00, nearly all of the T-O-T are Si-O-Al. In this case, the structural order of zeolite X is highest, and the signal-to-noise ratio of UV Raman spectrum is the highest. Obviously, the bands at 1000 cm^{-1} region associated with Si-O-Al become evident and distinct at an Si/Al ratio of 1.0.

ZSM-5 has a high Si/Al ratio but with similar structure of X; however, the UV Raman spectrum of ZSM-5 (Fig. 39e) is completely different from that of zeolite X (Fig. 40). For the Si/Al ratio of ∞ (pure silica), the band intensity is strongest, and bands appear at 294, 378, 800, 975, 1028, and 1086 cm^{-1}. When the Si/Al ratio of ZSM-5 is reduced to 100, the bands are much weaker, and bands appear at 298, 384, 806, 980, 1050, and 1095 cm^{-1}. When the Si/Al ratio of ZSM-5 is further decreased to 47, weak bands at 298, 384, 806, 980, and 1099 cm^{-1} are observed. The band intensity and S/N in the UV Raman spectra of ZSM-5 increase remarkably with the Si/Al ratio, indicating that the structure order is improved with the higher Si/Al ratio. This is just reversed for zeolite X. The band position in the UV Raman spectra of ZSM-5 is insensitive to the Si/Al ratio, and this behavior is also different from that of zeolite X. The amount of Al in ZSM-5 is relatively small, so that a change in the Si/Al ratio hardly influences the vibrations of Si-O-Si.

E. Crystallization of Microporous Materials

Raman spectroscopy is a potentially suitable technique to characterize the crystallization mechanism of microporous materials because Raman spectra can be recorded for the samples in aqueous solution and solid state. So it is possible to follow the whole procedure of a zeolite synthesis from the very beginning stage (aqueous solution) to the final stage (crystallized solid), including the crystallization process, by using Raman spectroscopy. Although few visible Raman spectroscopic studies were reported for the crystallization of zeolites Y (22), MOR (322), and ZSM-5 (312), conventional Raman spectroscopy has not been well used to study the synthesis mechanism mainly because the fluorescence interference often arises from the templates and other impurities in the synthesis system. In the UV Raman spectroscopic characterization of the crystallization of zeolite X (43), the fluorescence was completely avoided so that the Raman spectra were recorded for both the liquid and solid phases of zeolite X during its crystallization. UV Raman spectra together with NMR spectra indicate that $Al(OH)_4^-$species are consumed from the liquid phase and incorporated into the solid phase, accompanied by the depolymerization of polymeric silicate species from the solid phase into monomeric silicate species in the liquid phase. By condensation of $Al(OH)_4^-$and depolymerized silicate species, amorphous aluminosilicate species composed mainly of four-membered rings are formed in the solid phase in the early stage of nucleation. The four-membered rings interconnect with each other via six-membered rings to form β cages. Finally, the zeolite X is formed through connecting the double six-membered rings of the β cages.

F. UV Resonance Raman Spectroscopic Identification of Transition Metal Ions Incorporated in the Framework of Molecular Sieves

1. Introduction

Microporous materials incorporating transition metal ions in their framework are a class of new materials that show some unique properties that are particularly important in catalysis. The most useful property is their redox potential, which can be applied to creation of new catalysts for selective oxidation of a wide range of hydrocarbons, such as epoxidation of olefins and hydroxylation of benzene using H_2O_2 as the oxidant. The most interesting question concerning the microporous materials incorporated with transition metal ions in their framework is how to identify the transition metal ions in the framework. There have been excellent reviews and articles addressing this issue. One of the advances in this research direction is that the framework transition metal ions can be selectively examined by UV resonance Raman spectroscopy. The transition metal ions substituted in the framework of molecular sieves show a charge-transfer transition between the transition metal ions and the framework oxygen anions, and these transitions are usually in the UV region. Therefore the UV resonance Raman spectra can be obtained by exciting these transitions with the UV laser. Accordingly, the framework transition ions can be selectively identified based on the resonance Raman effect because the enhanced resonance Raman bands are directly associated with the framework transition metal ions. In the following sections, three typical examples—TS-1, Fe-ZSM-5, and V-MCM-41—are discussed and demonstrate how the framework transition metal ions can be characterized by UV resonance Raman spectroscopy.

2. Characterization of TS-1 Zeolites

The titanium-substituted silicalite-1, TS-1 zeolite with a MFI structure, was first prepared by Tarahasso and colleagues (368) in 1983. TS-1 zeolite has received great interest during the last decade because of its excellent catalytic properties in a range of selective oxidation reactions with aqueous hydrogen peroxide (30% H_2O_2) as oxidant under mild conditions (369–373). It is commonly believed that isolated titanium in the framework of the TS-1 zeolite, hereafter denoted as Ti-O-Si in this chapter, is the active site for the selective oxidation although the exact nature of the active site is still in dispute (374). There has been extensive characterization of TS-1 zeolite using the following techniques: FTIR and Raman spectroscopy (321,371,372,375–383), UV-vis absorption (377–379,383,384), NMR (379,385–387), EXAFS and XANES (381,382,388,389), ESR (385), XRD (380,390), *ab initio* (391), and so on. A band at 960 cm^{-1} appeared in Raman and IR spectra, was assumed to be the characteristic vibration mode of the framework titanium species, Ti-O-Si. However, this band sometimes appears for silicalite zeolites without substituted titanium or with substituted metals other than titanium, and there is also evidence indicating that this band may be from surface hydroxyl (e.g., Si-OH) (319,392) or defect sites (321). Thus, the key question remains how the framework titanium species can be identified unambiguously.

Using UV resonance Raman spectroscopy (23,25), we have distinguished the framework titanium from framework silicon and nonframework titanium dioxide. It makes use of the resonance Raman effect to selectively enhance the Raman bands associated with the framework titanium while keeping the rest of the Raman bands unchanged. The enhanced Raman bands are directly associated with the framework titanium species Ti-O-Si in the zeolite because the excitation line approaches the charge-transfer absorption of framework

Ti-O-Si species in the UV region (200–250 nm). In addition, the Raman spectrum with the excitation lines in the UV region gives better signal-to-noise ratio than in the visible region, mainly because UV Raman spectroscopy can avoid most of the fluorescence interference from zeolite samples (36–38). Therefore, UV resonance Raman spectroscopy is a potentially powerful technique to characterize the framework titanium in TS-1. This study also demonstrates that the UV resonance Raman spectroscopy is a general technique to identify other transition metals substituted in the framework of a zeolite or molecular sieves, based on the resonance Raman enhancement when there is an absorption due to the charge-transfer transition between the framework metal cations and oxygen anions (24,26).

3. UV Raman Spectra of TS-1 Zeolite

UV–visible diffuse reflectance spectra of TS-1 and silicalite (Fig. 41A) show that there is a typical absorption band centered at 220 nm for TS-1 while no electronic absorption band is observed for silicalite-1. The band at 220 nm originates from the charge transfer of the $p\pi$-$d\pi$ transition between titanium and oxygen of the framework titanium species, Ti-O-Si, in the zeolite (377,384). This transition involves excitation of an electron from a π-bonding molecular orbital consisting essentially of oxygen atomic orbital to a molecular orbital that is essentially a titanium atomic orbital. The tail of the band centered at 220 nm actually extends to 300 nm due to the presence of extraframework titanium species, TiO_2, in the TS-1 zeolite.

Figure 41B shows the UV Raman spectra of TS-1 and silicalite-1 excited by the 244-nm line. There are Raman bands observed for TS-1 at 1170 (shoulder), 1125, 960, 530, 490, 380, 290 cm^{-1} and some weak bands in the 600–800 cm^{-1} region. Of particular interest is the fact that a very strong band at 1125 cm^{-1} is observed for TS-1 although usually the bands in the 1000-cm^{-1} region are difficult to detect with normal Raman spectroscopy. The UV Raman spectrum of silicalite-1 is completely different from that of TS-1. The strong Raman bands at 490, 530, and 1125 cm^{-1}, which appear for TS-1, are absent in the Raman spectrum of silicalite-1. These new bands at 490, 530, and 1125 cm^{-1}

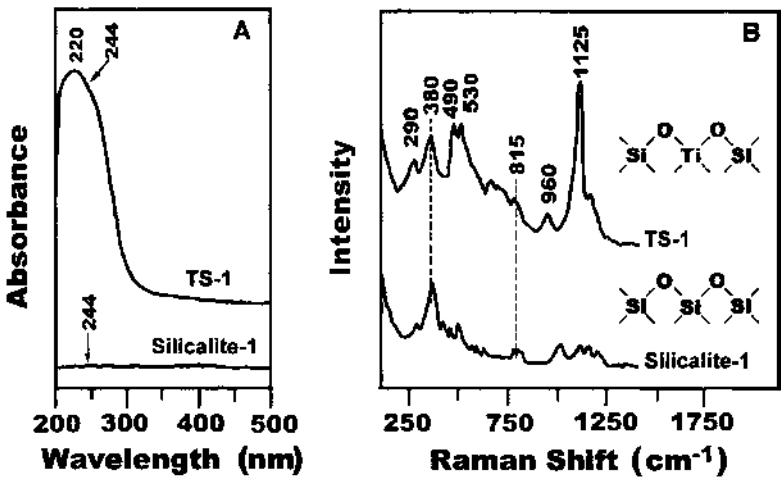

Fig. 41 (A) UV-visible diffuse reflectance spectra of TS-1 and silicalite-1. (B) UV resonance Raman spectra of TS-1 and silicalite-1 excited with the 244-nm line. (From Ref. 25.)

must be from the framework titanium species in TS-1. Several common bands are observed at 290, 380, and 815 cm^{-1} for both TS-1 and silicalite-1 zeolites indicating that these bands are characteristic of silicalite-1 zeolite. The weak band at 960 cm^{-1} in the UV Raman spectrum appears at the same frequency as in FTIR and FT Raman spectra.

Figure 42 exhibits the Raman spectra of TS-1 excited by three different laser lines at 244, 325, and 488 nm, respectively. The strong bands at 490, 530, and 1125 cm^{-1} are observed only when excited with the line at 244 nm. Clearly these bands are due to the UV resonance Raman effect because the 244-nm line is in the absorbance band of the electronic absorption of TS-1 whereas the 325- and 488-nm lines are outside of the absorption band of TS-1 (Fig. 41A). All three spectra have common bands at 290, 380, 815, and 960 cm^{-1}, suggesting that these bands are not due to the resonance Raman effect but are the characteristics of silicalite-1, as shown in Fig. 41B.

In the Raman spectra of TS-1 excited at 325 and 488 nm, three additional bands at 144, 390, and 637 cm^{-1} are observed. These bands are readily attributed to TiO_2 (anatase), indicating that there are extraframework titanium species in the TS-1 sample. However, these bands are absent in the UV Raman spectrum from the excitation at 244 nm. It appears that visible Raman spectroscopy is sensitive to extraframework titanium species, TiO_2, whereas UV Raman spectroscopy is exclusively sensitive to the framework titanium species, Ti-O-Si.

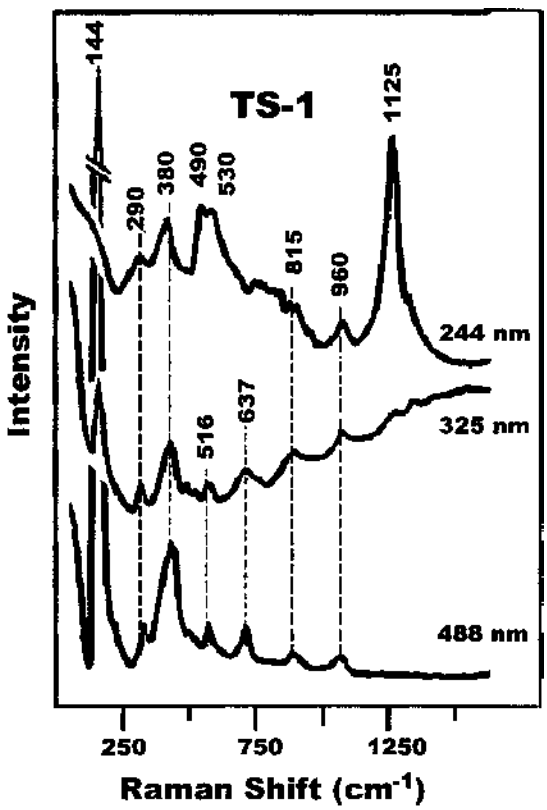

Fig. 42 Raman spectra of TS-1 excited with laser lines at 244, 325, and 488 nm, respectively. (From Ref. 25.)

The Raman spectra of silicalite-1 excited with lines at 244, 325, and 488 nm are almost identical. The interesting bands at 490, 530, and 1125 cm^{-1} are not detected for silicalite-1 for excitation lines from the visible to UV regions. There is no resonance Raman phenomenon observed for silicalite-1 as no enhanced Raman bands are detected for silicalite-1 when the excitation line varied from the visible to the UV regions. This is in good agreement with the UV-visible diffuse reflectance spectrum in Fig. 41A where there is no electronic absorption band for silicalite-1. Thus, it is confirmed that the bands at 490, 530, and 1125 cm^{-1} are solely associated with the framework titanium of TS-1 but not with silicalite-1.

The Raman bands at 290, 380, and 815 cm^{-1} do not vary with the different excitation lines at 244, 325, and 1125 nm, indicating that these bands are the characteristic bands of silicalite-1 itself. In particular, the band at 380 cm^{-1} is the identification of the MFI structure (375). These bands also appear for TS-1, suggesting that TS-1 maintains the structure of silicalite-1. There are some weak bands in the 1000–1200 cm^{-1} region that are also due to silicalite-1. These bands become evident when the excitation is shifted from 488 nm to 244 nm mainly due to less fluorescence interference in the Raman spectrum when the excitation wavelength is shifted from the visible to the UV regions.

The resonance-enhanced Raman bands at 490, 530, and 1125 cm^{-1} can be assigned simply from the analysis of the local unit of a $[Ti(Osi)_4]$, denoted as Ti-O-Si in this chapter. The bands at 490 and 530 cm^{-1} are respectively assigned to the bending and symmetrical stretching vibrations of the framework Ti-O-Si species, and the band at 1125 cm^{-1} is attributed to the asymmetrical stretching vibration of the Ti-O-Si (375,377). The band at 1125 cm^{-1} is most enhanced in the UV resonance Raman spectrum because this vibration mode is more sensitive to the charge-transfer transition of Ti-O-Si.

To rule out the possibility that nanoparticles of TiO_2 in the zeolite may give the resonance Raman band, a sample of TiO_2 with sizes from 1 to 10 nm was also characterized by UV Raman spectroscopy with the excitation at 244 nm. No detectable Raman bands were observed for the nanoparticle TiO_2 in the UV Raman spectra. Therefore, the enhanced Raman bands observed at 490, 530, and 1125 cm^{-1} for TS-1 are solely from the framework Ti-O-Si species.

The evolution of the framework titanium species in TS-1 was followed by UV resonance Raman spectroscopy during the crystallization of the zeolite. The relative intensities of the resonance Raman bands at 490, 530, and 1125 cm^{-1} significantly increased with the crystallization time, while the other bands, e.g., 290, 370, and 960 cm^{-1}, are only slightly changed. In addition, these resonance Raman bands, particularly the band at 1125 cm^{-1}, become narrower for longer crystallization time indicating that the framework titanium becomes more uniform in the TS-1. The fact that the bands at 490, 530, and 1125 cm^{-1} develop with crystallization time strongly suggests that more framework titanium species are derived and/or the structure of the framework titanium becomes more compatible with the silicalite-1 structure. The relative intensities of the resonance bands at 490, 530, and 1125 cm^{-1} can be an estimation of how much framework titanium species is incorporated in the silicalite-1 structure and how well the crystal structure of TS-1 is formed.

Prior to this work, the framework titanium in TS-1 was characterized mainly by the band at 960 cm^{-1} when using FTIR and normal Raman spectroscopy (with the excitations at 488, 514, or 1064 nm). It was assumed that the appearance of the band at 960 cm^{-1} is the indication that framework titanium is formed in the TS-1. However, the assignment of this band has been controversial so far. For example, this band was also assigned to titanyl group Ti═O (375,393), Ti-O stretching, silanol group Si-OH, titanium related defect sites (377), Ti-O-Si bridge (375), and others. This band is detected for TS-1 in this study by UV

Raman and visible Raman spectroscopy (see Figs. 41 and 42), and also by FT Raman spectroscopy. But the relative intensity of this band is almost the same with the different excitation lines (Fig. 42). This clearly means that the band is not a resonance-related Raman band. The fact that the relative intensity of the band at 960 cm^{-1} remains almost unchanged with the crystallization time suggests that the band at 960 cm^{-1} may not be directly associated with the framework titanium species of TS-1.

Three resonance-enhanced Raman bands at 490, 530, and 1125 cm^{-1} are observed exclusively for TS-1 zeolite in the UV resonance Raman spectra. These bands are the characteristics of the framework titanium species in TS-1 zeolite because they appear only when UV laser (244 nm) excites the charge-transfer transition of the framework titanium species in the TS-1 zeolite. The framework titanium in TS-1 can be successfully identified by the UV resonance Raman spectroscopy. The UV resonance Raman spectroscopy of this report also opens up the possibility of identifying the other transition metal cations incorporated into the framework of a zeolite or other molecular sieves.

The assignment of the Raman band at 1125 cm^{-1} due to framework titanium in TS-1 is confirmed by the resonance, whereas the band at 960 cm^{-1} is still controversial. A thorough analysis of the vibrational features of the TS-1 catalyst was made by Ricchiardi et al (394) based on quantitative IR measurements, Raman and UV resonance Raman experiments, quantitative XANES, and quantum chemical calculations on cluster and periodic models. The linear correlation of the intensity of the IR and Raman bands located at 960 and 1125 cm^{-1} and the XANES peak at 4967 eV with the amount of tetrahedral Ti are quantitatively demonstrated. Raman and resonant Raman spectra of silicalite and TS-1 with variable Ti content are presented, showing main features at 960 and 1125 cm^{-1} associated with titanium insertion into the zeolite framework. The enhancement of the intensity of the 1125 cm^{-1} feature and the invariance of the 960 cm^{-1} feature in UV Raman experiments are discussed in terms of resonant Raman selection rules. Quantum chemical calculations on cluster models $Si[Osi(OH)_3]_4$ and $Ti[Osi(OH)_3]_4$ at the B3LYP/6-31G(d) level of theory provide the basis for the assignment of the main vibrational contributions and for the understanding of Raman enhancement. The resonance-enhanced 1125 cm^{-1} mode is unambiguously associated with a totally symmetrical vibration of the TiO_4 tetrahedron, achieved through in-phase antisymmetrical stretching of the four connected Ti-O-Si bridges. This vibration can also be described as a totally symmetrical stretching of the four Si-O bonds pointing toward Ti. The resonance enhancement of this feature is explained in terms of the electronic structure of the Ti-containing moiety. Asymmetrical SiO_4 and TiO_4 stretching modes appear above and below 1000 cm^{-1}, respectively, when they are achieved through antisymmetrical stretching of the T-O-Si bridges, and around 800 cm^{-1} (in both SiO_4 and TiO_4) when they involve symmetrical stretching of the T-O-Si units. In purely siliceous models, the transparency gap between the main peaks at 800 and 1100 cm^{-1} contains only vibrational features associated with terminal Si-OH groups, while in Ti-containing models it contains also the above-mentioned asymmetrical TiO_4 modes, which in turn are strongly coupled with Si-OH stretching modes. Calculations on periodic models of silicalite and TS-1 free of OH groups using the QMPOT embedding method correctly reproduce the transparency gap of silicalite and the appearance of asymmetrical TiO_4 vibrations at 960 cm^{-1} in TS-1.

4. UV Raman Spectra of Fe-ZSM-5

Yu et al. (26) reported the UV resonance Raman characterization of Fe-ZSM-5. The UV Raman spectra of three samples—silicalite-1, Fe-SZSM-5, and a mixture of silicalite-1 and Fe_2O_3—were recorded in order to compare their difference (Fig. 43). Silicalite-1 exhibits

two bands at 380 and 802 cm^{-1} (Fig. 43a), the band at 380 cm^{-1} is assigned to five-membered building unit of MFI-structure zeolites (305,312), and the 802 cm^{-1} band is assigned to the framework symmetrical stretching vibration in ZSM-5 (312,395). It is very interesting to note that Fe-ZSM-5 exhibits new bands at 516, 580, 1026, 1126, and 1185 cm^{-1}, in addition to the bands at 380 and 802 cm^{-1} (Fig. 43b). The chemical analysis of silicalite-1 (Fig. 43a) and Fe-ZSM-5 (Fig. 43b) shows that the difference in chemical composition is only iron in these zeolites. Therefore, the new bands should be related to the contribution of the iron atoms in zeolite. Figure 43c shows the UV Raman spectrum of a mechanical mixture of Fe_2O_3 with silicalite-1, giving similar bands to those of silicalite-1 (Figs. 43a). These results indicate that UV Raman spectroscopy is insensitive to Fe_2O_3 material, and Fe_2O_3 does not exhibit UV Raman bands because the UV Raman bands of Fe_2O_3 are too weak to be detected.

The UV-vis diffuse reflectance spectra of silicalite-1, Fe-ZSM-5, and mechanical mixture of Fe_2O_3 with silicalite-1, which were prepared from fumed silica, were recorded. Silicalite-1 has no any bands in the 200–700 nm region, while Fe-ZSM-5 shows a strong absorption band centered at 240–250 nm. The band at 240–250 nm may be assigned to the $d\pi$-$p\pi$ charge-transfer transition between the iron and oxygen atoms in the framework of Fe-O-Si in zeolite (396,397). Similar phenomena have been observed in Ti-O-Si species of TS-1 (23,384). The UV-vis diffuse reflectance spectrum of mechanical mixture of Fe_2O_3 with silicalite-1 exhibits an absorption band at near 500 nm, indicating that there is no strong absorption band in the UV region (below 300 nm). The UV-vis diffuse reflectance spectra of silicalite-1 and ZSM-5 with an Si/Al ratio of 23 and 100, which were prepared from sodium, silicate, show no obvious absorption bands at 240–250 and 500 nm, suggesting that UV-vis DRS technique is insensitive to a trace amount of iron atoms in zeolites.

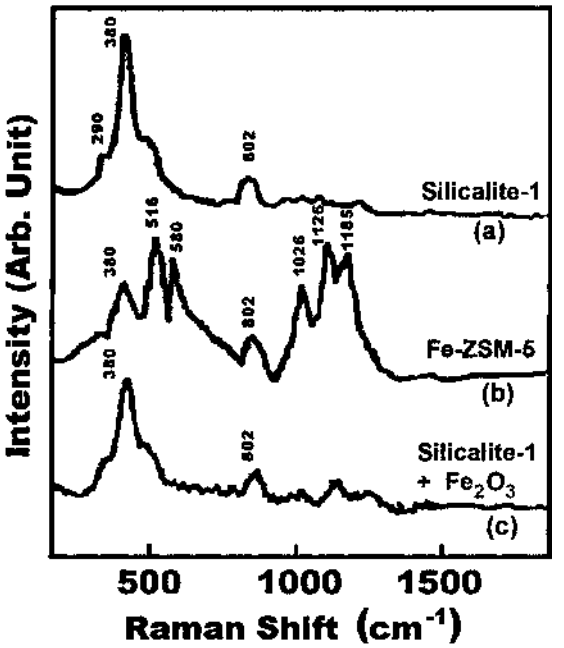

Fig. 43 UV Raman spectra of (a) silicalite-1, (b) Fe-ZSM-5, and (c) mechanical mixture of silicalite-1 with Fe_2O_3, which were prepared from fumed silica as a silicon source. (From Ref. 26.)

5. UV Raman Spectra of V-MCM-41

Similarly, the framework vanadium species in V-MCM-41 was characterized by UV resonance Raman spectroscopy (24). In the UV-vis reflectance diffuse absorption spectra of Si-MCM-41 and V-MCM-41, no electronic absorption band is observed in the UV-vis absorption spectrum of Si-MCM-41. There are the electronic absorptions observed for V-MCM-41 at 270, 340, 410, and 450 nm. The electronic absorptions at 270 and 340 nm are assigned to the charge transfer between the tetrahedral oxygen ligands and the central V^{5+} ion of tetrahedral coordinated V^{5+} in the framework (398–400). Two bands at 410 and 450 nm indicate that the extraframework V^{5+} ions are formed in V-MCM-41. However, the UV-vis electronic absorption of polymerized vanadium oxides supported on SiO_2 also appears in the 250–350 nm region (401). The bands at 250 and 320 nm are observed in the UV-vis diffuse reflectance spectrum of supported vanadium oxides. Hence, the broad bands at 270 and 340 nm are the overlap of the UV-vis bands of both isolated tetrahedral (framework) and polymerized octahedral (extraframework) vanadium sites. A laser line at 244 nm is close to the electronic absorption of the vanadium ions species in both the framework and the extraframework simultaneously.

Figure 44 shows the UV Raman spectra of Si-MCM-41 and V-MCM-41 excited by the 244-nm line. The bands at 490, 610, 810 and 970 cm^{-1} are detected in the visible and UV Raman spectra of MCM-41. These bands are attributed to the fourfold siloxine, siloxane bridges, and silanol groups (399). Visible Raman spectrum of V-MCM-41 shows similar Raman bands to those of the MCM-41, and no Raman bands associated with the

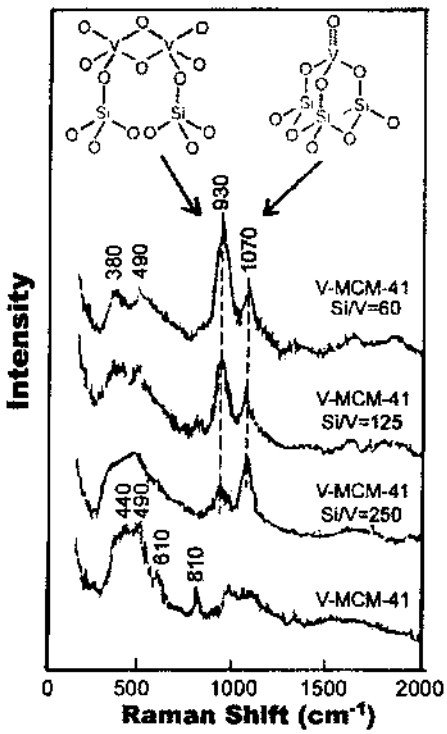

Fig. 44 UV Raman spectra of V-MCM-41 and MCM-41 excited by 244-nm line radiation. (From Ref. 24.)

vanadium species in the framework and extraframework are detected. In the UV Raman spectrum two additional bands at 930 and 1070 cm^{-1} are detected as shown in Fig. 44. The band at 930 cm^{-1} is assigned to the hydrated polymerized vanadium oxides in the extraframework (402). The band at 1070 cm^{-1} is assigned to the V-O symmetrical stretching mode of the vanadium ions in the framework (399,402–404). Considering that the 244-nm line is close to the charge-transfer absorption of the vanadium ions, it is the Raman resonance effect that makes the 930 and 1070 cm^{-1} bands considerably enhanced.

The bands at 930 and 1070 cm^{-1} are assigned to the vanadium species in the extraframework and framework, respectively, because the Raman bands of vanadium species in the framework and extraframework are enhanced by resonance Raman effect simultaneously. The framework vanadium species in MCM-41 is in the distorted tetrahedral form, and that in the extraframework is in the polymerized octahedral form. The concentration of framework vanadium atoms in the zeolite is limited to a certain amount. As the concentration of vanadium species is beyond the limit, the vanadium oxides in the extraframework begin to appear and their amount increases with increasing the concentration of vanadium atoms.

G. UV Raman Spectroscopic Studies of Adsorbed Molecules

Place and Dutta (405) showed the advantages of resonance Raman spectroscopy using visible excitation in distinguishing between acid and base forms in zeolites by adsorption of dye molecules. By taking advantage of the strongly allowed electronic transitions in the dye molecules (large extinction coefficients) and the different absorption maxima of the conjugate acid and base forms of the dye, selective enhancements of the Raman bands specific to each form were obtained. The focus has been on the dye molecule 4-(phenylazo)diphenylamine (PDA) adsorbed onto the faujasitic zeolite NaY. A calibration curve of Raman intensity (peak area) vs. number of protons in supercages was obtained. Because of the inner filter effect, at loadings significantly greater than one proton per supercage, the Raman intensity was found to decrease. The sensitivity of Raman spectroscopy for low proton loadings appears to be considerably better than IR spectroscopy used to estimate the acidity of zeolite surfaces.

However, many of the dyes have radii that are larger than the cage openings of zeolites (typically 4–8 Å). This may lead to size selectivity and may not accurately reflect true site acidity. Thus, it would be advantageous to use small molecules that could freely move about in the inner surfaces of the zeolite. Later, Jakupca and Dutta (406) used 4-aminopyridine to probe the weak acid sites present in NaY by UV resonance Raman spectroscopy. The normal Raman spectrum of this molecule adsorbed in NaY shows bands due to both the neutral molecule and the protonated adduct. However, the UV absorption band of the protonated adduct is shifted by 20 nm from that of the neutral molecule, to 264 nm. When the Raman spectrum is recorded using 266-nm laser excitation, the spectrum of the protonated adduct is resonance enhanced selectively. The study demonstrates that it is possible to detect low levels of weakly acidic sites on the zeolite and to selectively examine chemical changes of small molecules adsorbed on zeolites by using UV resonance Raman spectroscopy.

Li et al. (40), using UV Raman spectroscopy, investigated the formation of coke during the methanol conversion to olefins on different zeolites, including ZSM-5, USY, and SAPO-34. The spectra show that the surface methoxyl species are produced when methanol is introduced into USY, ZSM-5, and SAPO-34 zeolites even at room temperature, but different coke species are formed in these zeolites. Aromatic and polyaromatic

species are easily formed in USY, polyolefinic and monoaromatic species are dominant in ZSM-5, while only olefin and polyolefin species are formed in SAPO-34. The differences of coke formation in ZSM-5, USY, and SAPO-34 are attributed to the different pore structures of the three zeolites.

Chua and Stair (41) designed a fluidized-bed catalytic reactor for UV Raman measurements for eliminating interference from thermal or photochemical decomposition products. This is demonstrated by the spectra for naphthalene adsorbed in H-USY shown in Fig. 45. The spectrum labeled naphthalene is recorded from the neat solid. The spectra labeled stationary, spin, and fluidized bed are recorded from naphthalene adsorbed in an ultrastable Y zeolite when the sample pellet is stationary, spinning, and fluidized powder, respectively. The Raman shifts for peaks from neat naphthalene measured using UV excitation compare well with those reported using visible radiation, showing several distinct Raman peaks. The spectrum measured from the stationary sample exhibits only a small peak at 1625 cm^{-1}, attributed to coke species. The band at 1620 cm^{-1} and a broad band from 1300 to 1550 cm^{-1} seen in the spectra recorded from the spinning sample are also signature coke peaks. The spectrum measured using the fluidized bed method clearly shows that the dominant peaks are those of the undecomposed molecular adsorbate. The small shifts in peak position from the spectrum of neat naphthalene are similar to shifts

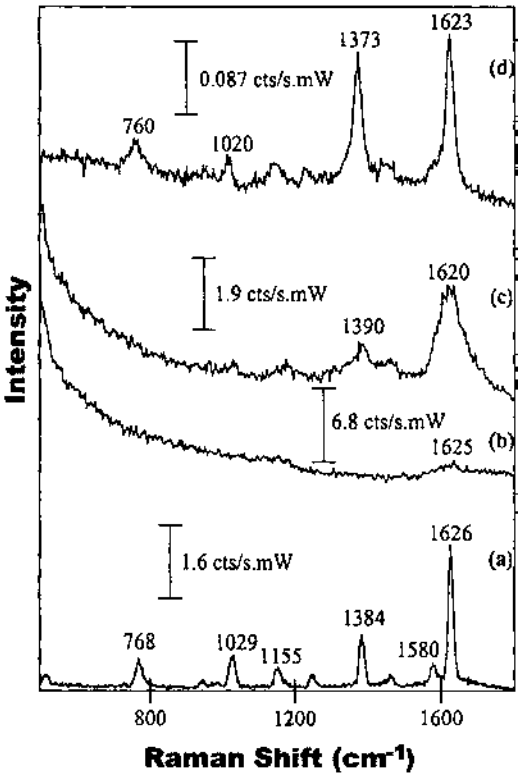

Fig. 45 (a) Spectrum of naphthalene recorded on a spinning disk. Laser power, 0.2 mW. Collection time, 1000 s. (b) Spectrum of naphthalene/H-USY recorded on a stationary disk. 0.3 mW; 300 s. (c) Spectrum of naphthalene/H-USY recorded on a spinning disk. 0.3 mW; 600 s. (d) Spectrum of naphthalene/H-USY recorded using the fluidized-bed apparatus. 1.5 mW; 3600 s. (From Ref. 41.)

observed for spectra from naphthalene in solution and suggest that the zeolite acts something like a solvent for adsorbed naphthalene. Thus, the authors suggest that the fluidized-bed method is a major step forward for in situ catalytic reaction measurements using UV Raman spectroscopy.

VI. SUMMARY AND PROSPECTS

The use of vibrational spectroscopies, mainly IR and Raman, for zeolite characterization was highlighted in this contribution, including the framework and extraframework vibrations, nature of sites in zeolites probed by adsorbed molecules, mechanisms of reactions on zeolite surfaces, and host–guest chemistry within zeolite spaces. It was also shown how UV Raman spectroscopy can be used for identifying transition metals in the framework of zeolites and microporous materials. These examples studied by vibrational spectroscopies provide important information on structure and dynamics of zeolites and zeolite–adsorbate systems, leading to an improved understanding of zeolites and intrazeolite chemistry.

Due to rapid developments in zeolite chemistry, many opportunities are provided for the fundamental progress for vibrational spectroscopies to further enhance our understanding of zeolite chemistry. Several prospects are briefly given as follows.

1. As the application of zeolites depends on the ability to synthesize high-quality zeolites and to characterize zeolites and zeolite-based materials at the atomic level, in situ spectroscopic characterizations of the synthesis precedure of zeolites should be greatly improved. Also, in situ detection of the detailed changes of the structure and sites of zeolites during their use in adsorption, reaction, deactivation, and aging processes should receive more attention.
2. Much can be learned from the interplay between experimental research and computer-assisted calculations and modeling. For example, in the assignment of vibrational bands arising from zeolite units, it is possible by theoretical simulation to obtain the key parameters that affect the vibrational modes of a unit in zeolite. Thus, it is possible to direct the synthesis process of zeolite.
3. Knowledge of zeolite chemistry will be improved significantly by the systematic application of vibrational spectroscopies and other in situ techniques, such as NMR, EPR, and UV-vis spectroscopy. More sensitive and selective spectroscopic techniques are expected to differentiate the nature of sites in and on zeolites. Development of new vibrational spectroscopic techniques is also expected for identifying the fine strutures of zeolites, including the pore structures and defect sites.

ACKNOWLEDGMENTS

We thank Bo Han and Jun Chen for their assistance in preparing the manuscript. In particular, Bo Han reviewed the most references of Raman studies and made a rough draft for the part of Raman characterization of microporous materials.

REFERENCES

1. A Zecchina, C Otero Areán. Chem Soc Rev 25:187–198, 1996.
2. H Knözinger, S Huber. J Chem Soc Faraday Trans 94:2047–2059, 1998.

3. JW Ward. In JA Rabo, ed. Zeolite Chemistry and Catalysis. ACS Monograph No. 171, Washington DC, 1976.
4. H Förster. In JE Davies, ed. Spectroscopic and Computational Studies of Supramolecular Systems. Dordrecht: Kluwer Academic Publishers, 1992.
5. C Otero Areán. Comm Inorg Chem 22:241–273, 2000.
6. HG Karge, M Hunger, HK Beyer. In: J Weitkamp, L Puppe, ed. Catalysis and Zeolites: Fundamentals and Applications. New York: Springer-Verlag, 1999, p 200.
7. JR Ferraro, K Nakamoto. Introduction to Raman Spectroscopy. New York: Academic Press, 1994.
8. I Kiricsi, G Gasi, H Foerster, P Fejes. Acta Phys Chem Szeged 33:69, 1987.
9. W Nicholas Delgass, GL Haller, R Kellerman, JH Lunsford. Spectroscopy in Heterogeneous Catalysis. New York: Academic Press, 1979.
10. LM Kustov, VY Borovkov, VB Kazansky. J Catal 72:149–159, 1981.
11. VB Kazansky. Stud Surf Sci Catal 65:117–131, 1991.
12. P Kubelka, F Munk. Z Teck Phys 12:593, 1931.
13. P Kubelka. J Opt Soc Am 38:448, 1948.
14. AT Bell. In: JT Yates Jr, TE Madey, ed. Vibrational Spectroscopy of Molecules on Surfaces. New York: Plenum Press, 1987, p 105.
15. MFM Post, T Huizinga, CA Emeis, JM Nanne, WHJ Stork. J Catal 72:365–372, 1981.
16. J Phillippaerts, EF Vasant, YA Yan. Stud Surf Sci Catal 46:555–566, 1989.
17. DH Sullivan, WC Conner, MP Harold. Appl Spectrosc 46:811–818, 1992.
18. DC calabro, EW Valyocsik, FX Ryan. Micropor Mater 7:243–259, 1996.
19. PPHJM Knops-Gerrits, XY Li, NT Yu, PA Jacobs. Raman study of the building units in the zeolite structure. Proceedings of 13th International Zeolite Conference, Montpellier, 2001, A-12-P10, and references cited therein.
20. G Mestl, P Ruiz, B Delmon, H Knözinger. J Phys Chem 98:11269–11275, 1994; 98:11276–11282, 1994; 98:11283–11292, 1994.
21. PP Knops-Gerrits, PA Jacobs, A Fukuoka, M Ichikawa, F Faglioni, WA Goddard III. J Mol Cat A Chem 166:3–13, 2001.
22. PK Dutta, DC Shieh, M Puri. J Phys Chem 91:2332–2336, 1987.
23. C Li, G Xiong, Q Xin, J Liu, P Ying, Z Feng, J Li, W Yang, Y Wang, G Wang, X Liu, M Lin, X Wang, E Min. Angew Chem Int Ed 38:2220–2222, 1999.
24. G Xiong, C Li, HY Li, Q Xin, ZC Feng. Chem Commun 677–678, 2000.
25. C Li, G Xiong, J Liu, P Ying, Q Xin, Z Feng. J Phys Chem B 105:2993–2997, 2001.
26. Y Yu, G Xiong, C Li, FS Xiao. J Catal 194:487–490, 2000.
27. K Nakamoto. Infrared and Raman Spectra of Inorganic and Coordination Compounds. New York: John Wiley & Sons, 1978.
28. A Compion. In: JT Yates Jr, TE Madey, ed. Vibrational Spectroscopy of Molecules on Surfaces. New York: Plenum Press, 1987, p 345.
29. JM Stencel. Raman Spectroscopy for Catalysis. New York: Van Nostrand Reinhold, 1990.
30. DJ Gardiner. P. 1, In: DJ Gardiner, PR Graves, ed. Practical Raman Spectroscopy. New York: Springer-Verlag, 1989.
31. IR Beattie. Chem Soc Rev 4:107–154, 1975.
32. TA Egerton, AH Hardin. Catal Rev Sci Eng 11:71–116, 1975.
33. GW Chantry, HA Gebbie, C Helsum. Nature 203:1052–1053, 1964.
34. DB Chase. Mikrochim Acta 111:81–91, 1987.
35. C Li, PC Stair. Stud Surf Sci Catal 105A:599–606, 1997.
36. PC Stair, C Li. J Vac Sci Technol A 15:1697–1684, 1997.
37. C Li, PC Stair. Catal Today 33:353–360, 1997.
38. C Li, PC Stair, Stud Surf Sci Catal 101:881–890, 1996.
39. C Li, PC Stair. Catal Lett 36:119–123, 1996.
40. J Li, G Xiong, Z Feng, Z Liu, Q Xin, C Li. Micropor Mesopor Mater 39:275–280, 2000.

41. YT Chua, PC Stair. J Catal 196:66–72, 2000.
42. Y Yu, G Xiong, C Li, F Xiao. Micropor Mesopor Mater 46:23–34, 2001.
43. G Xiong, Y Yu, F Xiao, C Li. Micropor Mesopor Mater 42:317–323, 2001.
44. J Klinowski. Annu Rev Mater Sci 18:189–218, 1988.
45. J Klinowski. Chem Rev 91:1459–1479, 1997.
46. MW Anderson, JR Agger, DP Luigi, AK Baggaley, J Rocha. Phys Chem Chem Phys 1:2287–2292, 1999.
47. EM Glanigen. In: J Rabo, ed. Zeolite Chemistry and Catalysis. ACS Monograph Ser. 171:93, 1976.
48. EM Flanigen, H Khatami, HA Seymenski. In: EM Flanigen, LB Sands, eds. Advances in Chemistry Series 101, American Chemical Society, Washington, DC, 1971, pp 201–228.
49. JC Jansen, FJ Van der Gaag, H Van Bekkum. Zeolites 4:369–372, 1984.
50. PA Jacobs, HK Beyer, J Valyon. Zeolites 1:161–168, 1981.
51. G Coudurier, C Naccache, JC Vedrine. J Chem Soc Chem Commun 1413–1415, 1982.
52. DM Bibby, LA Aldridge, NB Milestone. J Catal 72:373–374, 1981.
53. JP Dong, YJ Sun, YC Long. Chemistry Letters 6:516–517, 2001.
54. W Mozgawa. J Mol Struct 596:129–137, 2001.
55. M Handke, M Sitarz, W Mozgawa. J Mol Struct 450:229–238, 1998.
56. E. Geidel. PhD dissertion, University of Leipzig, 1989.
57. E Geidel, H Boehlig, Ch Peuker, W Pilz. Stud Surf Sci Catal 65:511–520, 1991.
58. RA van Santen. DL Vogel. Adv Solid State Chem 1:151–224, 1988.
59. C Bremard, D Bougeard. Adv Mater 7:10–25, 1995.
60. PJ Jacobs, J Datka, P Geerlings, W Mortier. J Phys Chem 89:3483, 1985.
61. SM Campbell, DM Bibby, JM Coddington, RF Howe. J Catal 161:350–358, 1996.
62. MD Baker, GA Ozin, J Godber. Catal Rev Sci Eng 27:591–651, 1985.
63. GA Ozin, MD Baker, J Godber, S Wu. J Am Chem Soc 107:3033–3043, 1985.
64. H Esemann, H Förster, E Geidel, K Krause. Micropor Mater 6:321–329, 1996.
65. VK Kondratov, LF Lopatova, VGV Vykhristyuk. Russ J Phys Chem 53:1796, 1979.
66. E Broclawik, J Datka, B Gil, P Kozyra. Phys Chem Chem Phys 2:401–405, 2000.
67. JW Ward. In: JA Rabo, ed. Zeolite Chemistry and Catalysis. Washington, DC: Am Chem Soc, Mon 171, p 118.
68. HG Karge. ACS Symp Ser 40:584, 1977.
69. JW Ward. J Phys Chem 72:4211–4223, 1968.
70. JW Ward. J Catal 22:237–244, 1971.
71. CO Arean, GT Palomino, A Zecchina, G Spoto, S Bordiga, P Roy. Phys Chem Chem Phys 1: 4139–4140, 1999.
72. PA Jacobs. Catal Rev Sci Eng 24:415–440, 1982.
73. PA Jacobs, WJ Mortier. Zeolites 2:226–230, 1982.
74. H Stach, I Girnus, J Jänchen, E Löffler, B Parlitz, B Zibrowius. Recent Research Reports of the 9th International Zeolite Conference, Montreal, 1991, Report No. RP 142.
75. KH Schnabel, R Fricke, I Girnus, J Jahn, E Löffler, B Parlitz, C Peuker. J Chem Soc Faraday Trans 87:3569–3574, 1991.
76. LM Kustov, VB Kazansky, P Ratnasamy. Zeolites 7:79–83, 1987.
77. I Mirsojew, S Ernst, J Weitkamp, H Knözinger. Catal Lett 24:235–248, 1994.
78. CTW Chu, CD Chang. J Phys Chem 89:1569–1571, 1985.
79. MTM Post, T Huizinga, CA Emeis, JM Nanne, WHJ Stork. In: HG Karge, J. Weitkamp, eds. Zeolites as Catalysts, Sorbents and Detergent Builders: Applications and Innovations. Amsterdam: Elsevier, 1989, p 365.
80. LM Kustov, VB Kazansky, S Beran, L Kubelková, P Jiru. J Phys Chem 91:5247–5251, 1987.
81. L Kubelková, S Beran, JA Lercher. Zeolites 9:539–543, 1989.
82. N Echoufi, P Gélin. J Chem Soc Faraday Trans 88:1067–1073, 1992.
83. B Zibrowius, E. Löffler, M Hunger. Zeolites 12:167–174, 1992.
84. U Lohse, E Löffler, K Kosche, J Jänchen, B Parlitz. Zeolites 13:549–556, 1993.

85. J Chen, PA Wright, JM Thomas, S Natarajan, L Marchese, SM Bradley, G Sankar, CRA Catlow, PL Gai-Boyes, RP Towsend, CM Lok. J Phys Chem 98:10216–10224, 1994.
86. M Briend, MJ Peltre, A Lamy, PP Man, D Barthomeuf. J Catal 138:90–100, 1992.
87. U Lohse, B Parlitz, B Altrichter, K Janche, E Schreier, F Vogt. J Chem Soc Faraday Trans 91: 1155–1161, 1995.
88. B Onida, F Geobaldo, F Testa, F Crea, E Garrone. Micropor Mesopor Mater 30:119–127, 1999.
89. Kosslick H, Landmesser H, Fricke R. J Chem Soc Faraday Trans 93:1849–1854, 1997.
90. M Trombettaa, G Busca, M Lenarda, L Storaro, M Pavan. Appl Catal A General 182:225–235, 1999.
91. T Mori, Y Kuroda, Y Yoshikawa, M Nagao, S Kittaka. Langmuir 18:1595–1603, 2002.
92. GL Woolery, LB Alemany, RM Dessau, AW Chester. Zeolites 6:14–16, 1986.
93. D Barthomeuf. Stud Surf Sci Catal 5:55–64, 1980.
94. WJ Mortier. J Catal 55:138–145, 1978.
95. PA Jacobs, WJ Mortier, JB Uytterhoeven. Inorg Nucl Chem 40:1919, 1978.
96. VA Tuan. PhD dissertation, Free University of Berlin, 1994.
97. VB Kazansky, LM Kustov, VY Borovkov. Zeolites 3:77–81, 1983.
98. B Staudte, M Hunger, M Nimz. Zeolites 11:837–841, 1991.
99. K Beck, H Pfeifer, B Staudte. J Chem Soc Faraday Trans 89:3995–3998, 1993.
100. WPJH Jacobs, H Jobic, JHMC Van Wolput, RA van Santen. Zeolites 12:315–319, 1992.
101. J Dwyer. Stud Surf Sci Catal 37:333–354, 1987.
102. J Dwyer. NATO ASI Ser, Ser C 352:303 (1992); 352:321 (1992).
103. RA van Santen. Stud Surf Sci Catal 85:273–294, 1994.
104. WE Farneth, RJ Gorte. Chem Rev 95:615–635, 1995.
105. JA Lercher, C Gründling, G Eder-Mirth. Catal Today 27:353–376, 1996.
106. D Barthomeuf. Catal Rev Sci Eng 38:521–612, 1996.
107. JA Martens, W Souverijns, W Van Rhijn, PA Jacobs. In: G Ertl, H Knönzinger, J Weitkamp, eds. Handbook of Heterogeneous Catalysis. Weinheim: VCH, 1997, p 324.
108. S Coluccia, L Marchese, G Martra. Micropor Mesopor Mater 30:43–56, 1999.
109. S Coluccia, L Marchese, G Martra. In: A Masakazu, ed. Photofunctional Zeolites. New York: Nova Science Publishers, 2000, pp. 39–74.
110. D Barthomeuf. Stud Surf Sci Catal 65:157–170, 1991.
111. D Barthomeuf. In: J Fraissard, L Petrakis, eds. Acidity and Basicity of Solids. Dordrecht: Kluwer, 1994, p 181.
112. JC Lavalley. Catal Today 27:377–401, 1996.
113. R Szostak. Stud Surf Sci Catal 58:13, 1991.
114. JW Ward. J Catal 10:34–46, 1968.
115. HG Karge. In: E. G. Derouane, et al. eds. Zeolite Micropous Solids: Synthesis, Structure and Reactivity. Dordrecht: Kluwer, 1992, p 273.
116. G Müller, G Eder-Mirth, H Kessler, JA Lercher. J Phys Chem 99:12327–12331, 1995.
117. J Datka, B Gil. J Mol Structure 596:41–45, 2001.
118. J Datka, B Gil, T Domagala, K Gora-Marek. Micropor Mesopor Mater 47:61–66, 2001.
119. F Lonyi, J Valyon. Thermochim Acta 373:53–57, 2001.
120. R Barthos, F Lonyi, G Onyestyak, J Valyon. J Phys Chem B 104:7311–7319, 2000.
121. WM Zhang, PG Smirniotis, M Gangoda, RN Bose. J Phys Chem B 104:4122–4129, 2000.
122. C Peireira, RJ Gorte. Appl Catal A General 90:145–157, 1992.
123. W Liu, Y Xu. J Catal 185:386–392, 1999.
124. RB Borade, A Clearfield. J Phys Chem 96:6729–6737, 1992.
125. N Echoufi, P Gelin. Catal Lett 40:249–252, 1996.
126. P Tynjala, TT Pakkanen. J Mol Catal A Chemical 110:153–161, 1996.
127. H Kosslick, G Lischke, G Walther, W Storek, A Martin, R Fricke. Micropor Mater 9:13–33, 1997.
128. B Chakraborty, B Viswanathan. Catal Today 49:253–260, 1999.

129. D Meloni, S Laforge, D Martin, M Guisnet, E Rombi, V Solinas. Appl Catal A General 215:55–66, 2001.
130. WM Hua, YH Yue, Z Gao. J Mol Catal A Chemical 170:195–202, 2001.
131. F Moreau, P Ayrault, NS Gnep, S Lacombe, E Merlen, M Guisnet. Micropor Mesopor Mater 51:211–221, 2002.
132. MA Makarova, F Ojo, K Karim, M Hunger, J Dwyer. J Phys Chem 98:3619–3623, 1994.
133. S Jolly, J Saussey, JC Lavalley. J Mol Catal 86:401–421, 1994.
134. C Morterra, G Cerrato, G Meligrana. Langmuir 17:7053–7060, 2001.
135. H Knözinger, H Krietenbrink. J Chem Soc Faraday Trans I 71:2421–2430, 1975.
136. L Kulbelkova, J Kotrla, J Florian. J Phys Chem 99:10285–10293, 1995.
137. R Anquetil, J Saussey, JC Lavalley. Phys Chem Chem Phys 1:555–560, 1999.
138. C Paze, GT Palomino, A Zecchina. Catal Lett 60:139–143, 1999.
139. T Armaroli, M Bevilacqua, M Trombetta, F. Miella, AG Alejandre, J Ramírez, B Notari, RJ Willey, G Busca. Appl Catal A General 216:59–71.
140. A Corma. Chem Rev 95:559–614, 1995.
141. H Knözinger. In: K Tanabe, H Hattori, T Yamaguchi, T Tanaka, eds. Acid-Base Catalysis. Weinheim: VCH, 1989, p 147.
142. I Mirsojew, S Ernst, J Weitkamp, H Knözinger. Catal Lett 24:235–248, 1994.
143. F Wakabayashi, JN Kondo, K Domen, C Hirose. J Phys Chem 99:10573–10580, 1995.
144. M Sigl, S Ernst, J Weitkamp, H Knözinger. Catal Lett 45:27–33, 1997.
145. B Onida, F Geobaldo, F Testa, F Crea, E Garrone. Micropor Mesopor Mater 30:119–127, 1999.
146. L Pasqua, F Testa, R Aiello. Stud Surf Sci Catal 117:317–324, 1998.
147. O Cairon, K Thomas, T Chevreau. Micropor Mesopor Mater 46:327–340, 2001.
148. T Mori, Y Kuroda, Y Yoshikawa, M Nagao, S Kittaka. Langmuir 18:1595–1603, 2002.
149. A Zecchina, S Bordiga, C Lamberti, G Spoto, L Carnelli, C Otero Arean. J Phys Chem 98: 9577–9582, 1994.
150. M Trombetta, G Busca, SA Rossini, V Piccoli, U Cornaro. J Catal 168:349–363, 1997.
151. M Trombetta, T Armaroli, AG Alejandre, JR Solis, G Busca. Appl Catal A General 192:125–136, 2000.
152. M Trombetta, AG Alejandre, JR Solis, G Busca. Appl Catal A General 198:81–93, 2000.
153. F Wakabayashi, J Kondo, K Domen, C Hirose. Micropor Mater 8:29–37, 1997.
154. F Geobaldo, C Lamberti, G Ricchiardi, S Bordiga, A Zecchina, GT Palomino, C Otero Arean. J Phys Chem 99:11167–11177, 1995.
155. F Wakabayashi, J Kondo, K Domen, C Hirose. J Phys Chem 100:4154–4159, 1996.
156. A Zecchina, F Geobaldo, C Lamberti, S Bordiga, GT Palomino, C Otero Arean. Catal Lett 42:25–33, 1996.
157. L Marchese, E Gianotti, N Damilano, S Coluccia, JM Thomas. Catal Lett 37:107–111, 1996.
158. M Förster, M Schumann. J Chem Soc Faraday Trans I 85:1149–1158, 1989.
159. P Concepcion-Heydorn, C Jia, D Herein, N Pfander, HG Karge, FC Jentoft. J Mol Catal A Chem 162:227–246, 2000.
160. B Bonelli, B Onida, B Fubini, CO Arean, E Garrone. Langmuir 16:4976–4983, 2000.
161. A Vimont, F Thibault-Starzyk, JC Lavalley. J Phys Chem B 104:286–291, 2000.
162. PA Jacobs, FM Van Cauwelaert, EF Vansant. J Chem Soc Farad Trans I 69:2130, 1973.
163. MM Huang, S Kaliaguine. J Chem Soc Faraday Trans 88:751–758, 1992.
164. D Murphy, P Massiani, R Franck, D Barthomeuf. J Phys Chem 100:6731–6738, 1996.
165. C Binet, A Jadi, J Lamotte, JC Lavalley. J Chem Soc Faraday Trans 92:123–129, 1996.
166. C Yang, J Wang, QH Xu. Micropor Mater 11:261–268, 1997.
167. C Yang, NY He, QH Xu. Stud Surf Sci Catal 125:457–464, 1999.
168. J Liu, P Ying, Q Xin, C Li. Zeolites 19:197–199, 1997.
169. HG Karge, M Laniechi, M Ziolek. J Catal 109:252–262, 1988.
170. EB Uvarova, LM Kustov, VB Kazansky. Stud Surf Sci Catal 94:254–261, 1995.
171. HG Karge, M Ziolek, M Laniecki. Zeolites 7:197–202, 1987.

172. GN Vayssilov, N Rosch. Phys Chem Chem Phys 4:146–148, 2002.
173. M Waqif, AM Mohammed Saad, M Bensitel, J Bachelier, O Saur, JC Lavalley. J Chem Soc Farad Trans 88:2931–2936, 1992.
174. AA Davidov, ML Shepotko, AA Budneva. Kinet Catal 35:272–278, 1994.
175. RA van Santen, GJ Kramer. Chem Rev 95:637–660, 1995.
176. RA van Santen. Catal Today 38:377–390, 1997.
177. D Farcasiu, D Hancu. Catal Lett 53:3–6, 1998.
178. S Kotrel, JH Lunsford, H Knözinger. J Phys Chem B 105:3917–3921, 2001.
179. B Lee, JN Kondo, F Wakabayashi, K Domen. Catal Lett 59:51–54, 1999.
180. JN Kondo, S Liquin, F Wakabayashi, K Domen. Catal Lett 47:129–133, 1997.
181. JN Kondo, L Shao, F Wakabayashi, K Domen. J Phys Chem B 101:9314–9320, 1997.
182. JN Kondo, K Domen, F Wakabayashi. Micropor Mesopor Mater 21:429–437, 1998.
183. JN Kondo, F Wakabayashi, K Domen. Catal Lett 53:215–220, 1998.
184. J Kotrla, D Nachtigallova, V Bosacek, J Novakova. Phys Chem Chem Phys 1:2613–2620, 1999.
185. L Chen, L Wu, Z Xu, T Zhang, D Liang. Catal Lett 35:245–258, 1995.
186. S Natarajan, PA Wright, JM Thomas. J Chem Soc Chem Commun 1861–1862, 1993.
187. HH Mooiweer, KP de Jong, B Kraushaar-Czarnetzki, WHJ Stork, BCH Krutzen. Stud Surf Sci Catal 84:2327–2334, 1994.
188. CL O'Young, RJ Pellet, DG. Casey, JR Ugolini, RA Sawicki. J Catal 151:467–469, 1995.
189. M Guisnet, P Andy, NS Gnep, E Benazzi, C Travers. J Catal 158:551–560, 1996.
190. P Mériaudeau, R Bacaud, L Ngoc Hung, T Anh Vu. J Mol Catal A Chem 110:L177–L179, 1996.
191. G Seo, HS Jeong, SB Hong, US Uh. Catal Lett 36:249–253, 1996.
192. G Seo, MY Kim, JH Kim. Catal Lett 67:207–213, 2000.
193. DW Breck. Zeolite Molecular Sieves. New York: John Wiley & Sons, 1974, p 125.
194. WM Meier, DH Olson, C Baerlocher. Atlas of Zeolite Structure Types, 4th Ed. New York: Elsevier, 1996, p 62.
195. P Ivanov, H Papp. Langmuir 16:7769–7772, 2000.
196. C Pazé, B Sazak, A Zecchina, J Dwyer. J Phys Chem B 103:9978–9986, 1999.
197. B Wichterlová, N Zilkova, E Uvarova, J Cejka, P Sarv, C Paganini, JA Lercher. Appl Catal A General 182:297–308, 1999.
198. G Mirth, J Cejka, JH Lercher. J Catal 139:24–33, 1993.
199. T Terlouw, JP Gilson. Shell Int Res Mij B V EP n° 458 378, 1991.
200. O Marie, F Thibault-Starzyk, P Massiani, JC Lavalley. Role of the various acid sites in MOR on o-xylene conversion: an in situ IR approach. Proceedings of 13th International Zeolite Conference. Montpellier, France, 2001, 12-P-14.
201. F Thibault-Starzyk, A Vimont, JP Gilson. 2D correlation IR spectroscopy of xylene isomerisation on H-MFI zeolite. Proceeding of 13th International Zeolite Conference. Montpellier, France, 2001, 12-O-01.
202. PB Venuto, LA Hamilton, PS Landis. J Catal 5:81–98, 1966; 5:484–493, 1966.
203. C Flego, I Kiricsi, C Perego, G Bellussi. Stud Surf Sci Catal 94:405–412, 1995.
204. C Flego, I Kiricsi, WO Parker, Jr, MG Clerici. Appl Catal A: Gen 124:107–119, 1995.
205. N Arsenova, H Bludau, WO Haag, HG Karge. Micropor Mesopor Mater 23:1–10, 1998.
206. F Geobaldo, G Spoto, S Bordiga, C Lamberti, A Zecchina. J Chem Soc Faraday Trans 93: 1243–1249, 1997.
207. S Bordiga, G Ricchiardi, G Spoto, D Scarano, L Carnelli, A Zecchina, CO Arean. J Chem Soc Faraday Trans 89:1843–1855, 1993.
208. TV Voskoboinikov, B Coq, F Fajula, R Brown, G McDougall, JL Couturier. Micropor Mesopor Mater 24:89–99, 1998.
209. Z Dardas, MG Süer, YH Ma, WR Moser. J Catal 159:204–211, 1996.
210. MG Süer, Z Dardas, YH Ma, WR Moser. J Catal 162:320–326, 1996.
211. H Ishikawa, E Yoda, JN Kondo, F Wakabayashi, K Domen. J Phys Chem B 103:5681–5686, 1999.

212. VA Veefkind, JA Lercher. Appl Catal A General 181:245–255, 1999.
213. GA Fois, G Ricchiardi, S Bordiga, C Busco, L Dalloro, G Spano, A Zecchina. The Beckmann rearrangement catalyzed by silicalite: a spectroscopic and computational study. Proceeding of 13th International Zeolite Conference. Montpellier, France, 2001, 15-O-05.
214. ST King, JM Garces. J Catal 104:59–70, 1987.
215. AE Palomares, G Eder-Mirth, JA Lercher, J Catal 168:442–449, 1997.
216. AE Palomares, G Eder-Mirth, M Rep, JA Lercher. J Catal 180:56–65, 1998.
217. M Iwamoto, H Yashiro. Catal Today 22:5–18, 1994.
218. VA Matyshak, AN Il'ichev, AA Ukharshy, VN Korchak. J Catal 171:245–254, 1997.
219. B Ganemi, E Björnbom, J Paul. Appl Catal B 17:293–311, 1998.
220. MV Kondurn, SSC Chuang. J Phys Chem B 103:5802–5813, 1999.
221. X Feng, WK Hall. Catal Lett 41:45–46, 1996.
222. HY Chen, WMH Sachtler. Catal Today 42:73–83, 1998.
223. HY Chen, T Voskoboinikov, WMH Sachtler. Catal Today 54:483–494, 1999.
224. P Marturano, L Drozdová, A Kogelbauer, R Prins. J Catal 192:236–247, 2000.
225. LJ Lobree, IC Hwang, JA Reimer, AT Bell. Catal Lett 63:233–240, 1999.
226. RQ Long, RT Yang. J. Catal 194:80–90, 2000.
227. Q Sun, Z Gao, H Chen, WMH Sachtler. J Catal 201:89–99, 2001.
228. F Heinrich, E Löffler, W Grünert. Selective catalytic reduction of NO over Fe zeolites—catalytic and in-situ—DRIFTS studies. Proceeding of 13th International Zeolite Conference. Montpellier, France, 2001, 30-P-27.
229. J Eng, CH Bartholomew J Catal 171:27–44, 1997.
230. T Gerlach, FW Schütze, M Baerns. J Catal 185:131–137, 1999.
231. S Chatterjee, HL Greene. Appl Catal A General 98:139–158, 1993.
232. I Hannus, Z Kónya, T Kollár, Y Kiyozumi, F Mizukami, P Lentz, JB Nagy, I Kiricsi. Stud Surf Sci Catal 125:245–252, 1999.
233. JF Haw, JB Nicholas, T Xu, LW Beck, DB Ferguson. Acc Chem Res 29:259–267, 1996 and references cited therein.
234. AG Stepanov, KI Zamaraev, JM Thomas. Catal Lett 13:407–422, 1992.
235. AG Stepanov, MV Luzgin, VN Romannikov, VN Sidelnikov, EA Paukshtis. J Catal 178:466–477, 1998.
236. G Spoto, S Bordiga, G Ricchiardi, D Scarano, A Zecchina, E Borello. J Chem Soc Faraday Trans 90:2827–2835, 1994.
237. JN Kondo, F Wakabayashi, K Domen. J Phys Chem B 102:2259–2262, 1998.
238. JN Kondo, H Ishikawa, E Yoda, F Wakabayashi, K Domen. J Phys Chem B 103:8538–8543, 1999.
239. VB Kazansky. Accounts Chem Res 24:379–383, 1991.
240. GA Olah, GK Surya Prakash, J Sommer. Superacids. New York: Wiley-Interscience, 1985.
241. JF Haw, BR Richadson, IS Oshiro, ND Lazo, AJ Speed. J Am Chem Soc 111:2052–2058, 1989.
242. FG Oliver, FJ Munson, JF Haw. J Phys Chem 96:8106–8111, 1992.
243. AV Demidov, AA Davydov. Mater Chem Phys 39:13–20, 1994.
244. I Kirisci, H Förster, G Tasi, JB Nagy. Chem Rev 99:2085–2114, 1999 and references cited therein.
245. S Yang, JN Kondo, K Domen. Stud Surf Sci Catal 135:1870–1878, 2001.
246. S Yang, JN Kondo, K Domen. Chem Commun 2008–2009, 2001.
247. S Yang, JN Kondo, K Domen. J Phys Chem B 105:7878–7881, 2001.
248. S Yang, JN. Kondo, K Domen. Catal Today 73:113–125, 2002.
249. S Yang, JN Kondo, K Domen. Catal Surv Jpn 5:139–149, 2002.
250. BJ Adelman, T Beutel, GD Lei, WMH Sachtler. J Catal 158:327–335, 1996.
251. J Valyon, WK Hall. J Phys Chem 97:1204–1212, 1993.
252. T Cheung, PK Bhargava, M Hobday, K Foger. J Catal 158:301–310, 1996.
253. G Spoto, S Zecchina, S Bordiga, G Ricchiardi, G Marta, G Leofanti, G Petrini. Appl Catal 3: 151–172, 1994.

254. AW Aylor, SC Larsen, JA Reimer, AT Bell. J Catal 157:592–602, 1995.
255. E Giamello, D Murphy, G Magnacca, C Morterra, Y Shioya, T Nomura, M Anpo. J Catal 136:510–520, 1992.
256. M Iwamoto, H Mizuno, WX Zhang, Y Mine, H Furukawa, S Kagawa. J Phys Chem 96:9360–9366, 1992.
257. TE Hoost, KA Laframboise, K Otto. Catal Lett 33:105–116, 1995.
258. K Hadjiivanov, D Klissurski, G Ramis, G Busca. Appl Catal B 7:251–267, 1996.
259. K Hadjiivanov, J Saussey, JL Freysz, JC Lavalley. Catal Lett 52:103–108, 1998.
260. N Hayes, RW Joyner, ES Shapiro. Appl Catal B 8:343–363, 1996.
261. Y Li, TL Slager, JN Armor. J Catal 150:388–399, 1994.
262. J Weitkamp. In: R von Ballmoos, JB Higgins, MMJ Treacy, eds. Proceedings from the 9th International Zeolite Conference. Boston: Butterworth-Heinemann, 1:13, 1993.
263. C Brémard. Coord Chem Rev 178–180:1647–1677, 1998.
264. YN Huang, JH Leech, EA Havenga, RR Poissant. Micropor Mesopor Mater 48:95–102, 2001.
265. AI Serykh, OP Tkachenko, VY Borovkov, VB Kazansky, M Beneke, NI Jaeger, G Schulz-Ekloff. Phys Chem Chem Phys 2:5647–5652, 2000.
266. G Larsen, GL Haller. Catal Lett 3:103–116, 1989.
267. BL Mojet, JT Miller, C Koningsberger. J Phys Chem B 103:2724–2734, 1999.
268. VB Kazansky, VY Borovkov, N Sokolova, NI Jaeger, G Schulz-Ekloff. Catal Lett 23:263–269, 1994.
269. T Rades, VY Borovkov, VB Kazansky, M Polisset-Thfoin, J Fraissard. J Phys Chem 100: 16238–16241, 1996.
270. VB Kazansky, VY Borovkov, AI Serykh. Catal Lett 49:35–41, 1997.
271. JH Sinfelt In: J. R. Anderson, M. Boudart, eds. Catalysis: Science and Technology. Berlin: Springer-Verlag, 1:257, 1981.
272. OP Tkachenko, ES Shpiro, NI Jaeger, R Lamber, G Schulz-Ekloff, H Landmesser. Catal Lett 23:251–262, 1994.
273. LL Sheu, H Knözinger, WMH Sachtler. J Am Chem Soc 111:8125–8131, 1989.
274. ZC Zhang, TT Wong, WMH Sachtler. J Catal 128:13–22, 1991.
275. BL Mojet, MJ Kappers, JC Muijsers, JW Niemantsverdriet, JT Miller, FS Modica, DC Koningsberger. Stud Surf Sci Catal 84:909–916, 1994.
276. JGC Shen, AM Liu, T Tanaka, M Ichikawa. J Phys Chem B 102:7782–7792, 1998.
277. JGC Shen. J Phys Chem B 105:2336–2342, 2001.
278. G Spoto, S Bordiga, D Scarano, A Zecchina. Catal Lett 13:39–44, 1992.
279. JH Lunsford, PJ Hutta, MJ Lin, KA Windhorst. Inorg Chem 17:606–610, 1978.
280. GA Ozin, S Ozkar. J Phys Chem 94:7556, 1990.
281. S Kawi, JR Chang, BC Gates. J Am Chem Soc 115:4830–4843, 1993.
282. TM Salama, R Ohnishi, M Ichikawa. Stud Surf Sci Catal 105:1571–1578, 1997.
283. GD Stucky, JE Macdougall. Science 247:669–678, 1990.
284. N Herron. J Inclusion Phenom Mol Recognit Chem 21:283–298, 1995.
285. G Telbiz, A Shwets, V Gunko, J Stoch, G Tamulajtis, N Kukhtarev. Stud Surf Sci Catal 84:1099–1106 Part A–C, 1994.
286. VN Bogomolov, VV Poborchii, SV Kholodkevich, SI Shagin, J Phys C Solid State Phys 18:L313–L317, 1985.
287. VN Bogomolov, VV Poborchii, SV Kholodkevich. JETP Lett 42:517, 1985.
288. VN Bogomolov, AN Efimov, MS Ivanova, VV Poborchii, SG Romanov, YuI Smolin, YuF Shepelev. Sov Phys Solid State 34:916, 1992.
289. VV Poborchii. J Phys Chem Solids 55:737–743, 1994.
290. A Goldbach, L Iton, M Grimsditch, ML Soboungi. J Am Chem Soc 118:2004–2007, 1996.
291. A Goldbach, M Grimsditch, L Iton, ML Saboungi. J Phys Chem B 101:330–334, 1997.
292. W Zhang, J Shi, H Chen, Z Hua, D Yan. Chem. Mater. 13:648–654, 2001.
293. X Li, C Shao, S Qiu, F Xiao, W Zheng, P Ying, O Terasaki. Micropor Mesopor Mater 40:263–269, 2000.

294. J He, Y Ba, CI Batcliffe, JA Ripmeester, DD Klug, JS Tse, KF Preston. J Am Chem Soc 120:10697–10705, 1998.
295. L frunza, H Kosslick, H Landmesser, E Höft, R fricke. J Mol Catal A Chem 123:179–187, 1997.
296. MJ Sabater, AB Corma, A Domenech, V Fornés, H García. Chem Commun 1285–1286, 1997.
297. SB Ogunwumi, T Bei. Chem Commun 901–902, 1997.
298. GJ Kim, JH Shim. Catal Lett 63:205–212, 1999.
299. PP Knops-Gerrits, DE De Vos, EJP Feijen, PA Jacobs. Micropor Mater 8:3–17, 1997.
300. G Mestl, H Knözinger. In: G Ertl, H Knözinger, J Weitkamp, ed. Handbook of Heterogeneous Catalysis, Vol 2. Weinheim: Wiley, 1997, pp 539–574.
301. EM Flanigen, H Khatami, HA Szymanski. Adv Chem Ser 10:201, 1971.
302. AJM de Man, BNH van Beest, M Leslie, RA van Santen. J Phys Chem 94:2524–2534, 1990.
303. A Jentys, JA Lercher. In: H van Bekkum, EM Flangien, PA Jacobs, JC Jansen, ed. Introduction to Zeolite Science and Practice. Amsterdam: Elsevier, 2001, pp 345–386.
304. PK Dutta, DC Shieh, M Puri. Zeolites 8:306–309, 1988.
305. PK Dutta, KM Rao, JY Park. J Phys Chem 95:6654–6656, 1991.
306. PK Dutta, DC Shieh. J Phys Chem 90:2331–2334, 1986.
307. CL Angel. J Phys Chem 77:222–227, 1973.
308. PK Dutta, J Twu. J Phys Chem 95:2498–2501, 1991.
309. PK Dutta, B Del Barco. J Chem Soc Chem Commun 1297–1299, 1985.
310. PK Dutta, B Del Barco. J Phys Chem 92:354–357, 1988.
311. PK Dutta, B Del Barco. J Phys Chem 89:1861–1965, 1985.
312. PK Dutta, M Puri. J Phys Chem 91:4329–4333, 1987.
313. KT No, DH Bae, MS John. J Phys Chem 90:1772–1780, 1986.
314. C Brémard, M Le Maire. J Phys Chem 97:9695–9702, 1993.
315. D Scarano, A Zecchina, S Bordiga, F Geobaldo, G Spoto, G Petrini, G Leofanti, M Padovan, G Tozzola. J Chem Soc Faraday Trans 89:4123–4130, 1993.
316. A Zecchina, S Bordiga, G Spoto, D Scarano, G Petrini, G Leofanti, M Padovan, CO Arean. J Chem Soc Faraday Trans 88:2959–2969, 1992.
317. AM Prakash, L Kevan. J Am Chem Soc 120:13148–13155, 1998.
318. H Kosslick, VA Tuan, R Fricke, C Peuker, W Pilz, W Storek. J Phys Chem 97:5678–5684, 1993.
319. AJM de Man, J Sauer. J Phys Chem 100:5025–5034, 1996.
320. MA Camblor, A Corma, J Perez-Pariente. J Chem Soc Chem Commun 557–559, 1993.
321. G Deo, AM Turek, IE Wachs, DRC Huybrechts, PA Jacobs. Zeolites 13:365–373, 1993.
322. J Twu, PK Dutta, CT Kresge. J Phys Chem 95:5267–5271, 1991.
323. F Roozeboom, HE Robson, SS Chan. Zeolites 3:321–328, 1983.
324. PK Dutta, KM Rao, JY Park. Langmuir 8:722–726, 1992.
325. BD McNicol, GT Pott, KR Loos, J Phys Chem 76:3388–3390, 1972.
326. CL Angell, WH Flank. ACS Symp Ser 40:194–206, 1977.
327. DW Breck. Zeolite Molecular Sieves. New York: John Wiley & Sons, 1976, pp 45–59.
328. J Twu, PK Dutta, CT Kresge. Zeolites 11:672–679, 1991.
329. H Boulet, C Brémard, M Le Marie. J Raman Spectrosc 23:421–423, 1992.
330. G Schrimpf, M Schlenkrich, J Brickmann, P Bopp. J Phys Chem 96:7404–7410, 1992.
331. JL Lievens, WJ Mortier, KJ Chao, J Phys Chem Solids 53:1163–1169, 1992.
332. KS Smirnov, D Bougeard. J Raman Spectrosc 24:255–257, 1993.
333. KS Smirnov, D Bougeard. J Phys Chem 97:9434–9440, 1993.
334. Y Huang. J Am Chem Soc 118:7233–7234, 1996.
335. Y Huang, Z Jiang. Micropor Mater 12:341–345, 1997.
336. Y Huang, EA Havenga. Langmuir 15:6605–6608, 1999.
337. Y Huang, P Qiu. Langmuir 15:1591–1593, 1999.
338. Y Huang, EA Havenga. J Phys Chem B 104:5084–5089, 2000.

339. Y Huang, EA Havenga. Chem Mater 13:738–746, 2001.
340. YN Huang, EA Havenga. Micropor Mesopor Mater 42:77–88, 2001.
341. S Ashtekar, AS McLeod, MD Mantle, PJ Barrie, LF Gladden, JJ Hastings. J Phys Chem B 104:5281–5287, 2000.
342. PC Stair. Curr Opin Solid State Mater Sci 5:365–369, 2001.
343. C Brémard, G Buntinx, G Ginestet. J Mol Struct 410:379–382, 1997.
344. C Brémard, G Buntinx, G Coustillier, G Ginestet. J Mol Struct 410:81–84, 1997.
345. A Moissette, I Gener, C Brémard. J Phys Chem B 105:5647–5656, 2001.
346. A Moissette, Y Batonneau, C Brémard. J Am Chem Soc 123:12325–12334, 2001.
347. C Brémard, G Buntinx, V De Waele, C Didierjean, I Gener, O Poizat. J Mol Struct 481:69–81, 1999.
348. I Gener, G Buntinx, C Brémard. Angew Chem Int Ed 38:1819–1822, 1999.
349. G Buntinx, G Ginestet, I Gener, G Coustillier, C Brémard. Laser Chem 19:325–327, 1999.
350. I Gener, G Ginestet, G Buntinx, C Brémard. Phys Chem Chem Phys 2:1855–1864, 2000.
351. I Gener, G Buntinx, C Brémard. Microporous Mesoporous Mat 41:253–268, 2000.
352. I Gener, G Ginestet, G Buntinx, C Brémard. J Phys Chem B 104:11656–11666, 2000.
353. A Moissette, C Brémard. Micropor Mesopor Mat 47:345–357, 2001.
354. LA Lyon, CD Keating, AP Fox, BE Baker, L He, SR Nicewarner, SP Mulvaney, MJ Natan. Anal Chem 70:341R–361R, 1998.
355. G Xiong, C Li, Z Feng, J Li, P Ying, H Li, Q Xin. Stud Surf Sci Catal 130:341–346, 2000.
356. G Xiong, C Li, Z Feng, P Ying, Q Xin, J Liu. J Catal 186:234–237, 1999.
357. G Xiong, Z Feng, J Li, Q Yang, P Ying, Q Xin, C Li. J Phys Chem B 104:3581–3588, 2000.
358. SA Asher. Anal Chem 65:A59–A66, 1993; 65:A201–A210, 1993.
359. PK Dutta, RE Zaykoski. Zeolites 8:179–182, 1988.
360. AJM De Man, BWH Van Beest, M Leslie, RA Van Santen. J Phys Chem 94:2524–2534, 1990.
361. P Mcmillan. Am Miner 69:622, 1984.
362. WP Griffith. J Chem Soc A 1372–1377, 1969.
363. A Miecznikowski, J Hanuza. Zeolites 5:188–193, 1985.
364. DW Breck. Zeolite Molcular Sieves. New York: John Wiley & Sons 1974, pp 45–50.
365. M Bartsch, P Bornhauser, G Calzaferri, R Imhof. Stud Surf Sci Catal 84:2089–2098, 1994.
366. MMJ Treacy, JM Newsam. Nature 332:249–251, 1988.
367. A Miecznikowski, J Hanuza. Zeolites 7:249–254, 1987.
368. M Taramasso, G Perego, B Notari. US Patent 4,410,501 (1983).
369. W Holderich, M Messe, M Nauman. Angew Chem Int Ed 27:226–246, 1988.
370. A Esposito, M Taramasso, C Neri, F Buonono. UK Patent 102,665 (1985).
371. CB Khouw, CB Dartt, JA Labinger, ME Davis. J Catal 149:195–205, 1994; CB Khouw, ME Davis. J Catal 151:77–86, 1995.
372. A Tuel, S Moussa-Khouzami, Y Ben Taarit, C Naccache. J Mol Catal 68:45–52, 1991; A Tuel, Y Ben Taarik. Appl Catal 102:69–77, 1993, A Tuel, Y Ben, C Naccache. Zeolites 13:454–461, 1993; A Tuel. Zeolites 16:108–117, 1996.
373. JA Martens, Ph Buskens, PA Jacobs. Appl Catal A General 99:71–84, 1993; DRC Huybreshts, I Vaesen, HX Li, PA Jacobs. Catal Lett 8:237–244, 1991.
374. G Bellussi, MS Rigutto. Stud Surf Sci Catal 85:177–213, 1994.
375. E Astorino, JB Peri, RJ Willey, G Busca. J Catal 157:482–500, 1995; CU Ingemar Odenbrano, S Lars, T Andersson, AH Lars, JGM Brandin, G Busca. J Catal 125:541–553, 1990; G Busca, G Ramis, JM Gallarado Amores, VS Escribano, P Piaggio. J Chem Soc Faraday Trans 90:3181–3190, 1994.
376. E Duprey, P Beaunier, MA Springuel-Huet, F Bozon-Verduraz, J Fraissard, JM Manoli, JM Bregeault. J Catal 165:22–32, 1997.
377. D Scarano, A Zecchina, S Bordiga, F Geobaldo, G Spoto. J Chem Soc Faraday Trans 89: 4123–4130, 1993; A Zecchina, G Spoto, S Bordiga, A Ferrero, G Petrini, G Leofanti, M Padovan. Zeolite Chemistry and Catalysis. Amsterdam: Elsevier, 1991, pp 251, 671.

378. S Krijnen, P Sanchez, BTF Jakobs, JHC van Hooff. Micropor Mesopor Mater 31:163–173, 1999.
379. A Carati, C Flego, E Previde Massara, R Millini, L Carluccio, WO Parker Jr, G Bellussi. Micropor Mesopor Mater 30:137–144, 1999.
380. L Tosheva, B Mihailova, V Valtchev, J Sterte. Micropor Mesopor Mater 39:91–101, 2000.
381. V Bolis, S Bordiga, C Lamberti, A Zecchina, A Carati, F Rivetti, G Spano, G Petrini. Micropor Mesopor Mater 30:67–76, 1999.
382. V Bolis, S Bordiga, C Lamberti, A Zecchina, A Carati, F Rivetti, G Spano, G Petrini. Langmuir 15:5753–5764, 1999.
383. JL Grieneisen, H Kessler, E Fache, AM Le Govic. Micropor Mesopor Mater 37:379–386, 2000.
384. J Klaas, K Kulawik, G Schulz-Ekloff, NI Jaeger. Stud Surf Sci Catal 84:2261–2268, 1994.
385. A Tuel, Y Ben Taarit. J Chem Soc Chem Commun 1578–1580, 1992; Zeolites 14:169–176, 1994; 14:272–281, 1994; A Tuel, J Diab, P Gelin, M Dufaux, JF Dutel, Y Ben Taarit. J Mol Catal 63:95–102, 1990.
386. A Thangaraj, S Sivasanker. J Chem Soc Chem Commun 123–124, 1992.
387. AJHP van der Pol, AJ Verduyn, JHC van Hooff. Appl Catal 92:113–130, 1992.
388. P Behrens, J Felsche, S Vetter, G Schulz-Ekloff, NI Jaeger, W Niemann. J Chem Soc Chem Commun 678–680, 1991.
389. L Le Noc, D Trong On, S Solomykina, B Echchahed, F Beland, C Cartier dit Moulin, L Bonneviot. Stud Surf Sci Catal 101:611–620, 1996.
390. C Lamberti, S Bordiga, A Zecchina, A Carati, AN Fitch, G Artioli, G Petrini, M Salvalaggio, GL Marra. J Catal 183:222–231, 1999.
391. C Zicovich-Wilson, R Dovesi. J Mol Catal A Chem 119:449–458, 1997.
392. RM Boccuti, KM Rao, A Zecchina. Stud Surf Sci Catal 48:133–144, 1989.
393. B Notari. Stud Surf Sci Catal 37:413–426, 1987.
394. G Ricchiardi, A Damin, S Bordiga, C Lamberti, G Spano, F Rivetti, A Zecchina. J Am Chem Soc 123:11409–11419, 2001.
395. J Kornatowski, B Wichterlová, J Jirkovský, E Löffler, W Pilz. J Chem Soc Faraday Trans 92: 1067–1078, 1996.
396. B Echchahed, A Moen, D Nicholson, L Bonneviot. Chem Mater 9:1716–1719, 1997.
397. T Abe, Y Tachibana, T Uematsu, MJ Thomas, RB Bell, GN Greaves. Top Catal 3:121–134, 1996.
398. ZH Luan, J Hu, HY He, J Klinowsli, L Kevan. J Phys Chem 100:19595–19602, 1996.
399. KJ Chao, CN Wu, H Chang, LJ Lee, SF Hu. J Phys Chem 101:6341–6349, 1997.
400. T Sen, V Ramaswamy, S Ganapathy, PR Rajamohanan, S Sivasanker. J Phys Chem 100: 3809–3817, 1996.
401. GT Centi, S Perathoner, F Trifir, A Aboukais, CF Aissi, M Guelton. J Phys Chem 96:2617–2629, 1992.
402. MA Vuurman, IE Wachs. J Phys Chem 96:5008–5016, 1992.
403. H Selig, HH Claassen. J Chem Phys 44:1404, 1966.
404. ZH Luan, PA Meloni, RS Czernuszewicz, L Kevan. J Phys Chem 101:9046–9051, 1997.
405. RD Place, PK Dutta. Anal Chem 63:348–351, 1991.
406. MR Jakupca, PK Dutta. Anal Chem 64:953–957, 1992.